Delivering anion transporters to lipid bilayers in water

Daniel A. McNaughton,[a] Tsz Ying (Teresa) To,[a,b] Bryson A. Hawkins,[c] David E. Hibbs,[c] and Philip A. Gale.[a,d*]

[a.] *School of Chemistry (F11), The University of Sydney, NSW, 2006, Australia.*

[b.] *Chemistry, University of Southampton, Southampton, SO17 1BJ, UK.*

[c.] *School of Pharmacy, The University of Sydney, NSW, 2006, Australia.*

[d.] *The University of Sydney Nano Institute (SydneyNano), The University of Sydney, NSW, 2006, Australia.*

* E-mail: philip.gale@sydney.edu.au

## Contents

1. General Remarks

All chemicals and solvents were purchased from commercials suppliers and used without further purification, unless stated otherwise. Deuterated solvents for NMR were purchased from Cambridge Isotope Laboratories. 1-Palmitoyl-2-oleoyl-*sn-glycero*-3-phosphocholine (POPC) was purchased from Avanti Lipids or Corden Pharma. Anhydrous solvents were collected from an Inert Corp PureSolv MD7 solvent purification system. Deionised water was collected from a Merck Millipore Milli-Q™ reference ultrapure water purification system.

NMR spectra (^{1}H NMR and ^{13}C NMR and 2D NOESY NMR) were collected on a Bruker AVIII 500 or a Bruker Avance DPX 400. NMR titrations were performed on the same instruments. Chemical shifts (δ) were reported in ppm and calibrated using the residual solvent peak of either DMSO-*d₆*, acetonitrile-*d₃*, or chloroform-*d*. Spin multiplicities were abbreviated to s = singlet, d = doublet, t = triplet, q = quartet, m = multiplet and br = broad.

Melting points were recorded manually using a Standford Research Systems Optimelt machine, and data were reported as a range (°C). Low resolution mass spectrometry (LR-MS) was performed with a Bruker amazon SL mass spectrometer using electrospray ionisation or APCI. High resolution mass spectra (HR-MS) were recorded on a Bruker Apex II Fourier Transform Ion Cyclotron Resonance (FTICR) mass spectrometer with a 7.0 T magnet, fitted with an off-axis analytic electrospray source with quadrupole mass analyser, and are reported as m/z (relative intensity).

Infrared absorption spectra were recorded on a Bruker Alpha-E FT-IR spectrometer using attenuated total reflection (ATR) for the compounds and complexes as solids. Notable vibrational wavenumbers are labelled. UV-Vis spectra were recorded on a Cary 4000 UV-Vis spectrophotometer at 298 K using a 1 cm quartz cuvette, equipped with stirring multicell holder. The ISE assay experiments were conducted on the Fisherbrand™ Accumet™ Chloride Combination Electrode.

2. Synthetic Overview of Compounds 1–6.
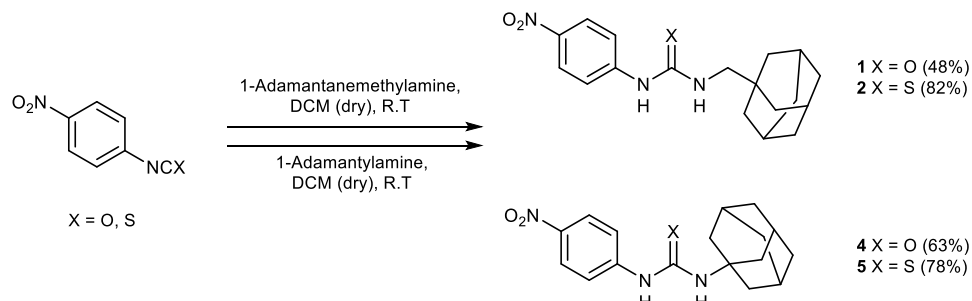
Scheme S1. The general synthesis of urea and thiourea compounds **1**, **2**, **4**, and **5** via condensation reaction between the relevant 4-nitrophenyl iso(thio)cyanate and adamantane-appended amine derivative.
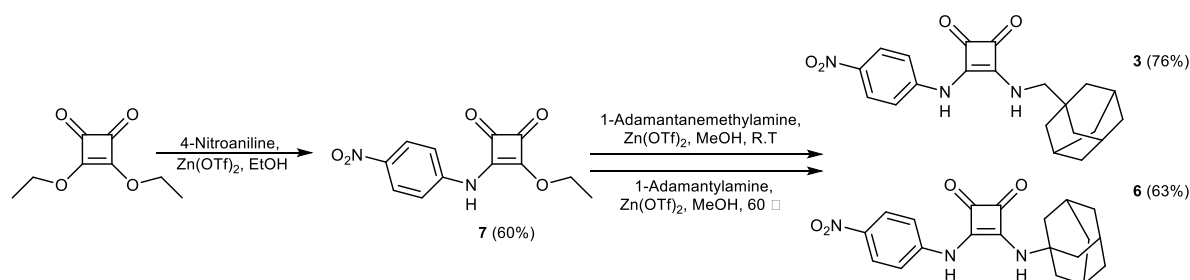
Scheme S2. The general synthesis of intermediate **7** and the final adamantyl-appended squaramide compounds **3** and **6**.

2. Synthesis

1-(1-adamantylmethyl)-3-(4-nitrophenyl)urea (1)
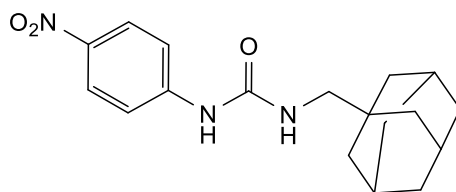
4-nitrophenyl isocyanate (547 mg, 3.34 mmol) was dissolved in dry DCM (15 mL) before 1-adamantyl methylamine (0.53 mL, 3.04 mmol) was added dropwise to the solution. This was left to stir at R.T for 12 h. A precipitate formed, which was identified as the symmetrical bis-4-nitrophenylurea side-product. This was filtered off, and the solvent was removed from the

filtrate *in vacuo*. The oily residue was subjected to column chromatography (30:70 ethyl acetate:hexane eluent) to yield a light yellow fluffy solid (480 mg, 1.46 mmol, 48%).
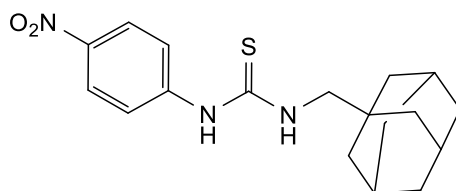
MP = 219–222 °C

¹H NMR (500 MHz, DMSO-*d_6*) δ ppm 9.15 (2 H, s), 8.13 (2 H, m), 7.60 (2 H, m), 6.40 (1 H, t, J 6.1), 2.83 (2 H, d, J 6.1), 1.94 (3 H, s), 1.68 (3 H, d, J 11.9), 1.59 (3 H, d, J 10.8), 1.46 (6 H, d, J 2.8); **¹³C NMR** (101 MHz, DMSO-d_6) δ ppm 155.1, 147.7, 140.8, 125.6, 117.1, 51.2, 37.0, 34.0, 28.1.

LR-MS (ESI⁺) *m/z* 352.2 [M+Na]⁺, 681.38 [2M+Na]⁺; **HR-MS** (ESI⁺) calcd for $C_{18}H_{23}N_3O_3$ [M+Na]⁺: 352.17394, found *m/z* 352.16314.

## 1-(1-adamantylmethyl)-3-(4-nitrophenyl)thiourea (2)

4-Nitrophenyl isothiocyanate (109 mg, 0.61 mmol) was dissolved in dry DCM (15 mL) before 1-adamantyl methylamine (0.11 mL, 0.61 mmol) was added dropwise to the solution. This was left to stir at R.T for 12 h. Next, the solvent was removed in vacuo and the residue subjected to column chromatography (30:70 ethyl acetate:hexane as the eluent). The solvent was removed *in vacuo* from the collected fraction and the resultant orange oil was dried in vacuo to yield a yellow solid (173 mg, 0.50 mmol, 82%).

MP = 199–202 °C

¹H NMR (500 MHz, DMSO-*d_6*) δ ppm 10.15 (1 H, s), 8.17 (2 H, d, J 9.2), 8.12 (1 H, s), 7.94 (2 H, d, J 9.2), 3.29 (2 H, d, J 5.3), 1.96 (2 H, s), 1.69 (3 H, d, J 12.1), 1.62 (3 H, d, J 10.8), 1.54 (6 H, d, J 2.9); **¹³C NMR** (101 MHz, DMSO-d_6) δ ppm 181.0, 147.1, 142.1, 124.9, 120.6, 55.8, 36.9, 34.2, 28.1.

LR-MS (ESI⁻) *m/z* 344.23 [M−H]⁻, 725.47 [M+Cl]⁻; **HR-MS** (ESI⁺) calcd for $C_{18}H_{23}N_3O_2S$ [M+Na]⁺: 368.14032, found *m/z* 368.14031.

## 3-ethoxy-4((4-nitrophenyl)amino)cyclobutene-1,2-dione (7)
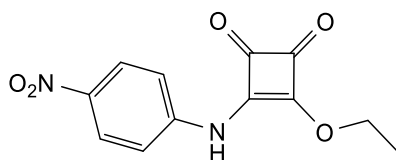
4-nitroaniline (1 g, 7.25 mmol) and zinc triflate (500 mg, 1.38 mmol) were dissolved in ethanol (50 mL) and stirred, before diethylsquarate (1 mL, 6.76 mmol) was added dropwise. The reaction flask was covered in foil and left to stir overnight. A precipitate formed which was filtered and washed with cold ethanol (2 x 25 mL) and dried *in vacuo* overnight to leave a pure orange solid (733 mg, 2.80 mmol, 41%). The ^{1}H-NMR and LR-MS spectra were found to be consistent with literature spectra.

^{1}H NMR (400 MHz, DMSO-d_6) δ ppm 11.20 (1 H, s), 8.21 (2 H, d, J 9.2), 7.59 (2 H, d, J 9.2), 4.80 (2 H, d, J 7.1), 3.17 (3 H, 7, J 7.1), ethanol solvent peaks are also visible.

LR-MS (ESI$^-$) *m/z* 260.79 [M−H]$^-$.

N-(1-adamantylmethyl)-*N'*-(4-nitrophenyl)squaramide (3)
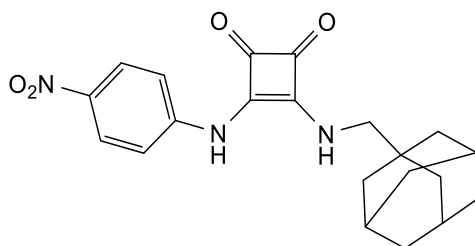
Compound **7** (400 mg, 1.52 mmol) and zinc triflate (111 mg, 0.3 mmol) were dissolved as much as possible in methanol (35 mL) and stirred. Next, 1-adamantylmethylamine (0.3 mL, 1.67 mmol) was added dropwise and the solution immediately changed colour from orange to dark red. The reaction was left overnight before a precipitate formed. This was filtered, washed with cold methanol (2 x 50 mL), and dried *in vacuo* to yield a pure dark red solid (442 mg, 1.16 mmol, 76%).
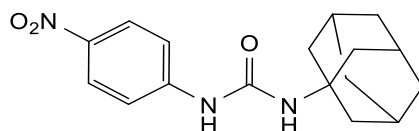
MP = +300 °C

^{1}H NMR (500 MHz, DMSO-d_6) δ ppm 9.96 (1H, br), 8.21 (2 H, d, J 8.8), 7.84 (1 H, s), 7.62 (2 H, d, J 8.8), 1.97 (3 H, s), 1.76 – 1.57 (6 H, m), 1.50 (6 H, s) [Methyl proton signal hidden beneath

water peak]; **¹³C NMR** (101 MHz, DMSO-d₆) δ ppm 185.1, 180.1, 170.7, 162.0, 145.4, 141.3, 125.6, 117.6, 55.3, 36.3, 27.5.

LR-MS (ESI⁻) *m/z* 379.95 [M−H]⁻; **HR-MS** (ESI⁺) calcd for C₂₁H₂₃N₃O₄ [M+H]⁺: 382.17613, found *m/z* 382.17583.
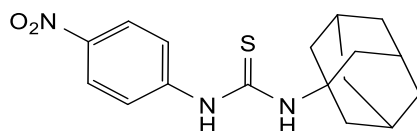
1-adamantyl-3-(4-nitrophenyl)urea (4)

4-Nitrophenylisocyanate (412 mg, 2.52 mmol) was dissolved in dry DCM (15 mL). Separately, 1-adamantylamine (190 mg, 1.26 mmol) was dissolved in dry DCM (15 mL) and added dropwise to the solution. This was left to stir at R.T overnight before a yellow precipitate was filtered off, which proved to be the mono-urea symmetrical 4-nitrophenyl side product. The solvent was removed *in vacuo* and the residue purified using silica gel column chromatography (30:70 ethyl acetate:hexane eluent). The solvent was removed *in vacuo* to yield a fluffy pale-yellow solid (252 mg, 0.80 mmol, 63%).

MP = 228−231 °C

¹H NMR (400 MHz, DMSO-*d₆*) δ ppm 9.01 (1H, s), 8.11 (2 H, d, J 9.3), 7.56 (2H, d, J 9.2), 6.15 (1H, s), 2.03 (3H, s), 1.95 (6H, s), 1.64 (6H, s); **¹³C NMR** (101 MHz, DMSO-d₆) δ ppm 153.0, 147.2, 140.2, 125.1, 116.5, 50.2, 41.4, 35.9, 28.8.

LR-MS (ESI⁺) *m/z* 313.89 [M−H]⁻; **HR-MS** (ESI⁺) calcd for C₁₇H₂₁N₃O₃ [M+Na]⁺: 338.14751, found *m/z* 338.14729.

## 1-adamantyl-3-(4-nitrophenyl)thiourea (5)

4-Nitrophenylisothiocyanate (160 mg, 1.46 mmol) was dissolved in dry DCM (15 mL). Separately, 1-adamantylamine (200 mg, 1.32 mmol) was dissolved in dry DCM (15 mL) and added dropwise to the solution. This was left to stir at R.T for 12 h. A precipitate formed was filtered and washed with DCM (3 × 30 mL) to give the pure white product. Next, the solvent was removed *in vacuo* and the residue subjected to column chromatography (10:90 ethyl acetate:hexane as the eluent). The solvent was removed *in vacuo* from the collected fraction and the solid was dried *in vacuo* to yield a white solid (312 mg, 0.94 mmol, 71%).

MP = 187–190 °C

¹H NMR (500 MHz, DMSO-d_6) δ ppm 9.89 (1 H, s), 8.15 (2 H, d, J 9.2), 7.82 (2 H, d, J 9.2), 7.78 (1 H, s), 2.25 (6 H, s), 2.07 (3 H, s), 1.65 (6 H, s) **¹³C NMR** (101 MHz, DMSO-d_6) δ ppm 178.0, 146.6, 141.5, 124.4, 120.3, 53.9, 35.9, 28.9.

LR-MS (ESI⁺) *m/z* 332.18 [M+H]⁺, 685.23 [2M+Na]⁺; **HR-MS** (ESI⁺) calcd for $C_{17}H_{21}N_3O_2S$ [M+Na]⁺: 354.12467, found *m/z* 354.12456.

N-(adamantyl)-*N'*-(4-nitrophenyl)squaramide (6)
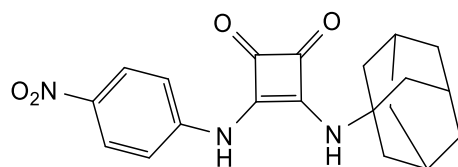
Compound **7** (400 mg, 1.52 mmol) and zinc triflate (111 mg, 0.3 mmol) were dissolved as much as possible in methanol (35 mL) and stirred. 1-adamantylamine (252 mg, 1.67 mmol) was added to the solution. Triethylamine (1 mL) was added to the reaction, which was left to stir overnight. A small amount of red precipitate formed which was identified as product. The solvent was removed from the reaction mixture *in vacuo* before the residue was subjected to column chromatography (2:98 methanol:dichloromethane eluent with 3% TEA). The fractions containing pure compound were dried to leave an orange-red solid (346 mg, 0.94 mmol, 63%).

MP = +300 °C

¹H NMR (500 MHz, DMSO-*d₆*) δ ppm 10.22 (1 H, br), 8.22 (2 H, d, J 9.1), 8.10 (1 H, s), 7.66 (2 H, d, J 9.1), 2.11 (3 H, s), 1.99 (6 H, s), 1.66 (6 H, s); **¹³C NMR** (101 MHz, DMSO-d₆) δ ppm 183.4, 179.6, 170.2, 163.2, 145.2, 141.5, 125.6, 117.7, 53.1, 42.4, 35.2, 28.9.

LR-MS (ESI⁻) *m/z* 365.91 [M−H]⁻; **HR-MS** (ESI⁺) calcd for $C_{20}H_{21}N_3O_4$ [M+H]⁺: 368.16048, found *m/z* 368.16020.

4. Characterisation Data

Proton NMR and low-resolution mass spectrometry (LR-MS) are shown for each compound. Carbon NMR and high-resolution mass spectrometry (HR-MS) are shown for novel compounds.

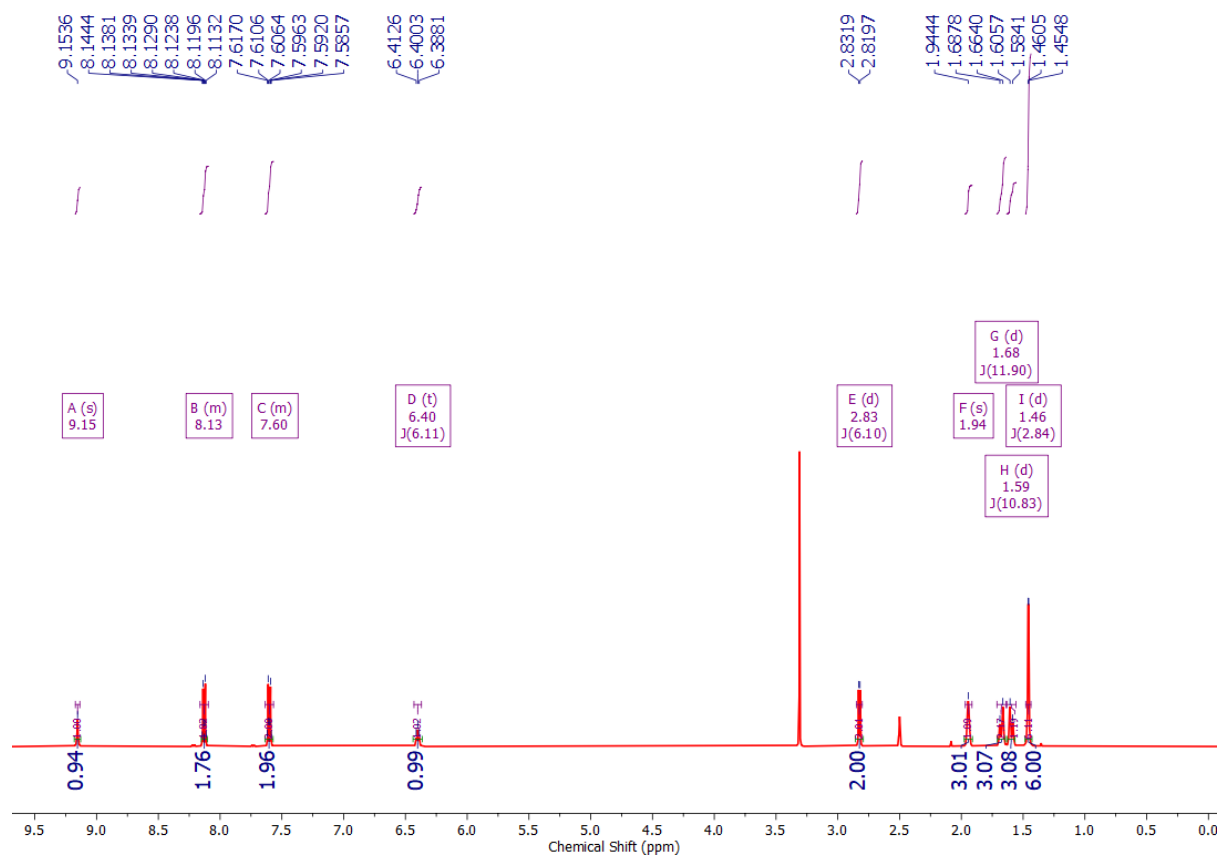## 1-(1-adamantylmethyl)-3-(4-nitrophenyl)urea (1)
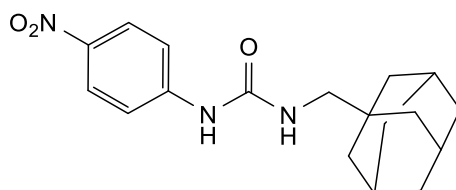
Figure S1. ¹H NMR (500 MHz) spectrum of 1-(1-adamantylmethyl)-3-(4-nitrophenyl)urea in DMSO-d_6 at 298 K.

Figure S2. ^{13}C NMR (101 MHz) spectrum of 1-(1-adamantylmethyl)-3-(4-nitrophenyl)urea in DMSO-d_6 at 298 K.

Figure S3. LR-MS (ESI$^+$) spectrum of 1-(1-adamantylmethyl)-3-(4-nitrophenyl)urea.

Figure S4. HR-MS (ESI+) spectrum of 1-(1-adamantylmethyl)-3-(4-nitrophenyl)urea.

1-(1-adamantylmethyl)-3-(4-nitrophenyl)thiourea – (2)
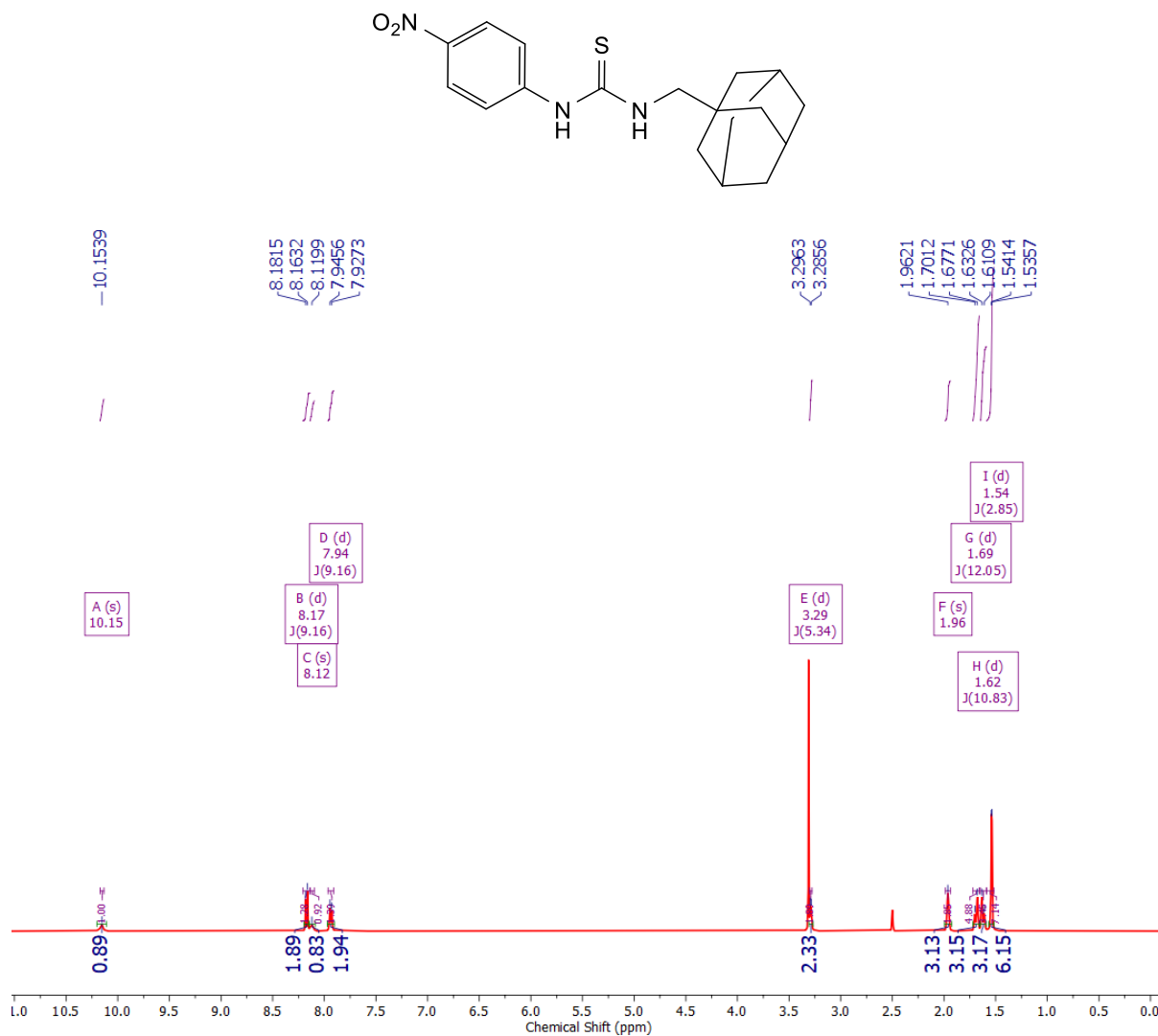
Figure S5. ^{1}H NMR (500 MHz) spectrum of 1-(1-adamantylmethyl)-3-(4-nitrophenyl)thiourea in DMSO-d_6 at 298 K.
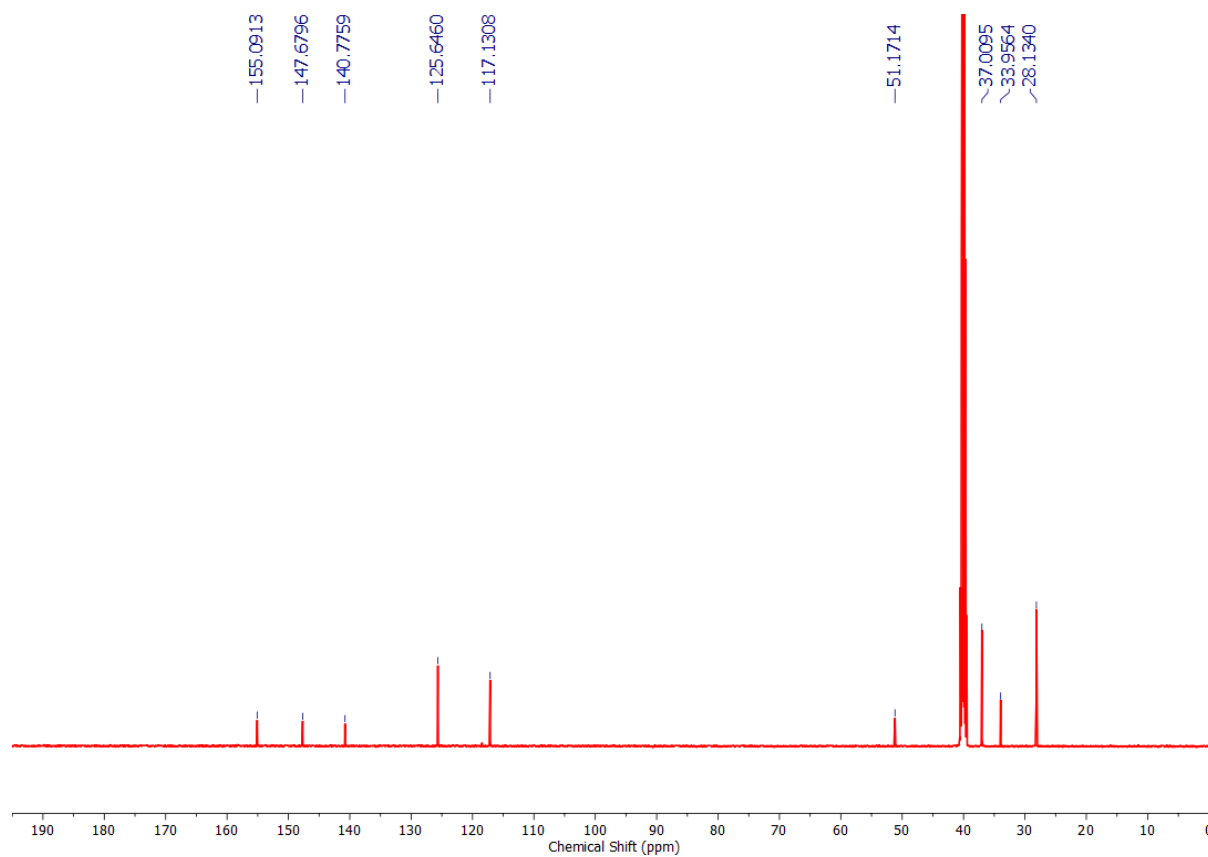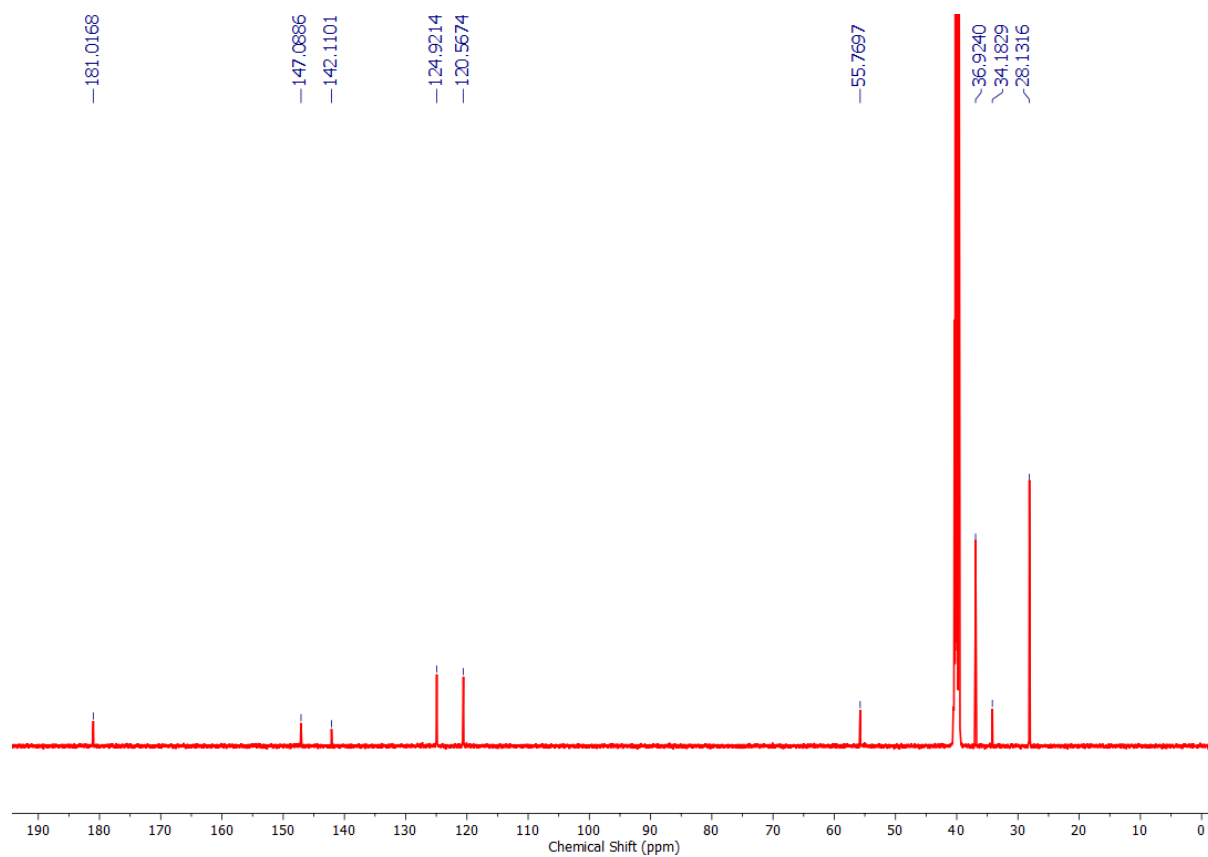
Figure S6. ^{13}C NMR (101 MHz) spectrum of 1-(1-adamantylmethyl)-3-(4-nitrophenyl)thiourea in DMSO-d_6 at 298 K.
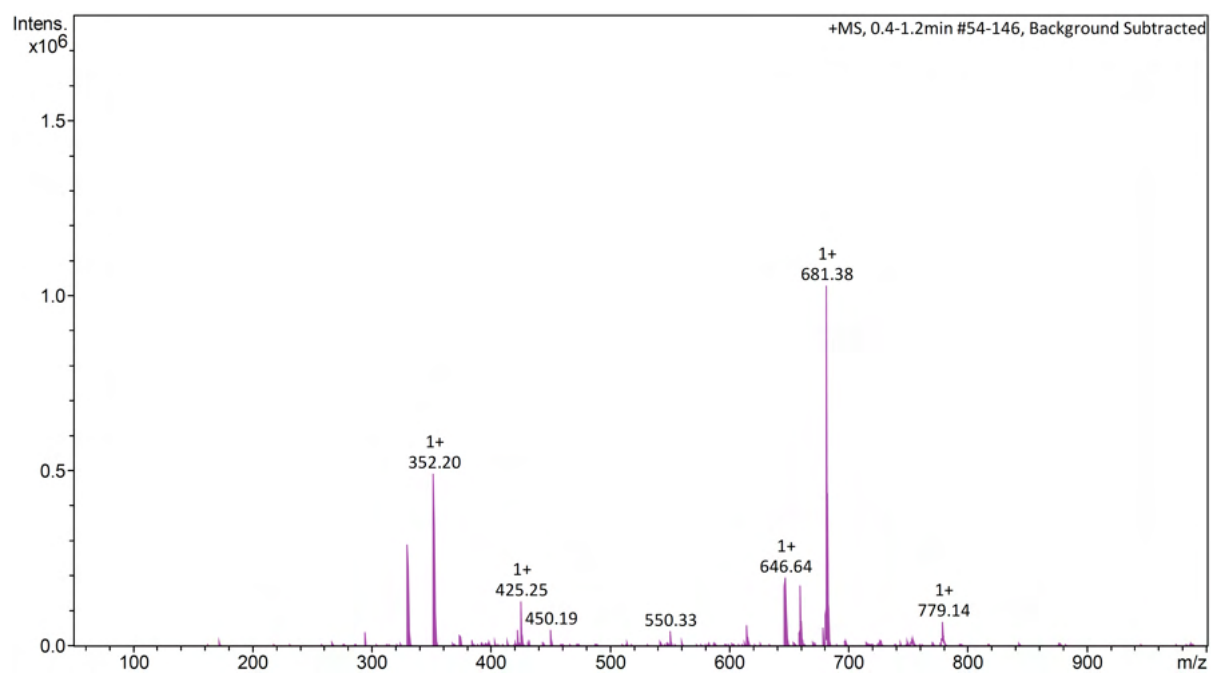

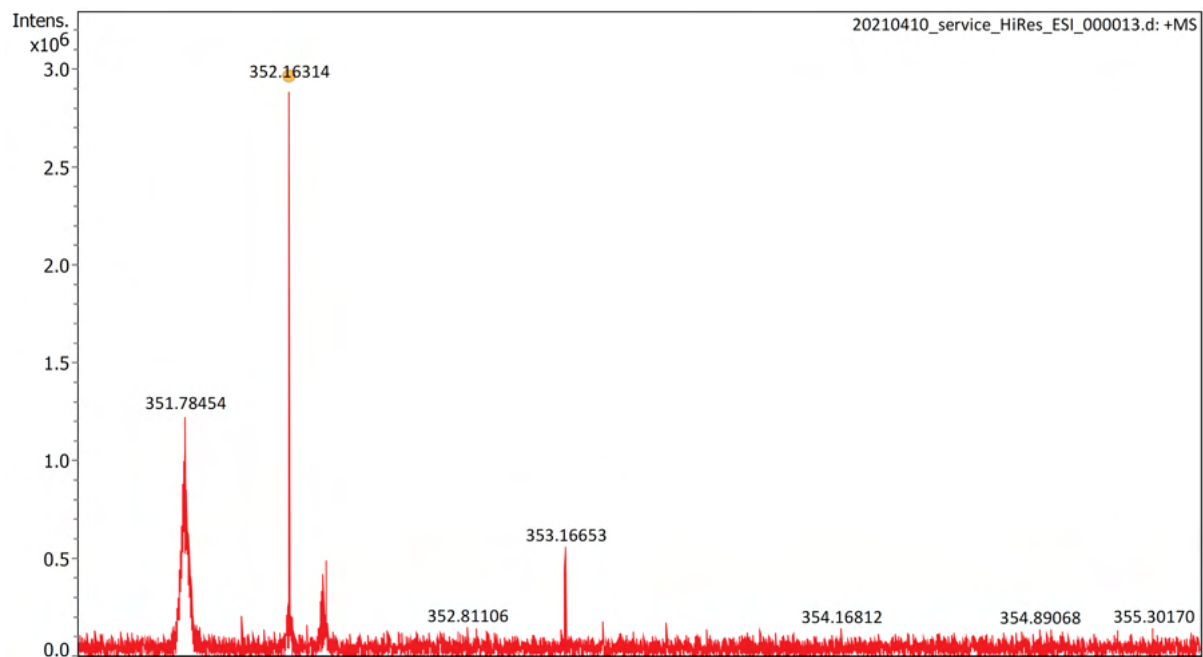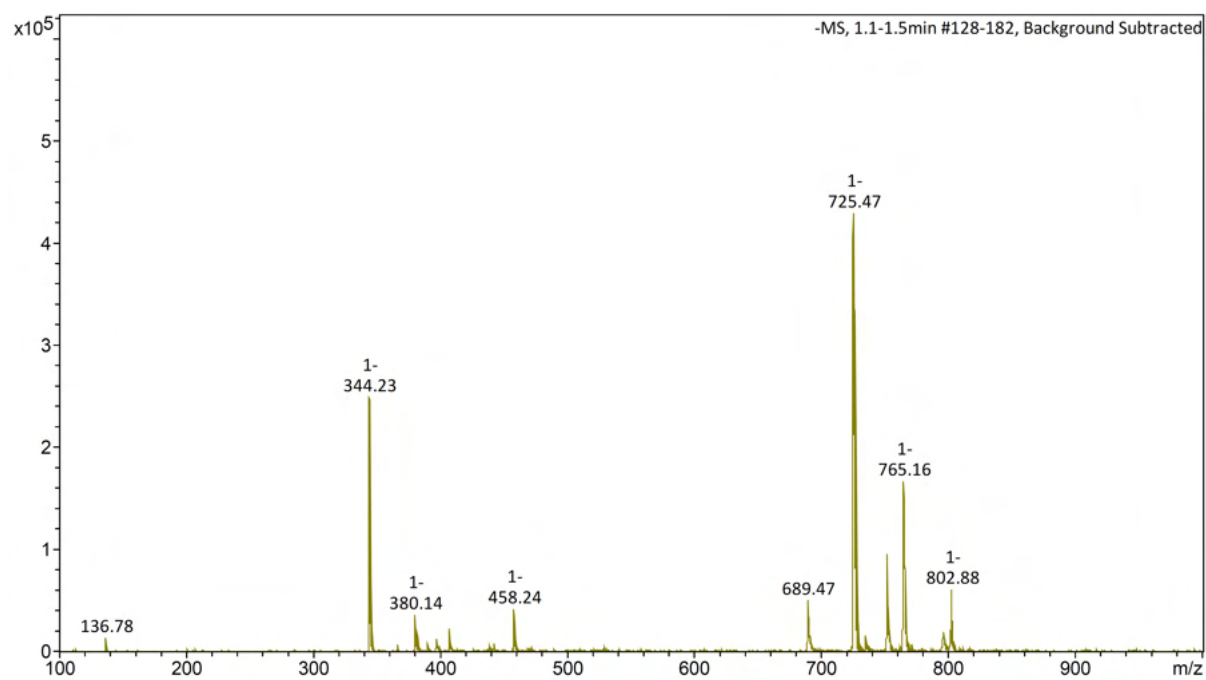**Figure S7**. LR-MS (ESI⁻) spectrum of 1-(1-adamantylmethyl)-3-(4-nitrophenyl)thiourea.

14

Figure S8. HR-MS (ESI+) spectrum of 1-(1-adamantylmethyl)-3-(4-nitrophenyl)thiourea.

3-ethoxy-4((4-nitrophenyl)amino)cyclobutene-1,2-dione (7)
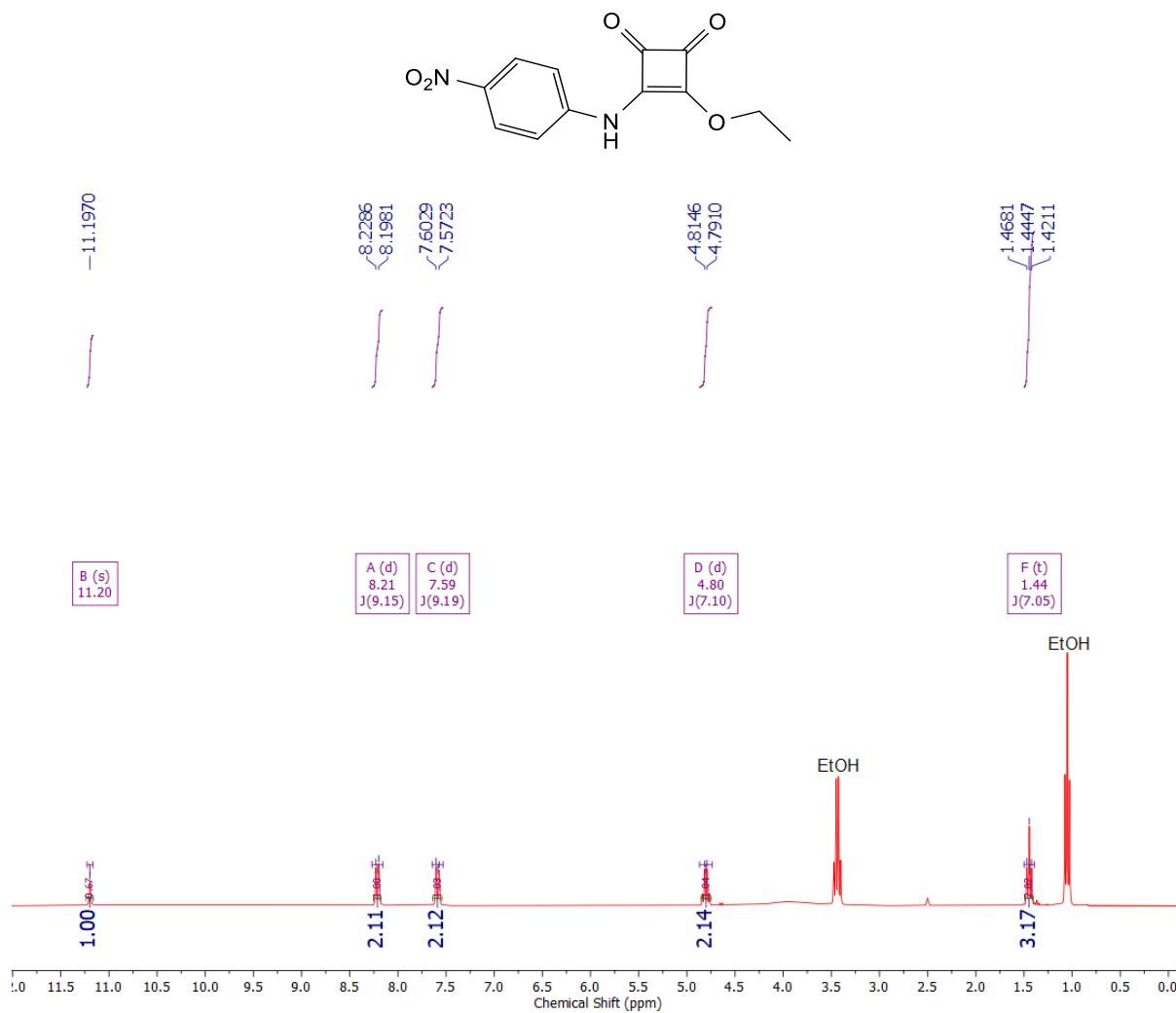
Figure S9. ^{1}H NMR (400 MHz) spectrum of 3-ethoxy-4((4-nitrophenyl)amino)cyclobutene-1,2-dione in DMSO-d_6 at 298 K.
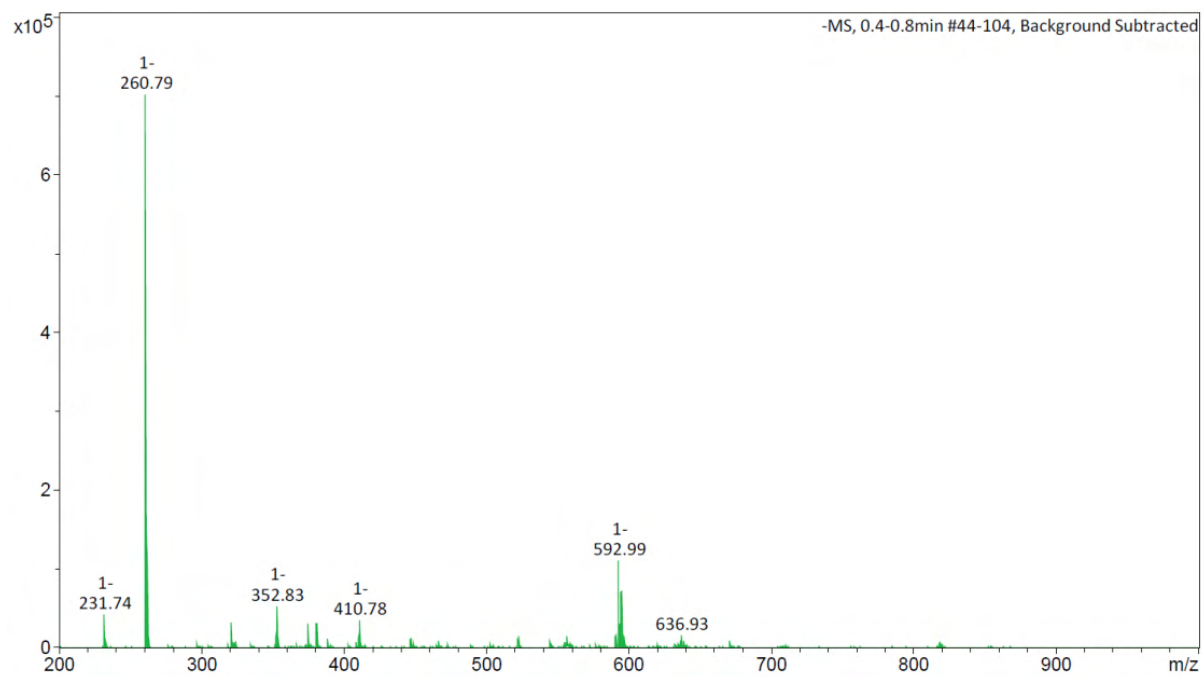
Figure S10. LR-MS (ESI⁻) spectrum of 3-ethoxy-4((4-nitrophenyl)amino)cyclobutene-1,2-dione.

N-(1-adamantylmethyl)-*N′*-(4-nitrophenyl)squaramide (3)

Figure S11. ¹H NMR (500 MHz) spectrum of *N*-(1-adamantylmethyl)-*N′*-(4-nitrophenyl)squaramide in DMSO-*d₆* at 298 K.

Figure S12. ^{1}H NMR (500 MHz) spectrum of *N*-(1-adamantylmethyl)-*N'*-(4-nitrophenyl)squaramide in DMSO-*d₆* at 298 K. Zoomed in to display broad resonance attributed to the squaramide N−H proton.

Figure S13. ^{13}C NMR (101 MHz) spectrum of *N*-(adamantyl)-*N'*-(4-nitrophenyl)squaramide urea in DMSO-d_6 at 298 K.

Figure S14. LR-MS (ESI⁻) spectrum of *N*-(1-adamantylmethyl)-*N'*-(4-nitrophenyl)squaramide.

Figure S15. HR-MS (ESI⁺) spectrum of *N*-(adamantylmethyl)-*N′*-(4-nitrophenyl)squaramide.

1-(1-adamantyl)-3-(4-nitrophenyl)urea (4)
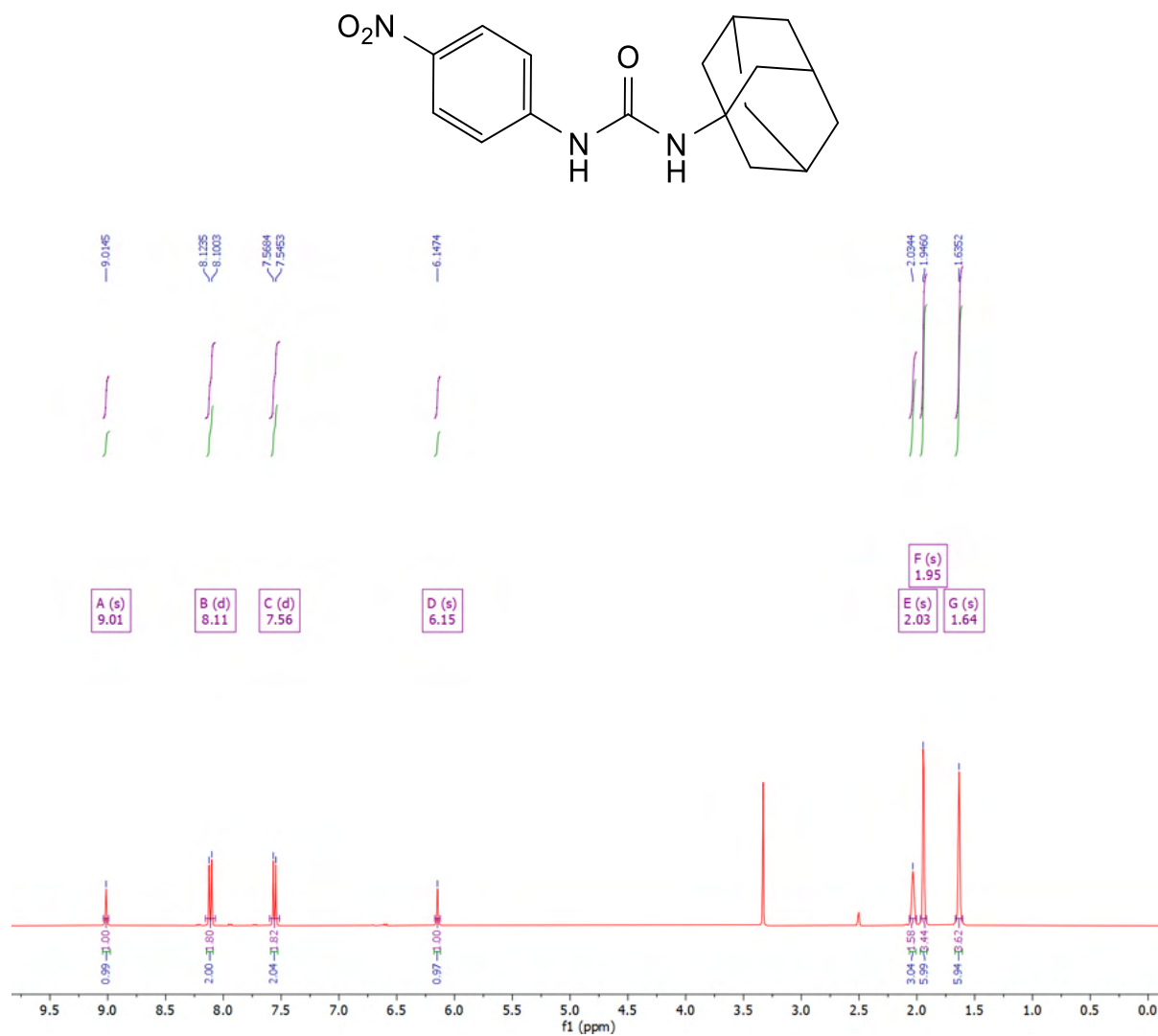
Figure S16. ¹H NMR (500 MHz) spectrum of 1-adamantyl-3-(4-nitrophenyl)urea in DMSO-d_6 at 298 K.
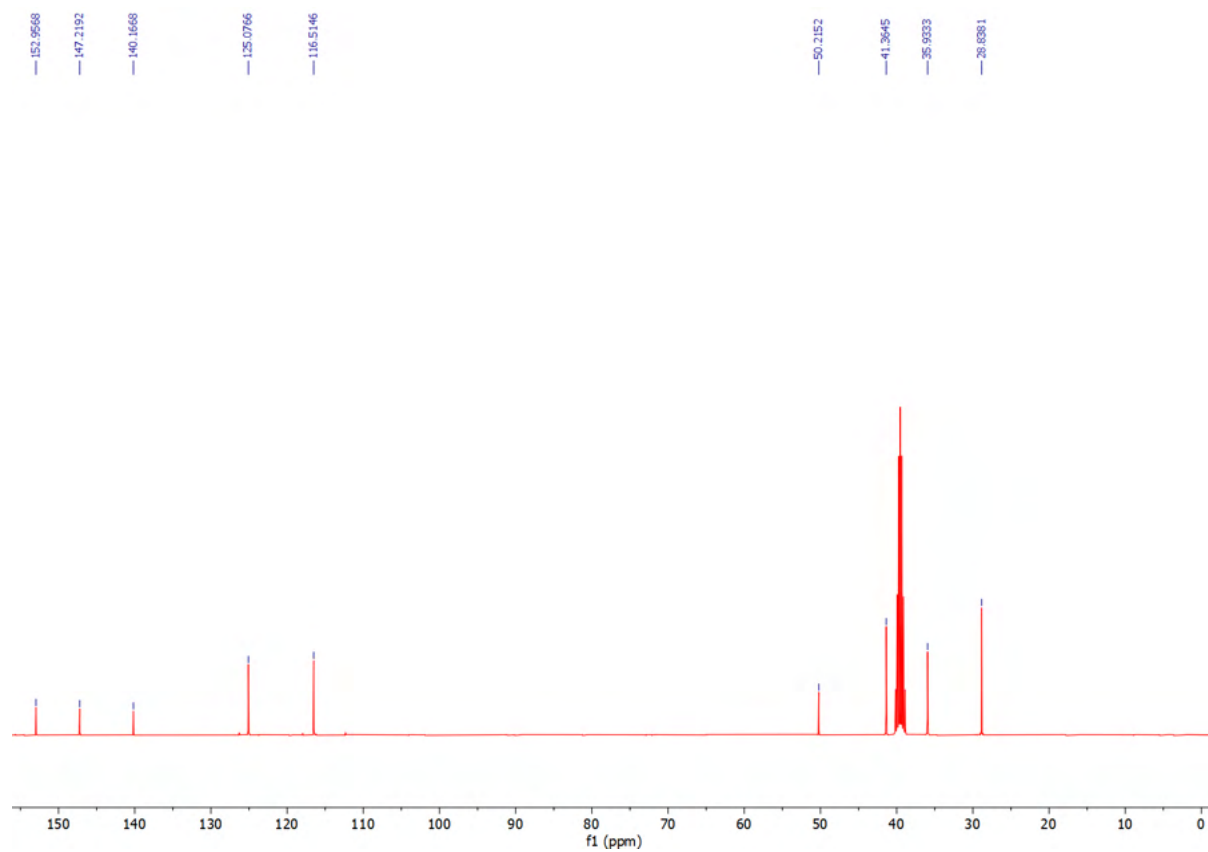
Figure S17. ¹³C NMR (101 MHz) spectrum of 1-adamantyl-3-(4-nitrophenyl)urea in DMSO-d_6 at 298 K.
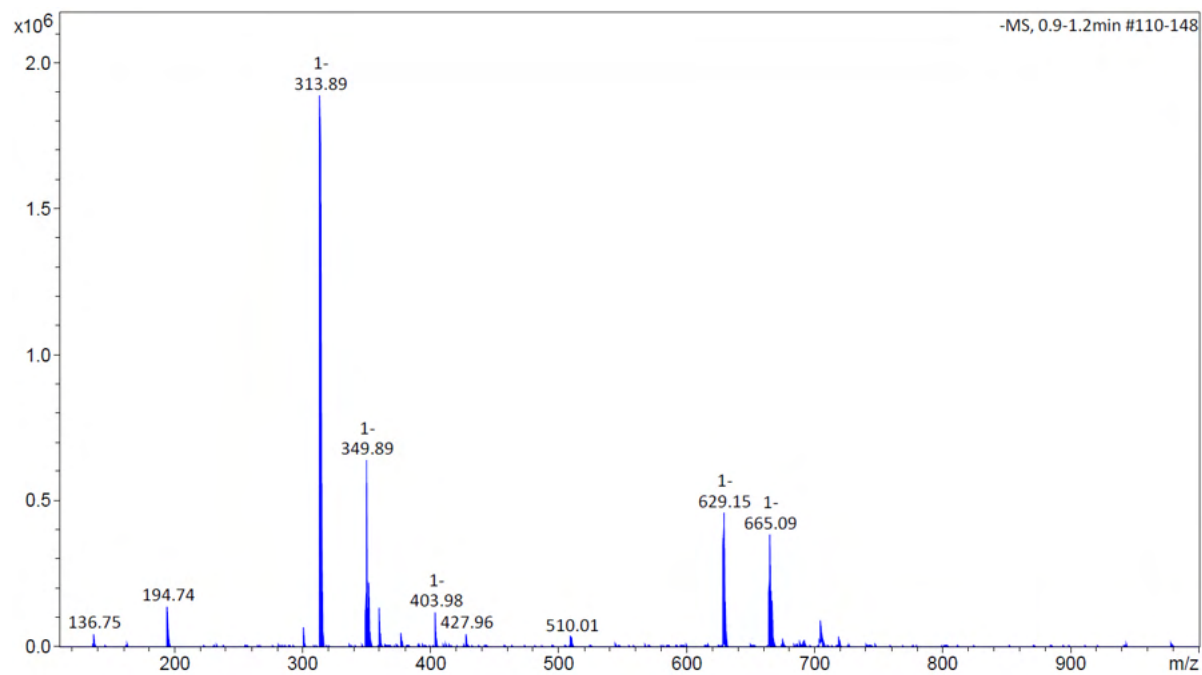
Figure S18. LR-MS (ESI⁻) spectrum of 1-adamantyl-3-(4-nitrophenyl)urea.
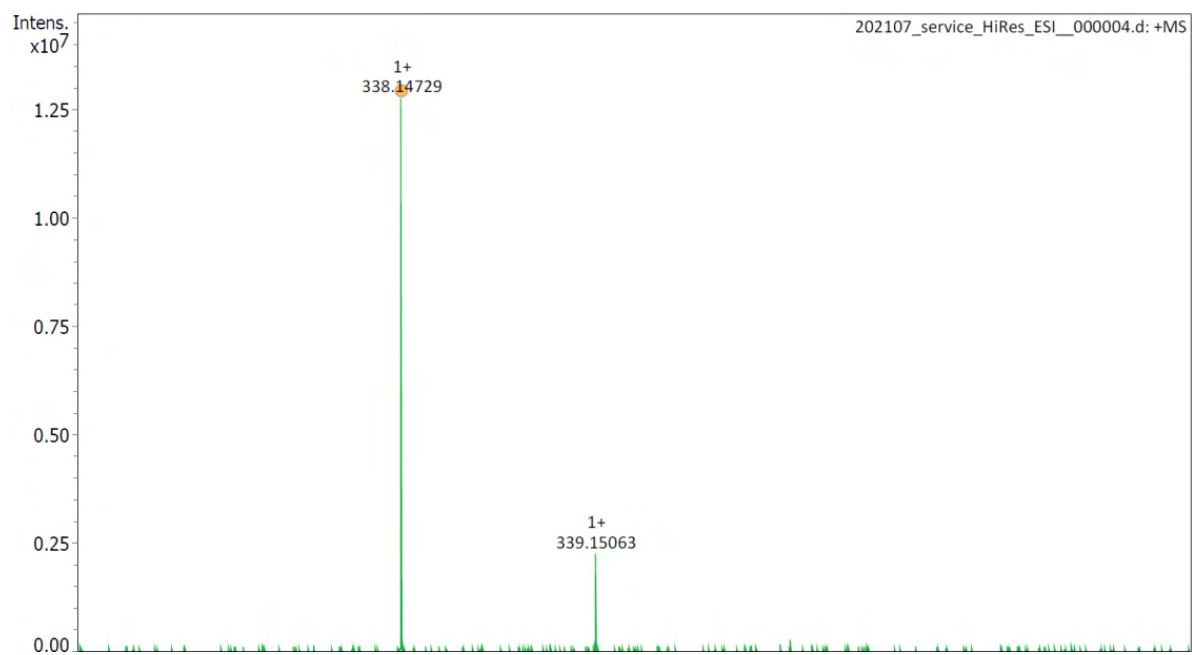
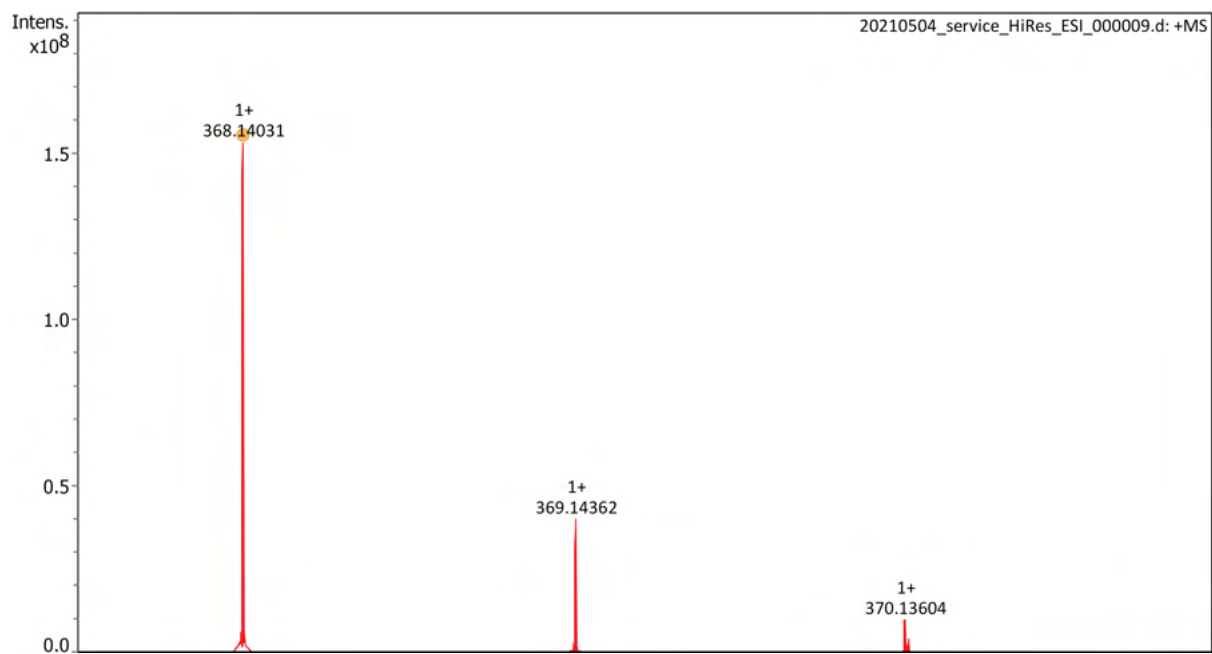**Figure S19**. HR-MS (ESI+) spectrum of 1-adamantyl-3-(4-nitrophenyl)urea.

1-adamantyl-3-(4-nitrophenyl)thiourea (5)
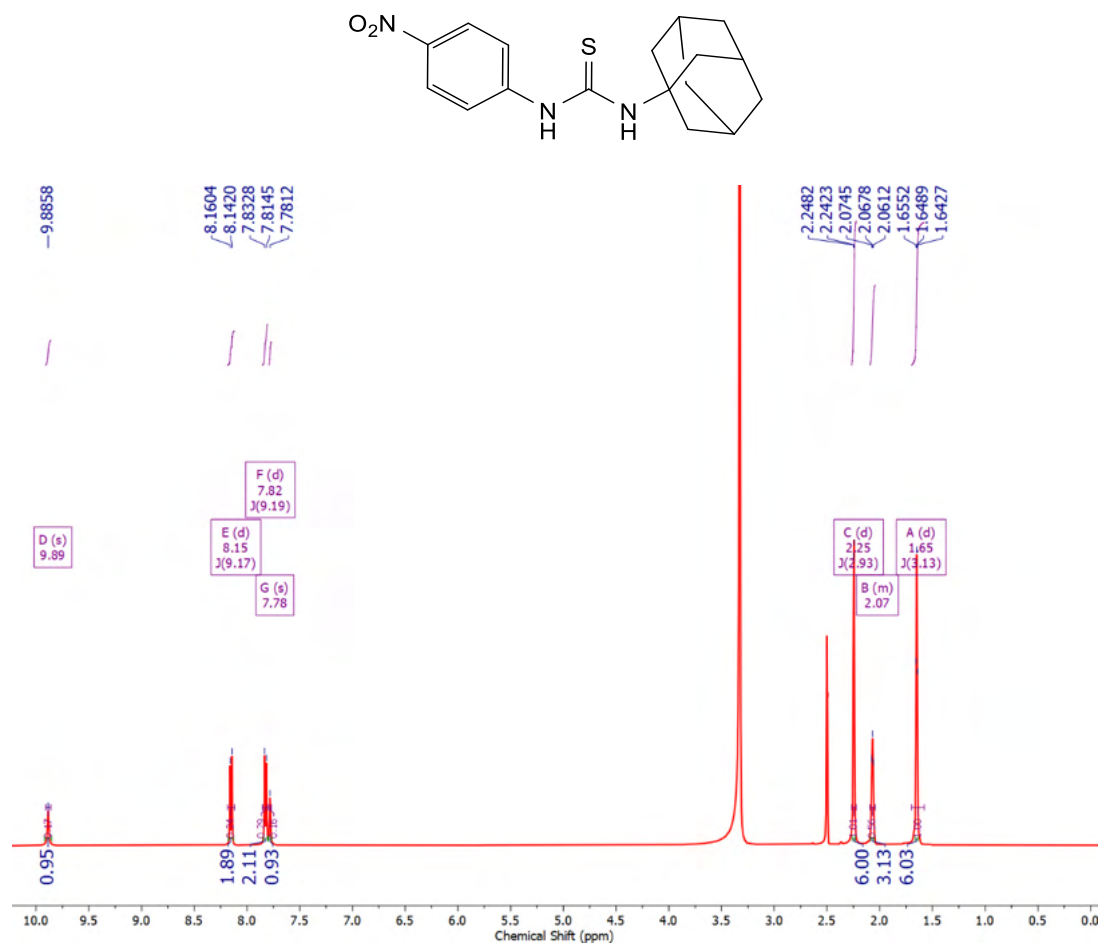
Figure S20. ^{1}H NMR (500 MHz) spectrum of 1-adamantyl-3-(4-nitrophenyl)thiourea in DMSO-d_6 at 298 K.
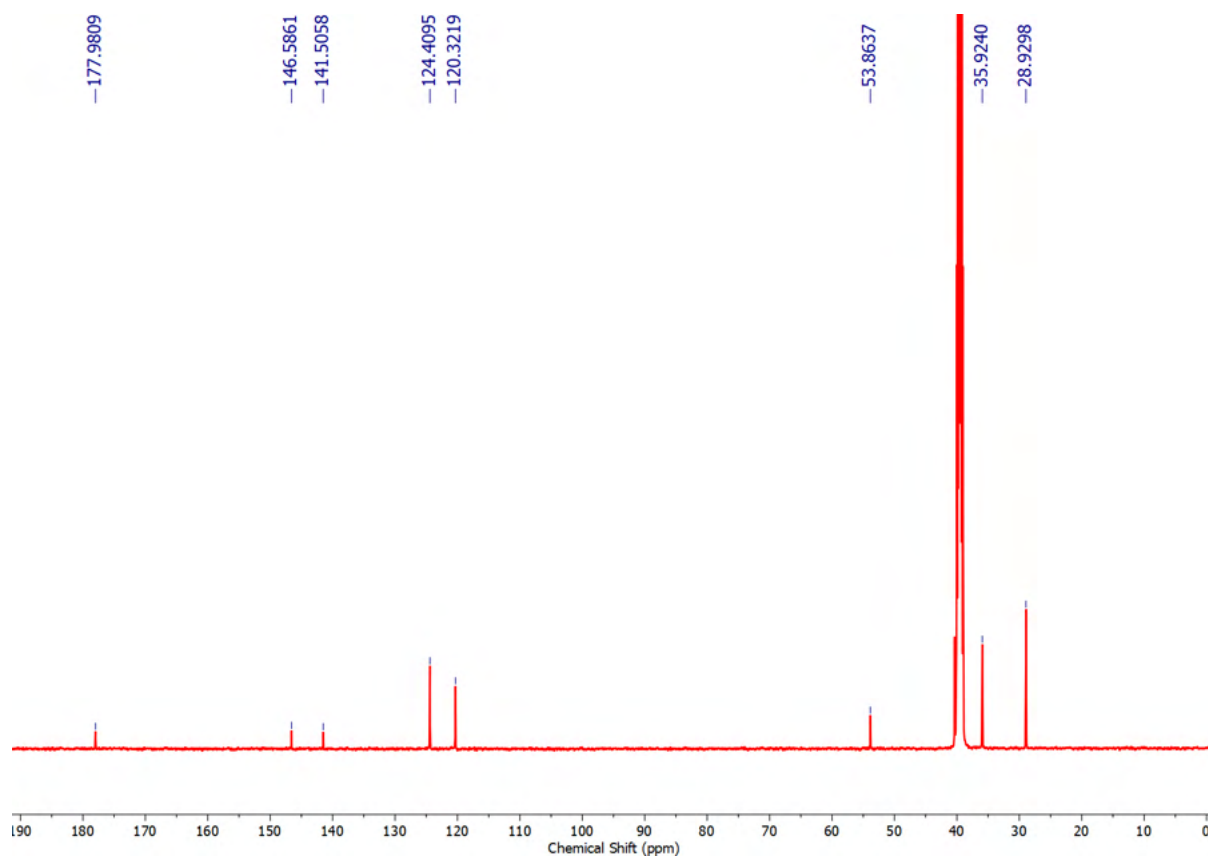
Figure S21. ^{13}C NMR (101 MHz) spectrum of 1-adamantyl-3-(4-nitrophenyl)thiourea in DMSO-d_6 at 298 K.
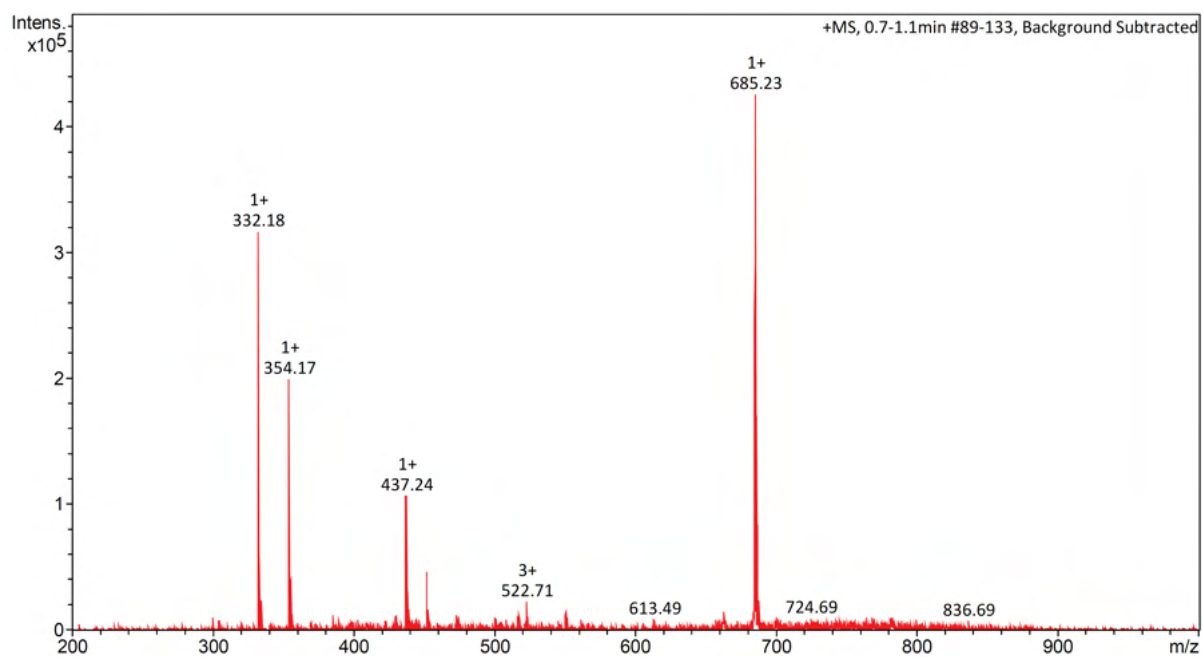
Figure S22. LR-MS (ESI$^+$) spectrum of 1-adamantyl-3-(4-nitrophenyl)thiourea.

20210308_Service_HiRes_ESI_000006.d: +MS
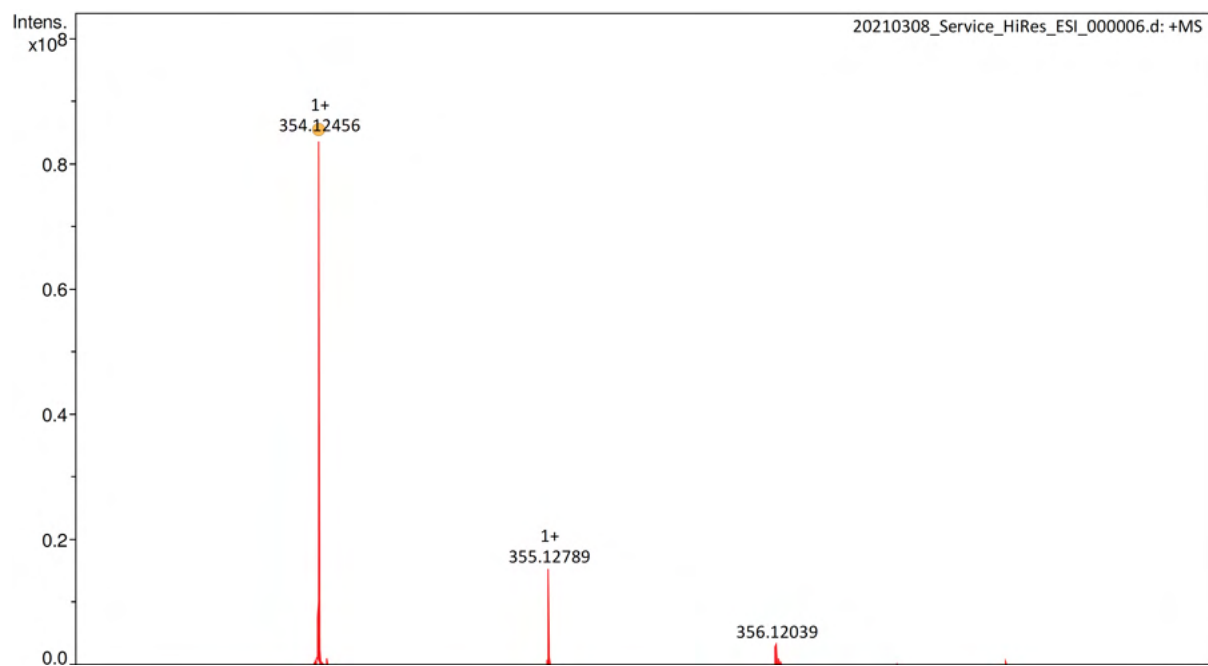
Figure S23. HR-MS (ESI⁺) spectrum of 1-adamantyl-3-(4-nitrophenyl)thiourea.
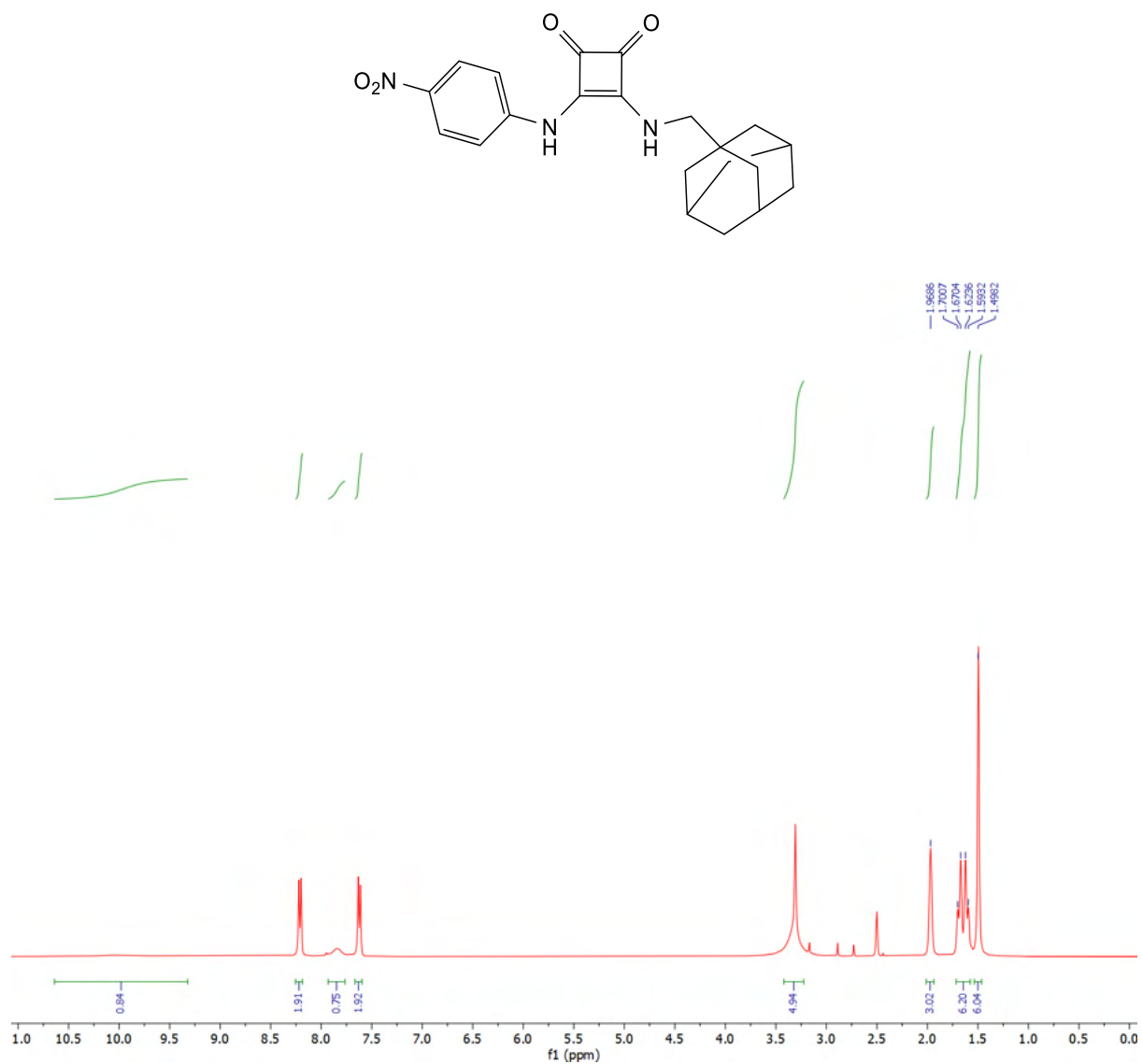
N-(adamantyl)-N′-(4-nitrophenyl)squaramide (6)
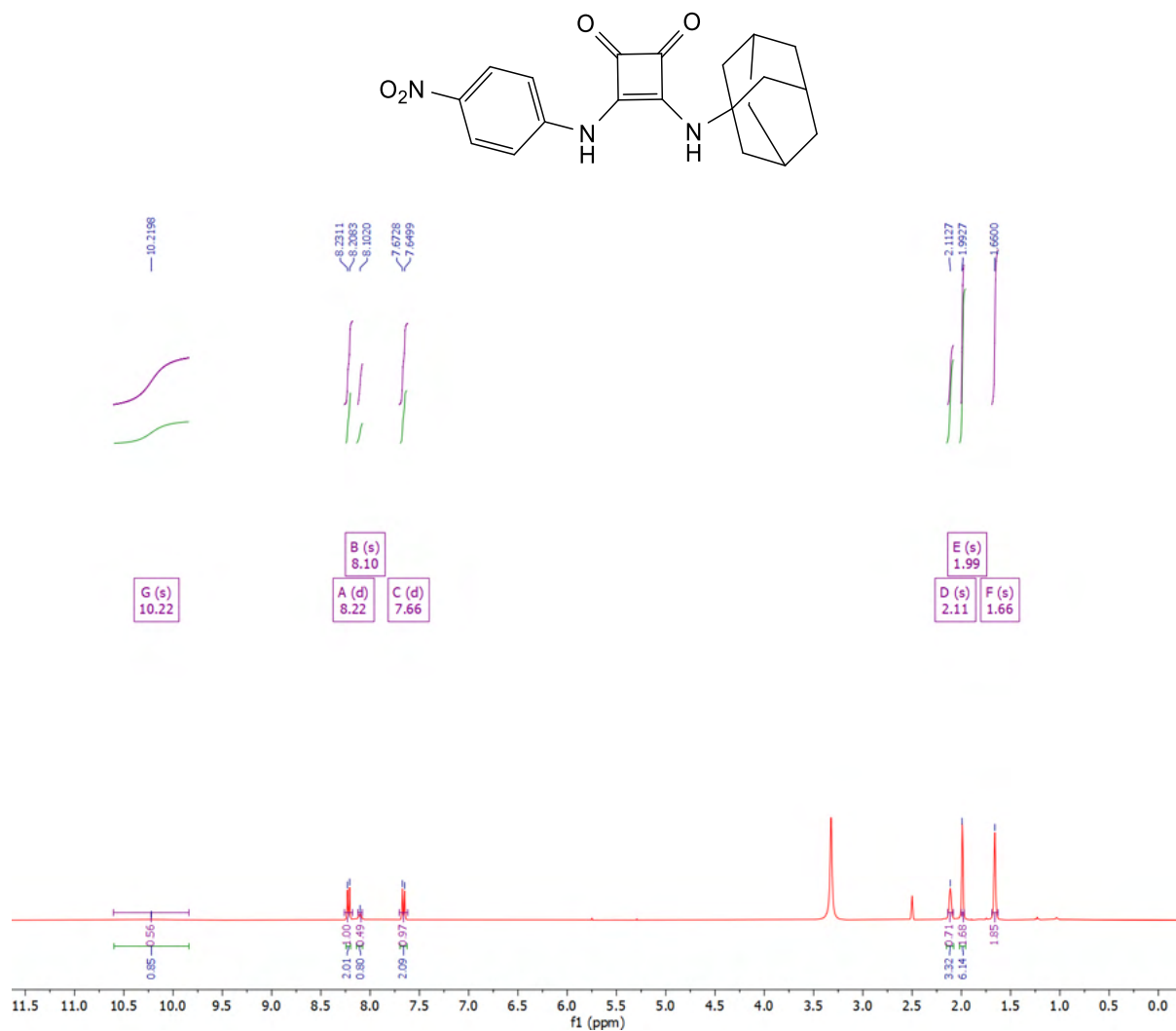
Figure S24. ^{1}H NMR (500 MHz) spectrum of N-(adamantyl)-N′-(4-nitrophenyl)squaramide in DMSO-d_6 at 298 K.
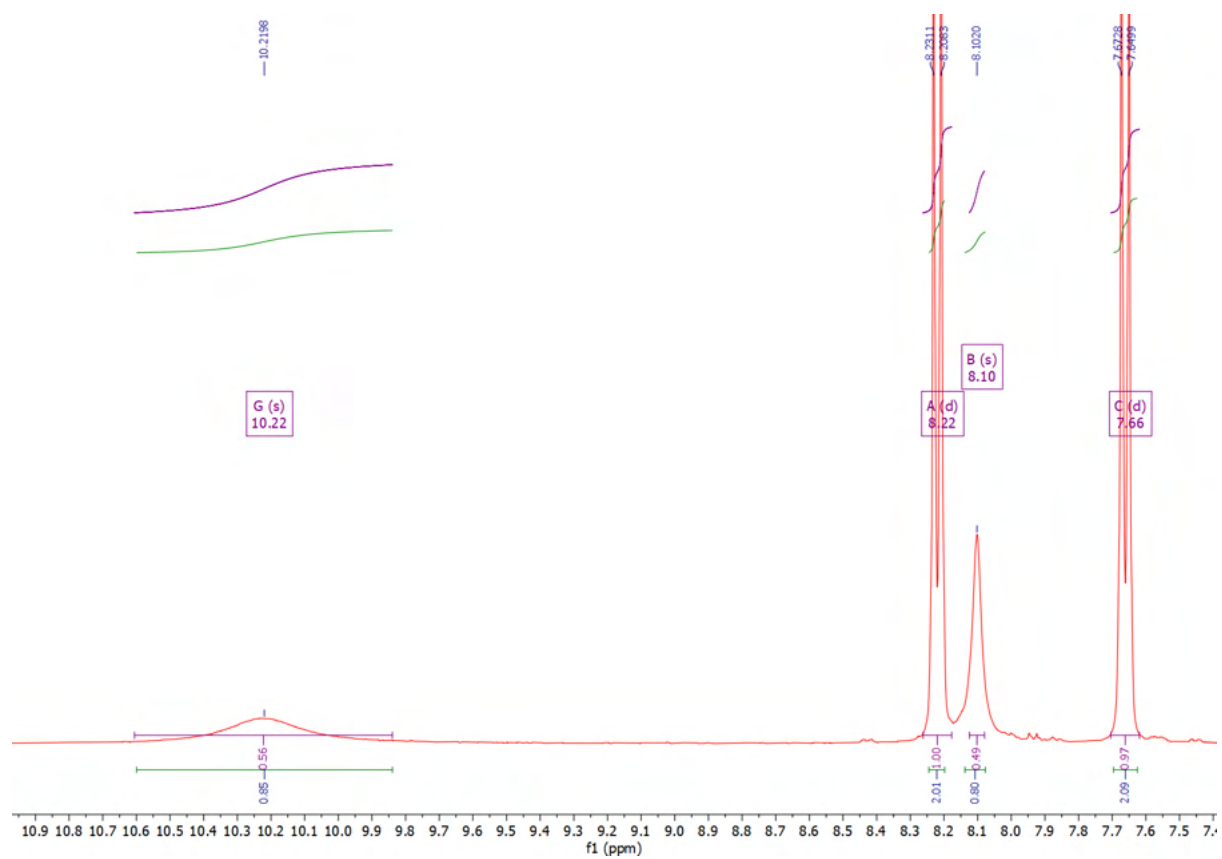
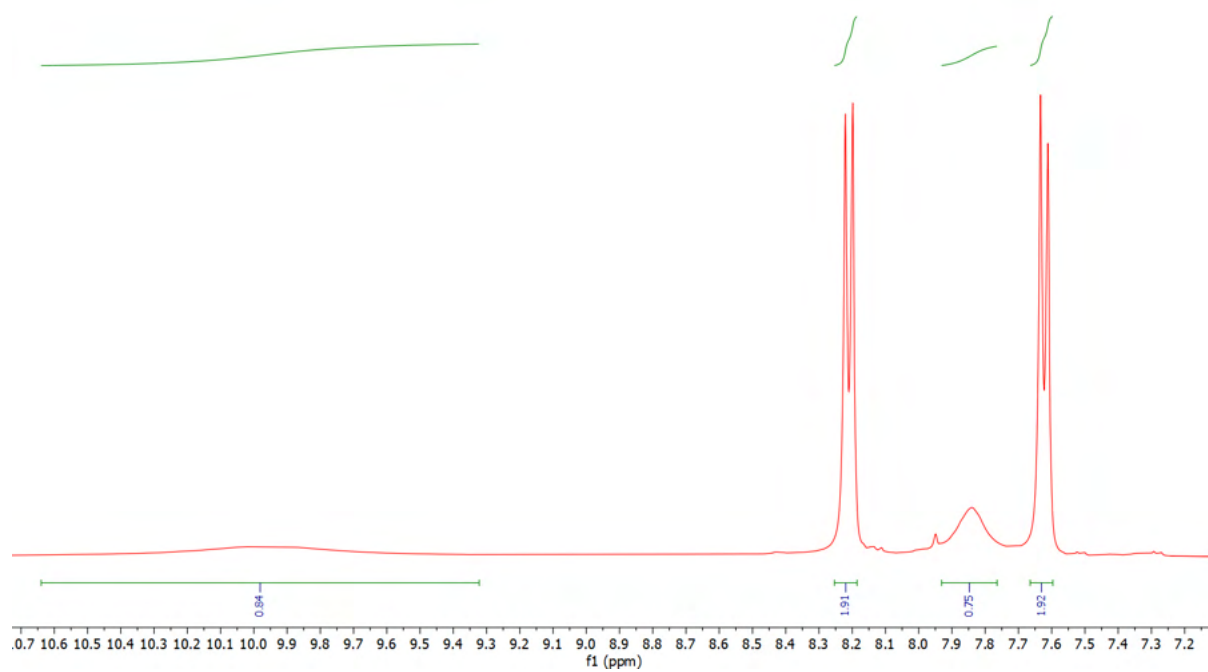**Figure S25.** ^{1}H NMR (500 MHz) spectrum of N-(adamantyl)-N'-(4-nitrophenyl)squaramide in DMSO-d_6 at 298 K. Zoomed in to display broad resonance attributed to the squaramide N−H proton.
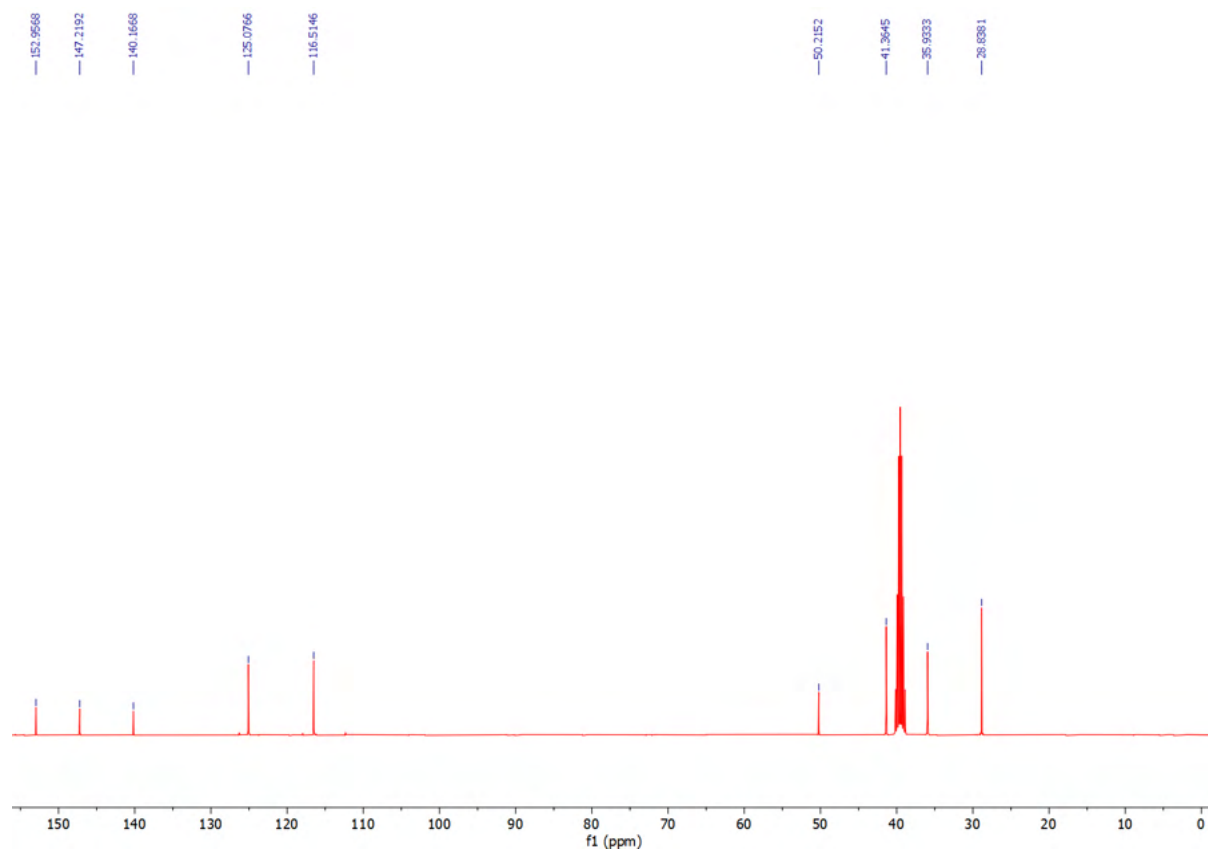
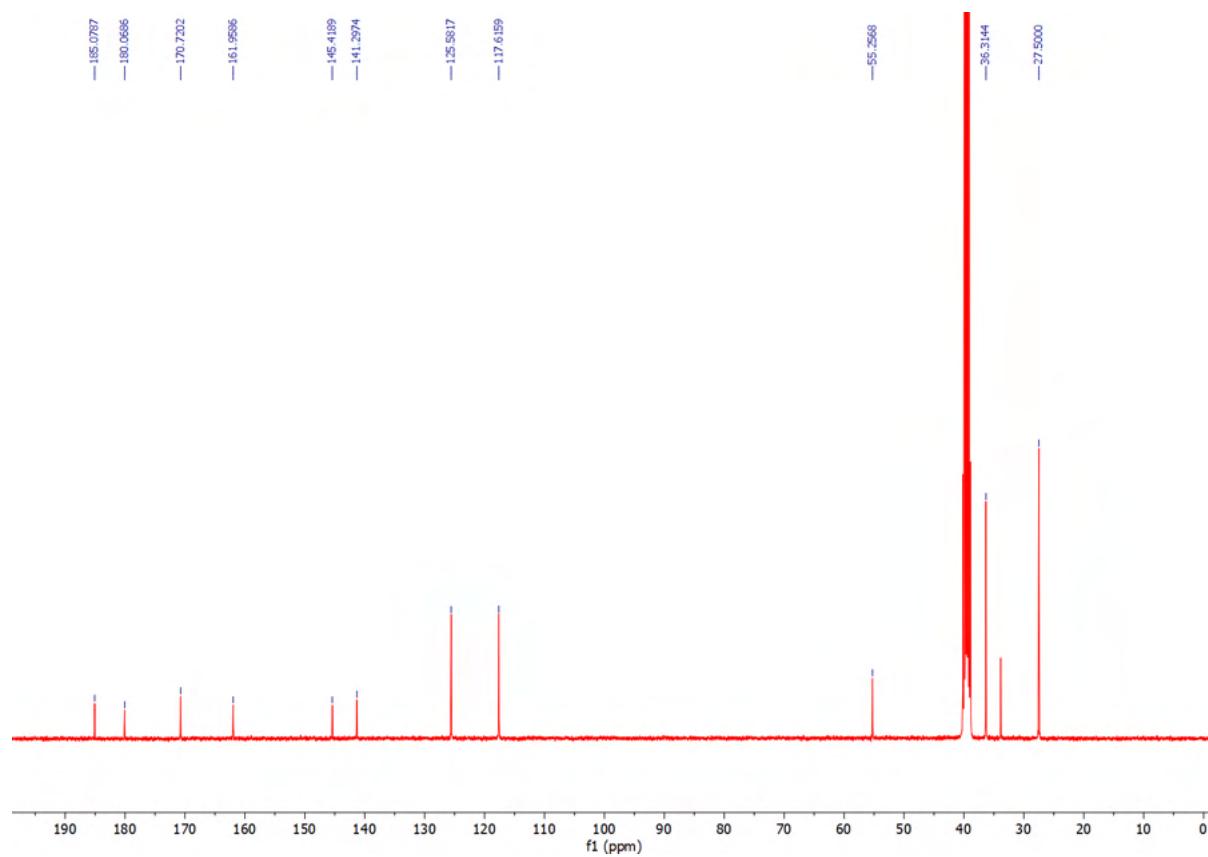**Figure S26**. ^{13}C NMR (101 MHz) spectrum of *N*-(adamantyl)-*N'*-(4-nitrophenyl)squaramide urea in DMSO-*d₆* at 298 K.
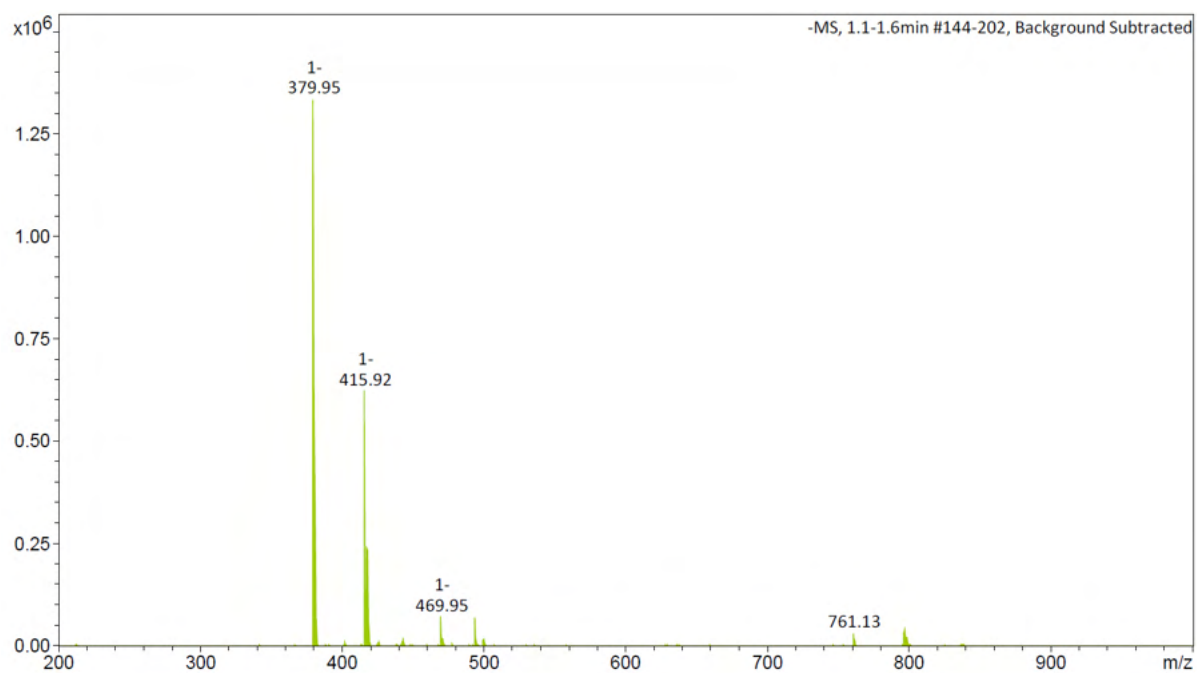

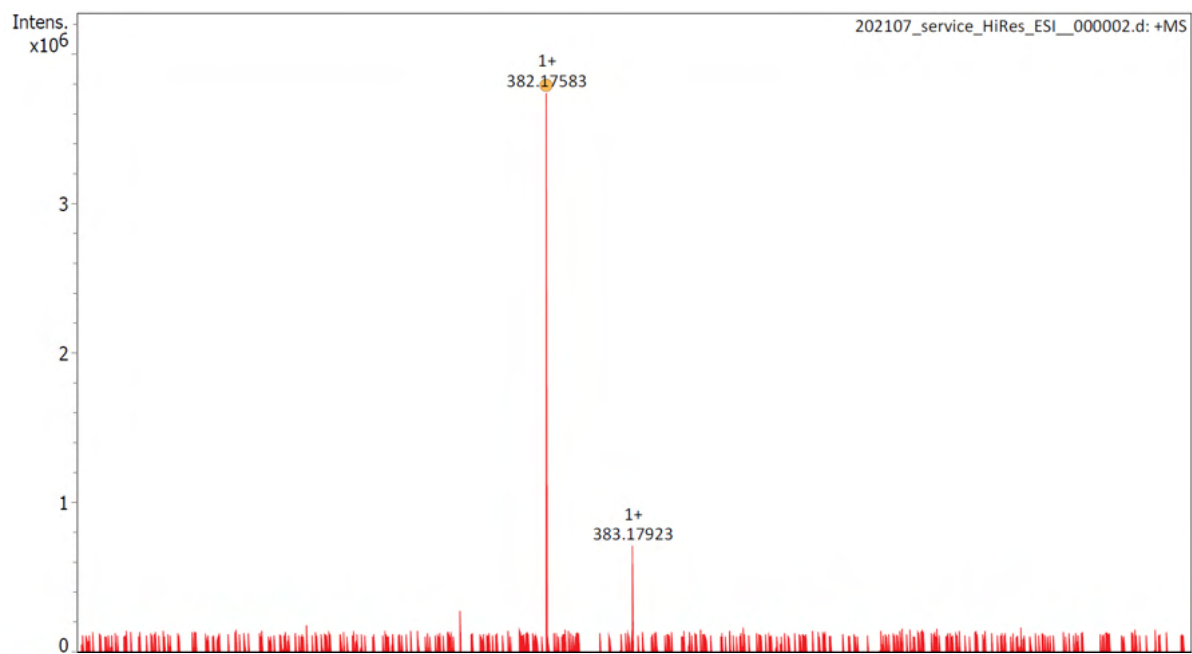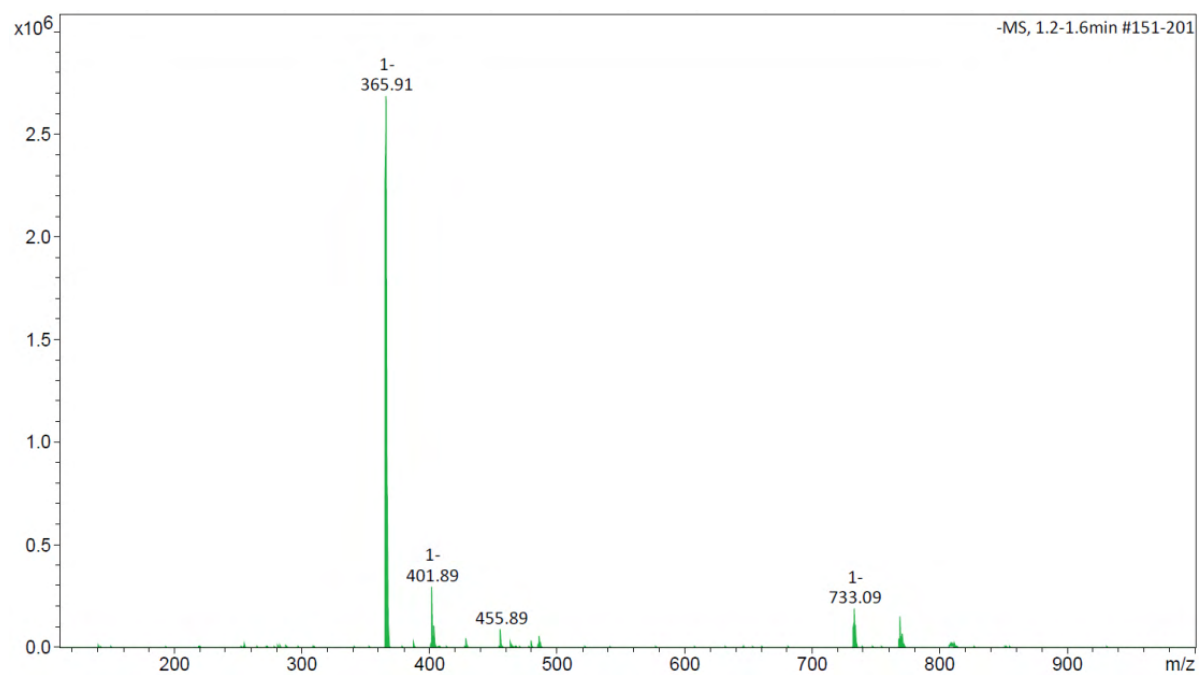**Figure S27**. LR-MS (ESI⁻) spectrum of *N*-(adamantyl)-*N'*-(4-nitrophenyl)squaramide.
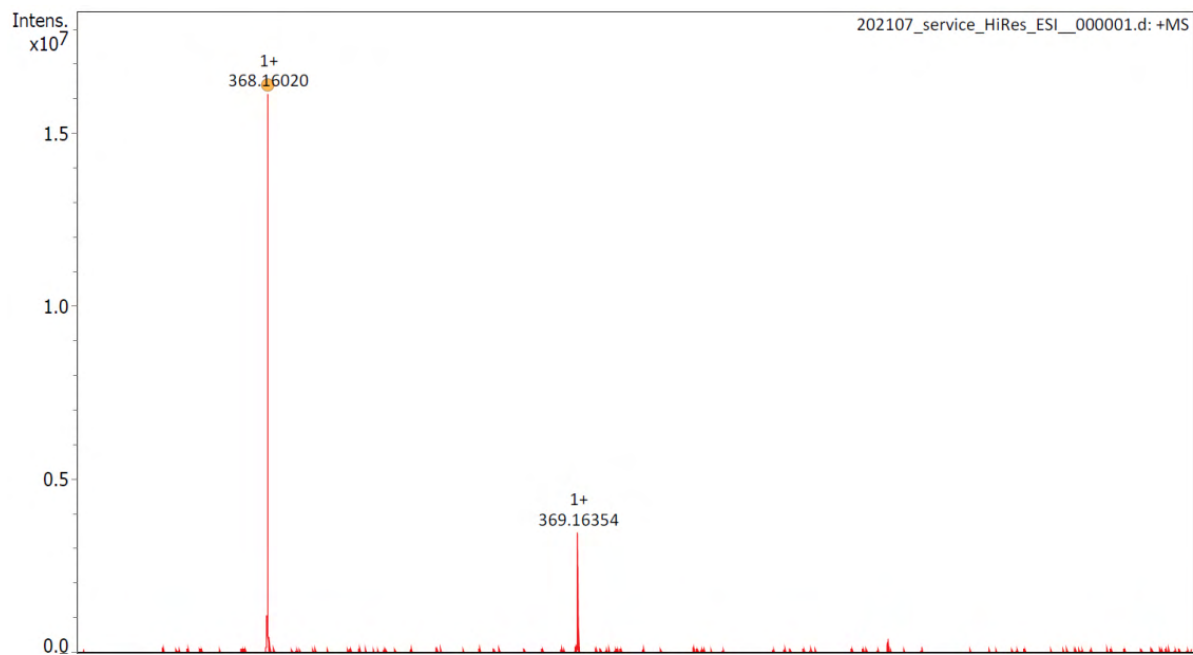
Figure S28. HR-MS (ESI⁺) spectrum of *N*-(adamantyl)-*N'*-(4-nitrophenyl)squaramide.

5. Single Crystal X-ray Diffraction

Crystals of free receptors **1** and **3** suitable for single crystal X-ray diffraction were obtained by vapour diffusion of H_2O into a DMSO solution saturated with either compound. The crystals were analysed using singe X-ray crystal diffraction, performed on an Agilent dual-beam Supernova™ System with a CCD Atlas detector on Mo/κa. Each specimen was mounted with the dual purpose cyro-protective adhesive Paratone-N and cool to 150 K with Oxford Cyrosystema Cobra Cooler. Compound **1** crystallised in the monocline space group $P2_1/c$ with one formula unit contained in the asymmetric unit (CDCC 2109212).
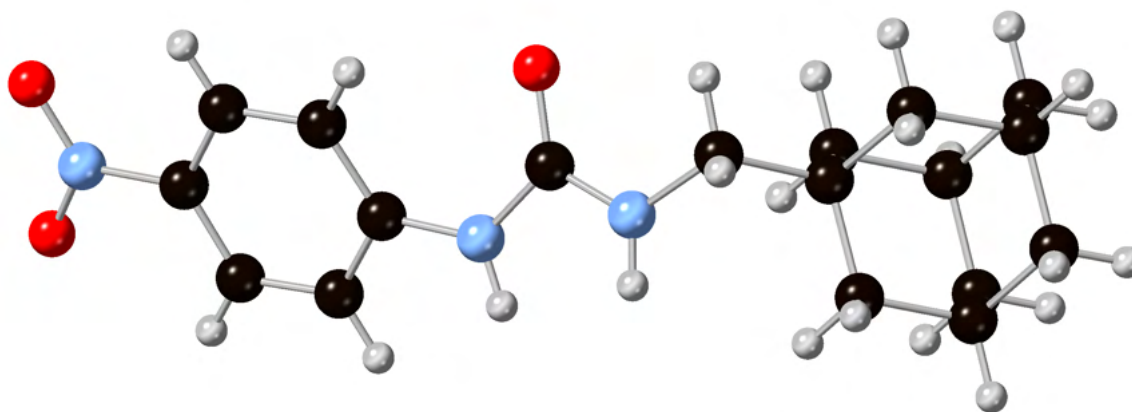
Figure S29. The X-ray crystal structure of receptor **1** (CDCC 2109212).

Table S1. Crystal data and structure refinement for **1**.

Identification code	21dm001
Empirical formula	$C_{18}H_{23}N_3O_3$
Formula weight	329.39
Temperature/K	150.00(18)
Crystal system	monoclinic
Space group	$P2_1/c$
a/Å	13.6962(3)
b/Å	13.6338(2)
c/Å	9.2710(2)
α/°	90
β/°	104.983(3)
γ/°	90
Volume/Å^3	1672.32(7)
Z	4
ϱ_{calc}g/cm^3	1.308
μ/mm^{-1}	0.090
F(000)	704.0
Crystal size/mm^3	0.563 × 0.328 × 0.243
Radiation	Mo Kα (λ = 0.71073)
2Θ range for data collection/°	5.442 to 56.56
Index ranges	$-18 \leq h \leq 18$, $-18 \leq k \leq 18$, $-12 \leq l \leq 12$
Reflections collected	26702
Independent reflections	4155 [R_{int} = 0.0255, R_{sigma} = 0.0166]
Data/restraints/parameters	4155/54/217
Goodness-of-fit on F^2	1.042
Final *R* indexes [I>=2σ (I)]	R_1 = 0.0560, wR_2 = 0.1415

Final *R* indexes [all data] | $R_1 = 0.0675$, $wR_2 = 0.1521$

Largest diff. peak/hole / e Å^{-3} | 0.50/-0.44

Table S2. Fractional Atomic Coordinates ($\times 10^4$) and Equivalent Isotropic Displacement Parameters ($\text{Å}^2 \times 10^3$) for **1**. U_{eq} is defined as 1/3 of the trace of the orthogonalised U_{IJ} tensor.

Atom	*x*	*y*	*z*	*U(eq)*
C1	4472.1(12)	4070.3(12)	3587(2)	34.5(4)
C2	4839.7(13)	4760.9(13)	2775(2)	39.7(4)
C3	4315.2(13)	5621.5(13)	2377(2)	35.7(4)
C4	3415.8(11)	5795.1(11)	2792.5(16)	25.5(3)
C5	3040.9(12)	5072.7(12)	3575.3(18)	30.0(3)
C6	3575.4(13)	4211.5(12)	3979.6(19)	34.1(4)
C7	2170.5(11)	7108.1(10)	2881.7(16)	23.3(3)
C8	995.6(12)	8496.8(11)	2485.6(19)	29.8(3)
C9	1314.1(11)	9569.6(10)	2736.9(16)	24.2(3)
C10	1464.7(12)	10037.5(11)	1315.9(17)	27.2(3)
C11	2281.3(18)	9675.1(13)	3968(2)	51.3(6)
C12	449.3(17)	10116.9(14)	3171(3)	47.9(5)
C13	1721.1(13)	11126.2(12)	1554(2)	34.0(4)
C14	2695.7(16)	11223.7(14)	2776(3)	64.3(7)
C15	2555(2)	10766.9(16)	4223(3)	76.8(9)
C16	883.5(15)	11663.2(12)	2038(2)	40.2(4)
C17	729(2)	11202.5(14)	3462(3)	56.7(6)
C18	1686(3)	11291.7(17)	4684(3)	86.3(11)
N1	5052.4(12)	3180.0(12)	4068(2)	46.2(4)
N2	2913.8(10)	6671.1(9)	2327.4(15)	27.5(3)
N3	1732.4(10)	7877.5(9)	2054.5(14)	27.0(3)
O1	4722.3(13)	2562.3(11)	4777(2)	63.2(5)
O2	5865.7(11)	3095.9(12)	3751(2)	66.9(5)
O3	1947.5(9)	6815.6(8)	4008.7(12)	31.6(3)

Table S3. Hydrogen Atom Coordinates ($\text{Å} \times 10^4$) and Isotropic Displacement Parameters ($\text{Å}^2 \times 10^3$) for **1**.

Atom	*x*	*y*	*z*	*U(eq)*
H2	5448.98	4643.44	2493.49	48
H3	4563.29	6100.8	1817.6	43
H5	2419.4	5173.02	3829.61	36

Atom	x	y	z	U(eq)
H6	3328.24	3721.41	4522.6	41
H8A	868.93	8234.12	3416.19	36
H8B	351.73	8463.68	1697.87	36
H10A	839.85	9961.77	500.51	33
H10B	2018.74	9696.57	1013.89	33
H11A	2836.74	9322.64	3686.75	62
H11B	2190.79	9381.52	4901.34	62
H12A	-177.8	10060.63	2354.49	57
H12B	324.5	9818.23	4079.79	57
H13	1809.71	11419.78	607.54	41
H14A	2877.89	11924.85	2942.96	77
H14B	3250.62	10885.48	2472.55	77
H15	3193.6	10834.9	5034.83	92
H16A	247.49	11624.83	1235.02	48
H16B	1065.77	12363.51	2217.19	48
H17	170.38	11551.18	3762.83	68
H18A	1590.19	10994.81	5612.51	104
H18B	1857.44	11992.8	4882.1	104
H2A	3086.64	6983.58	1600.37	33
H3A	1899.7	8009.58	1220.5	32

Crystals of compound **1** suitable for single crystal X-ray diffraction were also obtained in the presence of TBACl (20 molar equiv.). Crystals were prepared by slow evaporation of a saturated DMSO solution containing **1** and TBACl. The collection was carried out in the same manner as the parent molecule **1**. **1**·TBACl crystallised in the centrosymmetric triclinic P$\bar{1}$ space group (CDCC 2109213). Receptor **1** was found to form a 1:1 receptor:anion complex with TBACl, with coordinating hydrogen bonding interactions existing between chloride and the protons of the urea moiety (N⋯Cl distances: 3.145–3.278 Å, N–H⋯Cl angles: 150.5(7)–165.6(7) °) within the unit cell. The remaining bonds primarily extend outside the asymmetric unit, with large coordination created between the carbon donated hydrogen atoms an external chloride ion.
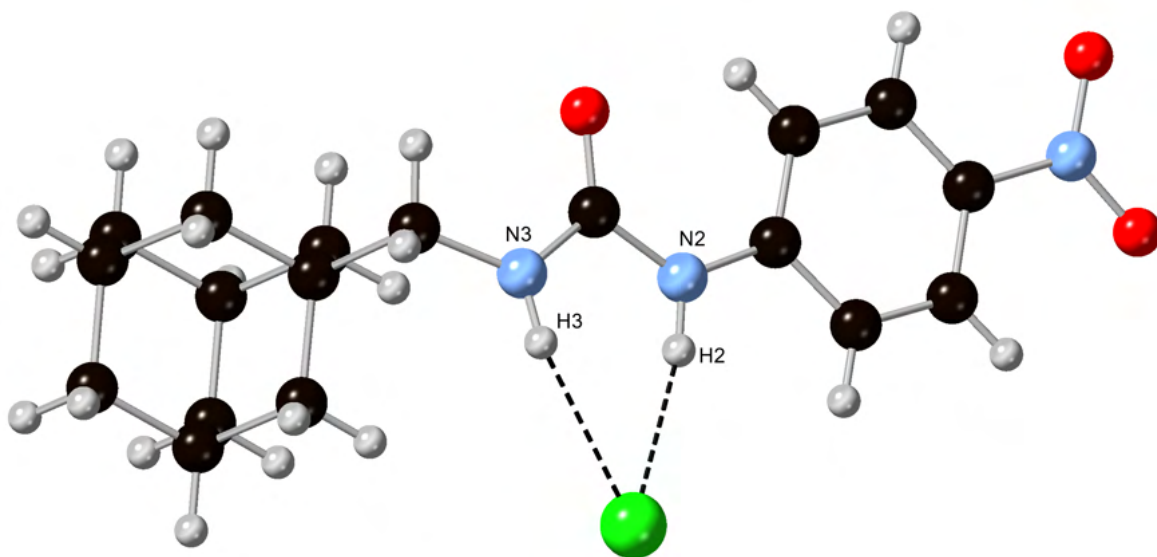
Figure S30. The X-ray crystal structure of receptor **1** in the presence of TBACl (CDCC 2109213). The chloride anion is coloured green, and the counterion is omitted for clarity. Dashed lines represent hydrogen bonds.

Table S4. Crystal data and structure refinement for **1**+TBACl.

Identification code	21bh013
Empirical formula	$C_{34}H_{59}ClN4O_3$
Formula weight	607.30
Temperature/K	150.0(2)
Crystal system	triclinic
Space group	P-1
a/Å	8.1181(2)
b/Å	13.6649(4)
c/Å	17.6062(6)
α/°	108.557(3)
β/°	100.746(2)
γ/°	95.887(2)
Volume/Å^3	1791.40(10)
Z	2

ϱ_{calc} g/cm^3	1.126
μ/mm^{-1}	0.143
F(000)	664.0
Crystal size/mm^3	0.91 × 0.74 × 0.53
Radiation	Mo Kα (λ = 0.71073)
2Θ range for data collection/°	5.018 to 52.742
Index ranges	-10 ≤ h ≤ 10, -17 ≤ k ≤ 17, -21 ≤ l ≤ 21
Reflections collected	25252
Independent reflections	7304 [R_{int} = 0.0292, R_{sigma} = 0.0291]
Data/restraints/parameters	7304/0/383
Goodness-of-fit on *F*^{2}	1.034
Final *R* indexes [I>=2σ (I)]	R_1 = 0.0422, wR_2 = 0.1050
Final *R* indexes [all data]	R_1 = 0.0562, wR_2 = 0.1144
Largest diff. peak/hole / e Å^{-3}	0.75/-0.28

Table S5. Fractional Atomic Coordinates (×10^4) and Equivalent Isotropic Displacement Parameters (Å^2×10^3) for **1**+TBACl. U_{eq} is defined as 1/3 of the trace of the orthogonalised U_{IJ} tensor.

Atom	*x*	*y*	*z*	*U(eq)*
Cl	1093.0(19)	7160.4(12)	5471.9(9)	28.4(3)
Cl'	4340.7(18)	5118.9(12)	2 541.1(9)	25.6(3)
C2'	4638(2)	4874.0(13)	3334.4(10)	31.5(4)
C2	11 96.8(19)	6429.6(12)	4733.5(10)	29.4(3)
C3	1 0 93.6(19)	6728.7(12)	4053.2(9)	27.0(3)
C4	8 8 6.4(18)	7752.4(12)	4096.8(9)	24.8(3)
C4'	3100(2)	4137.2(13)	3341.0(10)	30.8(4)
C5	800(2)	8474.1(12)	4852.1(10)	30.7(3)
C5'	3383(2)	3807.7(15)	4097.6(11)	41.9(4)
C6	892(2)	8172.3(13)	5532.1(10)	32.1(4)
C6'	6410.5(19)	6 817.9(12)	3151.1(9)	28.0(3)
C7	468(2)	8899.2(12)	3244.4(0)	28.3(3)
C7'	5081(2)	7516.(13)	3305.4(10)	36.4(4)
C8	2 59 2)	9711.5(12)	2180.1(10)	30.7(3)

Atom	x	y	z	U(eq)
C8'	5823(3)	8523.6(15)	4048.0(11)	48.6(5)
C9	1911(2)	10062.7(12)	1970.4(9)	26.0(3)
C9'	6062(3)	8360.4(19)	4859.3(12)	61.8(6)
C10'	7362.6(18)	5238.9(12)	2376.1(9)	26.1(3)
C10	3433(2)	10334.2(14)	2703.2(10)	36.8(4)
C11'	7117(2)	4211.6(14)	1671.9(11)	36.0(4)
C11	1737(2)	11049.6(13)	1742.8(10)	33.2(4)
C12'	8789(2)	3795.0(14)	1685.1(10)	34.8(4)
C12	2247(2)	9208.0(13)	1231.2(10)	35.2(4)
C13	3365(2)	11436.4 (14)	1526.1(12)	41.6(4)
C13′	8664(3)	2801.8(17)	962.7(14)	57.7(6)
C14	5066(2)	10707.7(16)	2480.9(13)	48.7(5)
C14′	5173.4(18)	5999.2(12)	1633.5(9)	25.0(3)
C15	6413(2)	6701.0(13)	1410.9(9)	30.9(4)
C15′	4870(3)	11692.0(15)	2258.8(14)	49.7(5)
C16	5618(2)	6778.6(15)	581.9(10)	40.6(4)
C16′	3871(3)	9588.1(15)	1010.4(12)	47.1(5)
C17	6823(3)	7414.6(19)	286.4(13)	60.8(6)
C17′	3670(3)	10572.4(15)	786.2(13)	51.1(5)
C18	5368(3)	9851.1(17)	1743.6(15)	57.1(6)
N1	1156.7(17)	6849.2(12)	6190.9(9)	35.0(3)
N2	5820.0(15)	5789.4(10)	2427.5(7)	23.1(3)
N3	759.5(16)	7970.7(10)	3374.5(8)	27.5(3)
O1	293.2(18)	8808.6(10)	2445.1(8)	32.0(3)
O2	936.1(18)	7480.9(11)	6823.2(8)	46.6(3)
O3	1413.8(18)	5957.0(10)	6135.2(8)	49.8(3)
Cl1*	364.0(17)	9689.0(9)	3789.4(7)	41.3(3)

Table S6. Hydrogen Atom Coordinates (Å×10⁴) and Isotropic Displacement Parameters (Å²×10³) for **1**+TBACl.

Atom	x	y	z	U(eq)
H1'A	4041.96	4448	2071.47	31
H1'B	3345.16	5479.53	2516.29	31
H2'A	4838.51	5532.59	3811.62	38
H2'B	5663.24	4542.87	3384.07	38
H2	1336.5	5736.1	4698.84	35
H3	1163.58	6234.91	3544.63	32

Atom	x	y	z	U(eq)
H4'A	2095.63	4490.75	3326.18	37
H4'B	2853.26	3504.2	2839.62	37
H5	677.35	9172.56	4895.55	37
H5'A	4428.66	3508.33	4139.95	63
H5'B	2414.4 3	3281.95	4047.67	63
H5'C	3488 .31	4420.75	4592.07	63
H6	818.22	8659.77	6042.58	38
H6'A	6817 .06	6654.63	3655.78	34
H6'B	7393 .94	7217.42	3057.18	34
H7'A	4094.07	7132.95	3409.24	44
H7'B	4676.62	7700.06	2810.15	44
H8A	26.18	10301.78	2623.02	37
H8B	-689.15	9539.22	1689.08	37
H8'A	6936.97	8824.42	3991.41	58
H8'B	5054.88	9040.27	4041.73	58
H9'A	4964.58	8064.29	4922.15	93
H9'B	6511.5	9033.74	5305.06	93
H9'C	6864 .98	7876.34	4882.44	93
H10A	8305 .91	5724.91	2334.69	31
H10B	7725 .97	5108.08	2898.75	31
H10C	3562 .77	9708.83	2862.48	44
H10D	3232 .88	10892.64	3179.16	44
H11A	6725.38	4318.87	1141.66	43
H11B	6235.94	3694.48	1723.09	43
H11C	759.6	10888.89	1266.5	40
H11D	1515.14	11607.62	2212.54	40
H12A	9683.36	4339.29	1676.86	42
Hl2B	9136.96	3652.95	2204.03	42
H12C	2367.19	8566.31	1368.26	42
H12D	1270.27	9032.41	752.34	42
H13	3233.24	12079.12	1381.03	50
H13A	7787.48	2257.53	970.16	87
H13B	9763.05	2561.82	1003.49	87
H13C	8359.07	2943.49	447.22	87
H14	6054.4	10872.76	2961.94	58
H14A	4832.34	5318.37	1174.76	30
H14B	4139.03	6318.34	1680.38	30
H15A	7476.66	6410.61	1380.39	37
H15B	6698.22	7407.23	1839.6	37
Hl5C	4680.89	12254.2	2735.58	60
H15D	5922.42	11943.94	2119.71	60

Atom	x	y	z	$U(eq)$
H16A	5256.38	6063.69	167.75	49

Compound **3** crystallised in the monoclinic space group *C*2/*c* with one formula unit contained in the asymmetric unit (CDCC 2109211). Close hydrogen bonds exist between the squaramide motifs of adjacent units (N2⋯O3: 2.877 Å, and N3⋯O4: 2.977 ⋯Å), forming an anti-parallel homogenous synthon, this hydrogen bond motif forms along the c-axis, creating sheets of transporters a 242 packing formation (respective to the b-axis).
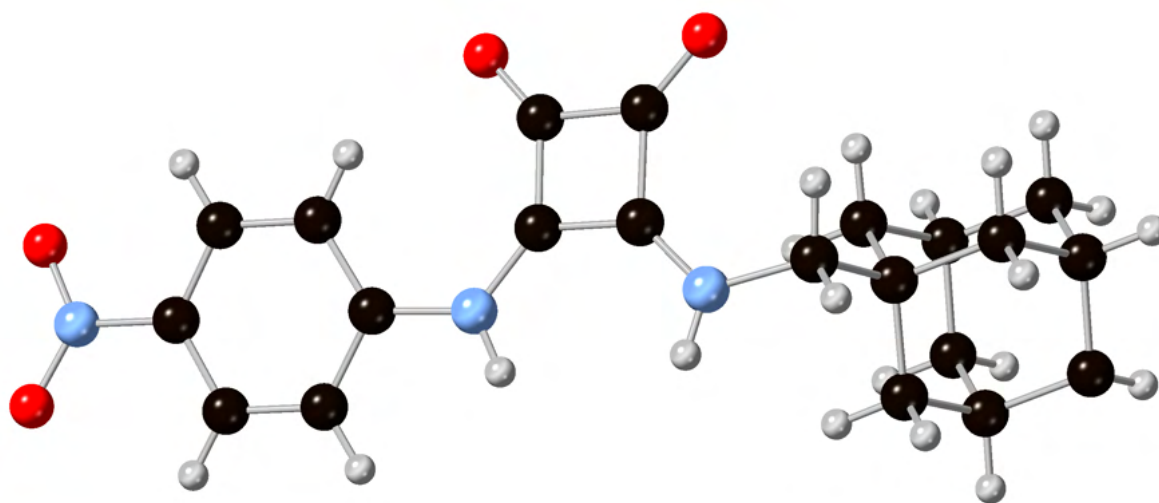

Figure S31. The X-ray crystal structure of receptor **3** (CDCC 2109211).

Table S7. Crystal data and structure refinement for **3**.

Identification code	21bh014
Empirical formula	$C_{21}H_{23}N_3O_4$
Formula weight	381.42
Temperature/K	150.0(2)
Crystal system	monoclinic
Space group	C2/c
a/Å	42.9415(11)
b/Å	6.2417(2)
c/Å	13.2277(3)
α/°	90
β/°	94.680(2)
γ/°	90
Volume/Å³	3533.57(17)
Z	8
ϱ_{calc}g/cm³	1.434

μ/mm^{-1}	0.101
F(000)	1616.0
Crystal size/mm^3	0.374 × 0.325 × 0.168
Radiation	Mo Kα (λ = 0.71073)
2Θ range for data collection/°	5.712 to 52.742
Index ranges	-53 ≤ h ≤ 53, -7 ≤ k ≤ 7, -16 ≤ l ≤ 16
Reflections collected	25030
Independent reflections	3615 [R$_{int}$ = 0.0344, R$_{sigma}$ = 0.0204]
Data/restraints/parameters	3615/0/253
Goodness-of-fit on F^2	1.029
Final R indexes [I>=2σ (I)]	R$_1$ = 0.0397, wR$_2$ = 0.0943
Final R indexes [all data]	R$_1$ = 0.0471, wR$_2$ = 0.0990
Largest diff. peak/hole / e Å^{-3}	0.30/-0.17

Table S8. Fractional Atomic Coordinates (×10^4) and Equivalent Isotropic Displacement Parameters (Å^2×10^3) for **3**. U_{eq} is defined as 1/3 of of the trace of the orthogonalised U$_{IJ}$ tensor.

Atom	x	y	z	U(eq)
C21	5499.6(3)	2949(2)	4874.3(11)	21.9(3)
C1	8029.1(3)	3413(2)	6886.8(10)	20.5(3)
C2	7867.4(3)	5158(2)	6473.0(10)	20.7(3)
C3	7560.2(3)	4918(2)	6089.5(10)	19.6(3)
C4	7413.3(3)	2933(2)	6151.0(9)	16.2(3)
C5	7584.0(3)	1165(2)	6545.4(10)	18.7(3)
C6	7892.9(3)	1404(2)	6910.6(10)	20.9(3)
C7	6884.9(3)	4122(2)	5511.4(9)	16.6(3)
C8	6857.9(3)	6463(2)	5479.9(10)	17.8(3)
C9	6535.6(3)	6228(2)	4986.5(10)	19.4(3)
C10	6571.7(3)	3863(2)	5088.7(10)	17.8(3)
C11	6054.5(3)	2532(2)	4514.0(11)	21.2(3)
C12	5831.3(3)	2491(2)	5361.1(10)	18.5(3)
C13	5919.0(3)	4214(2)	6166.2(10)	20.2(3)
C14	5683.2(3)	4221(2)	6973.7(11)	24.2(3)
C15	5355.3(3)	4673(2)	6471.7(12)	28.0(3)
C16	5265.3(3)	2930(2)	5685.9(12)	24.9(3)
C17	5269.5(3)	740(3)	6205.9(12)	28.7(3)
C18	5598.3(3)	293(2)	6706.7(11)	25.9(3)
C19	5830.8(3)	293(2)	5887.4(11)	22.0(3)
C20	5688.1(4)	2032(3)	7497.0(11)	28.2(3)
N1	8348.2(3)	3716(2)	7343.2(9)	28.3(3)
N2	7098.3(3)	2614.1(17)	5823.0(8)	16.8(2)

Atom	x	y	z	U(eq)
N3	6385.3(3)	2230.9(18)	4876.5(9)	19.9(3)
O1	8505.6(3)	2124(2)	7565.8(9)	37.1(3)
O2	8440.4(3)	5561(2)	7492.1(10)	46.8(3)
O3	7016.6(2)	8041.2(15)	5742.2(7)	22.1(2)
O4	6336.7(2)	7494.0(16)	4655.3(8)	25.7(2)

Table S9. Hydrogen Atom Coordinates ($\text{Å} \times 10^4$) and Isotropic Displacement Parameters ($\text{Å}^2 \times 10^3$) for **3**.

Atom	x	y	z	U(eq)
H21A	5495.56	4364.86	4535.7	26
H21B	5440.72	1848.21	4354.9	26
H2	7966.71	6515.62	6451.93	25
H3	7449.39	6101.21	5784.97	24
H5	7487.08	-201.66	6561.69	22
H6	8010.02	209.01	7173.89	25
H11A	5992.76	1389.17	4018.64	25
H11B	6031.8	3922.15	4155.05	25
H13A	6130.81	3923.9	6489.72	24
H13B	5921.59	5639.25	5838.07	24
H14	5741.42	5358.29	7487.21	29
H15A	5202.56	4695.49	6993.3	34
H15B	5351.87	6092.45	6136.9	34
H16	5050.95	3223.8	5361.98	30
H17A	5210.42	-388.22	5699.89	34
H17B	5116.16	721.07	6725.62	34
H18	5601.07	-1138.94	7046.26	31
H19A	5772.34	-832.79	5379.87	26
H19B	6042.97	-31.29	6199.45	26
H20A	5538.58	2024.6	8028.42	34
H20B	5899.5	1741.3	7824.24	34
H2A	7031.36	1281.3	5819.05	20
H3A	6459.74	921.99	4952.53	24

6. Proton NMR Titration Anion Binding Studies

6.1 Overview and Procedures

Proton NMR titrations were performed on a Bruker Avance DPX 400 spectrometer. For NMR titrations with chloride, a constant host concentration was maintained (2.0 mM) using a prepared host solution to dissolve the guest (as TBACl) to make the guest stock solution. Over the course of the titration, Hamiltonian Microlitre syringes were used to add aliquots of the guest stock solution to the NMR sample of the host solution. Chloride was added as the tetrabutylammonium (TBA) salt, purchased from Merck, after being dried under high vacuum (< 1.0 mmHg) for 24 h. Stock solutions of the host were prepared in a relevant solution to the experiment. The host stock solutions (600 µL) were transferred to an air-tight screwcap NMR sample tube (5 mm ID), and the same host stock solution was used to prepare the standard guest titrant solutions containing either 0.1 M, or 1 M of TBACl. This ensured a constant concentration of the host for the duration of the titration experiment.

Over the course of the titration, small aliquots (2–200 µL) of the standard guest solution were added to the host solution in the NMR tube. For each titration, 16–20 data points were collected. The number of equiv. of guest present at the end of each titration is labelled in the stacked plots. Before collecting each data point, an aliquot of the standard guest solution was added, and the sample was thoroughly mixed in the NMR tube. The system was allowed to equilibrate for up to 2 min inside the NMR probe before the spectra was collected. Throughout each titration experiment, all parameters of the NMR spectrometer remained constant.

In all cases, the proton resonances were monitored for changes in chemical shift. When possible, two or more resonances were followed, allowing several data sets to determine the association constant (Ka). Global fitting takes into account all data sets at the same time and improves the quality of the non-linear curve fitting. The supramolecular.org web applet was used to fit the titration data with chloride to a 1:1 model.[1]

6.1 Titration Data with TBACl Guest
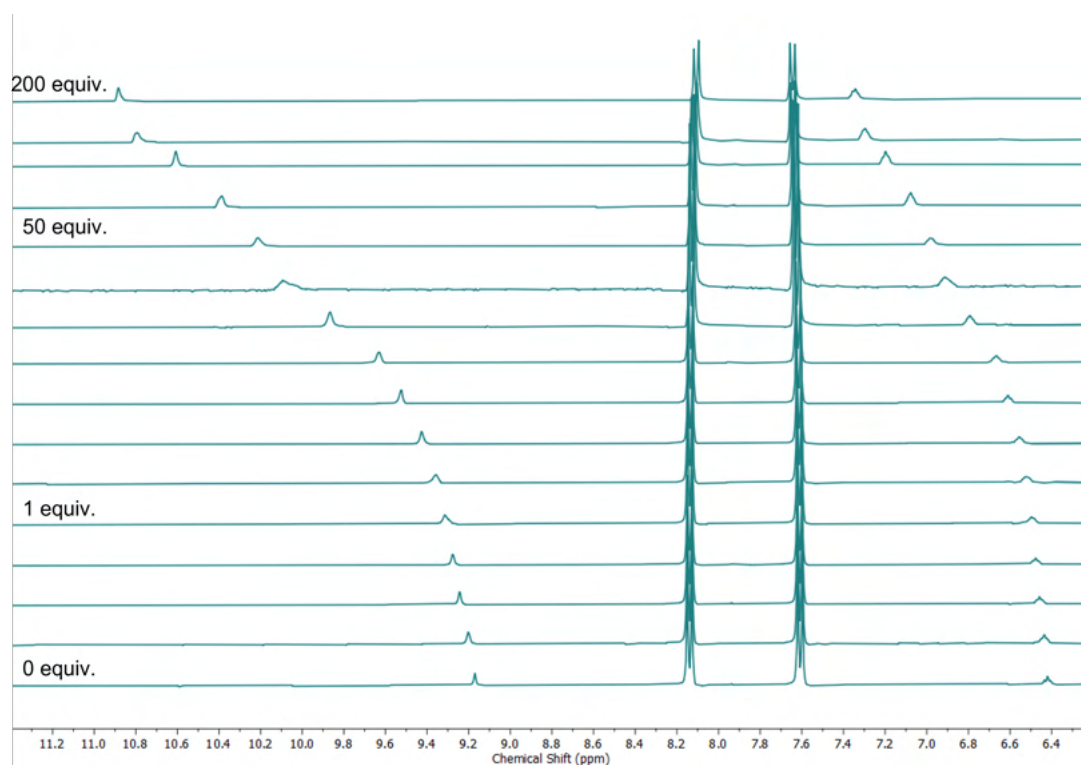
Figure S32. ^1H NMR titration spectra as a stack plot for **1** (2 mM) + TBACl (0–200 equiv.) in DMSO-d$_6$ /0.5% D$_2$O at 298 K.
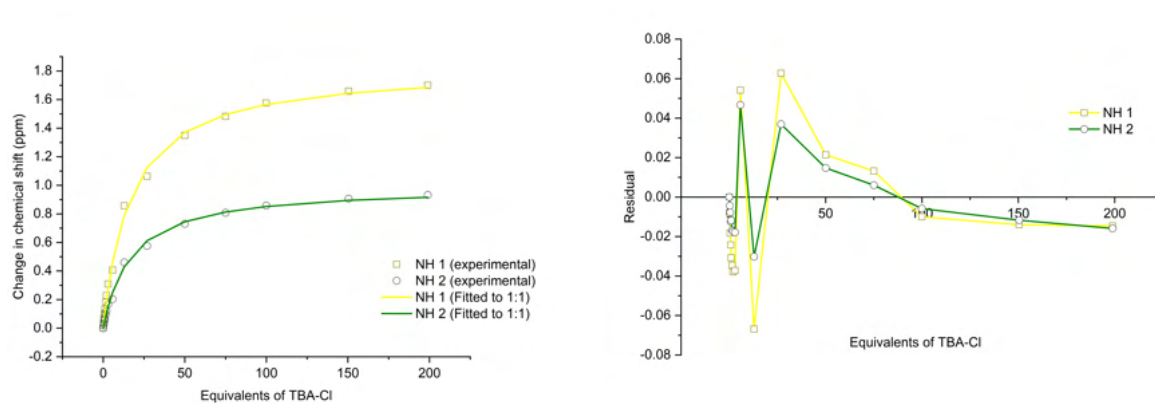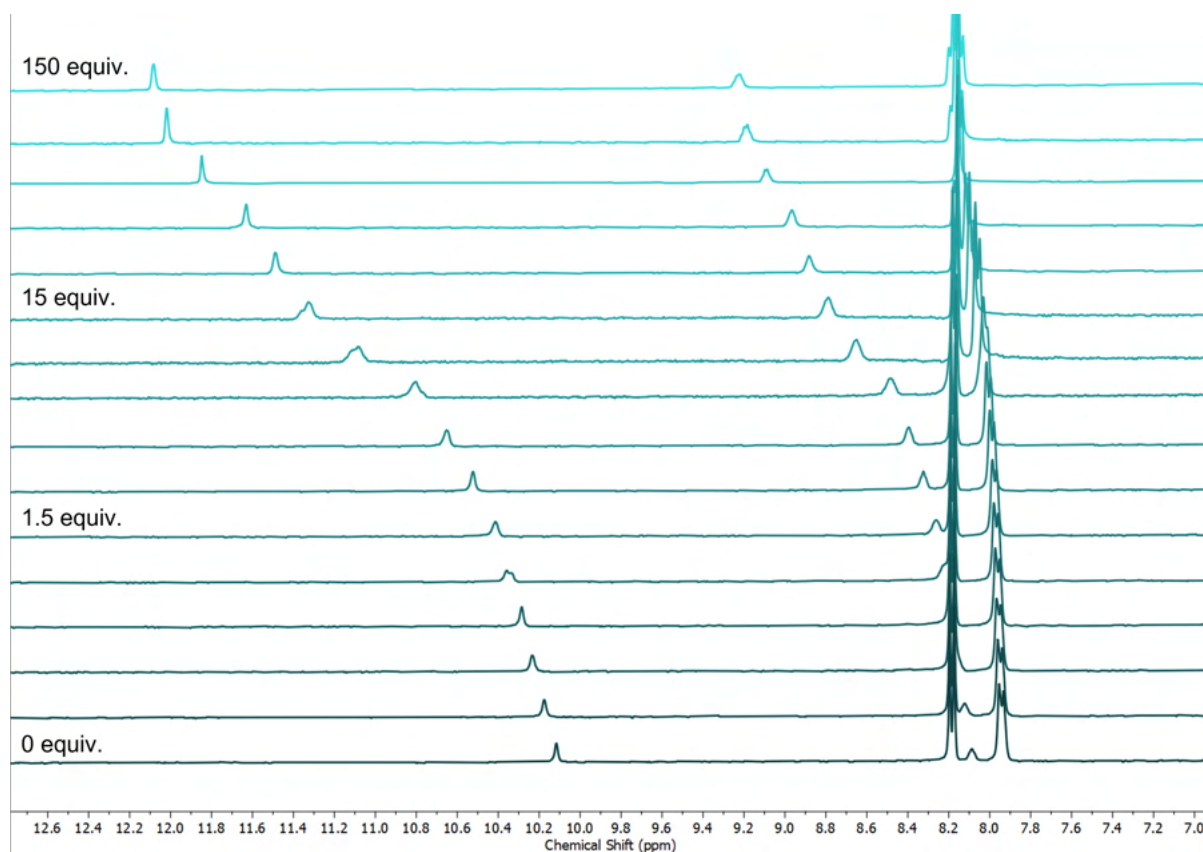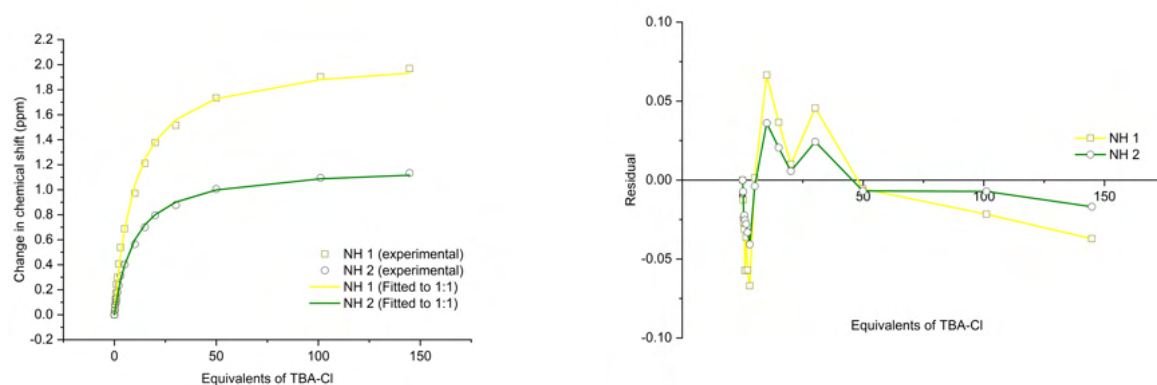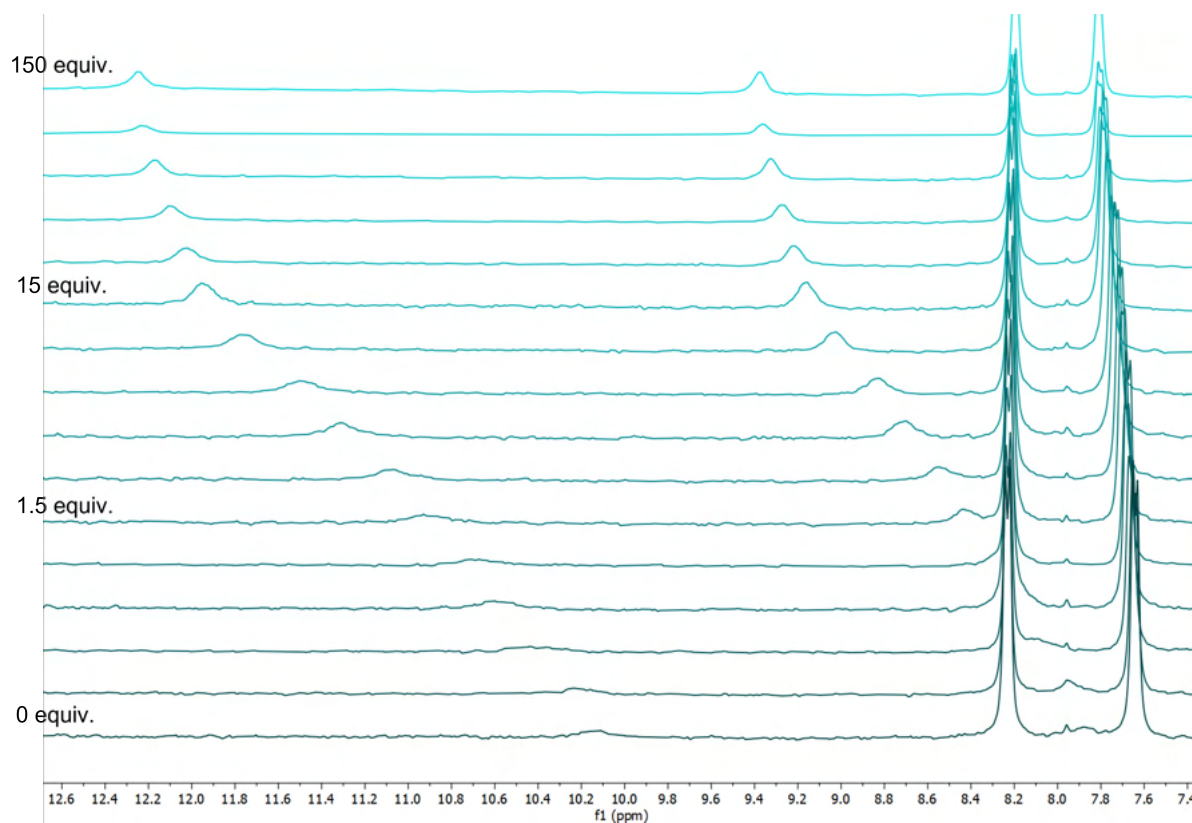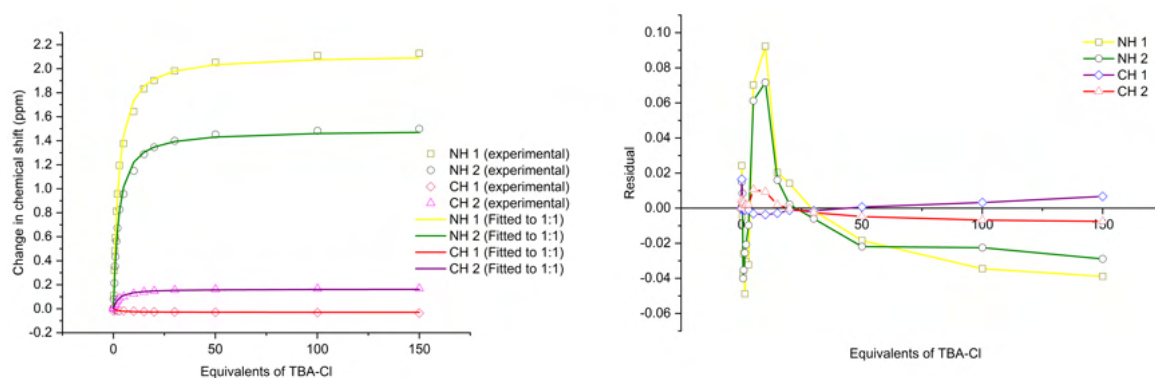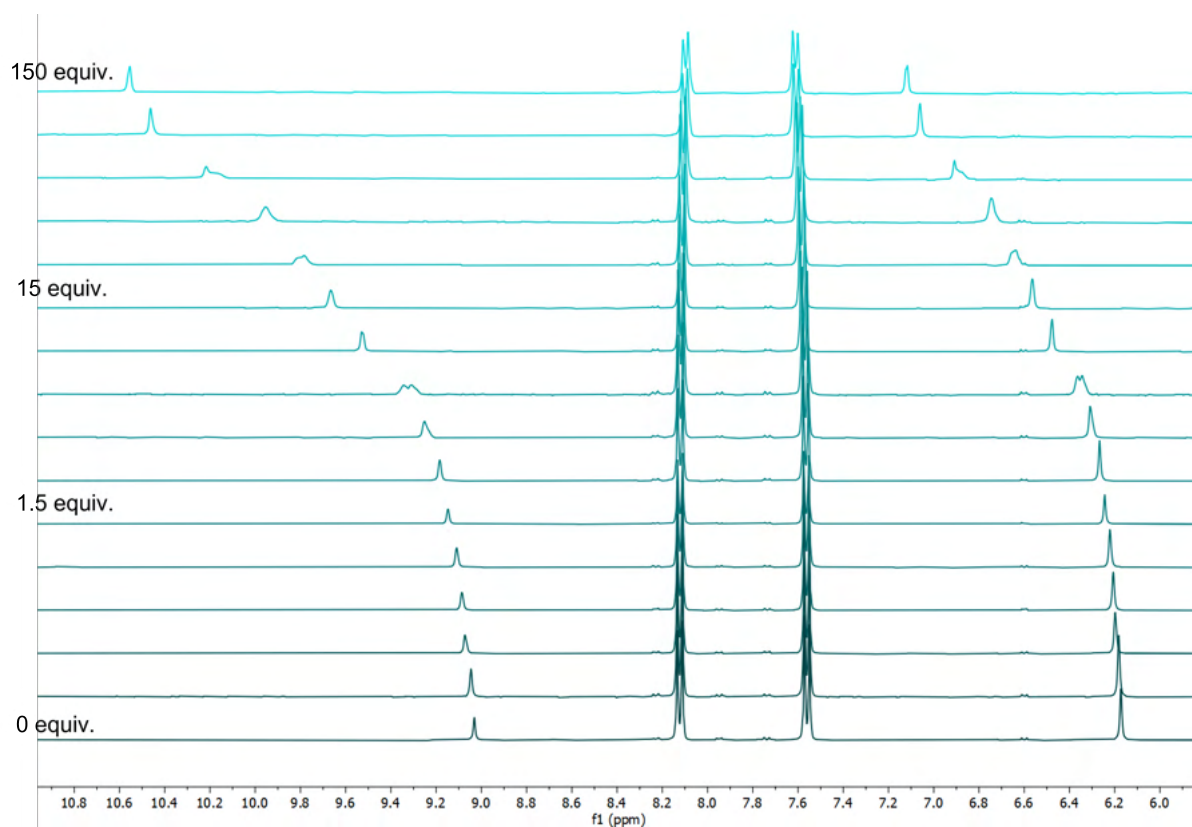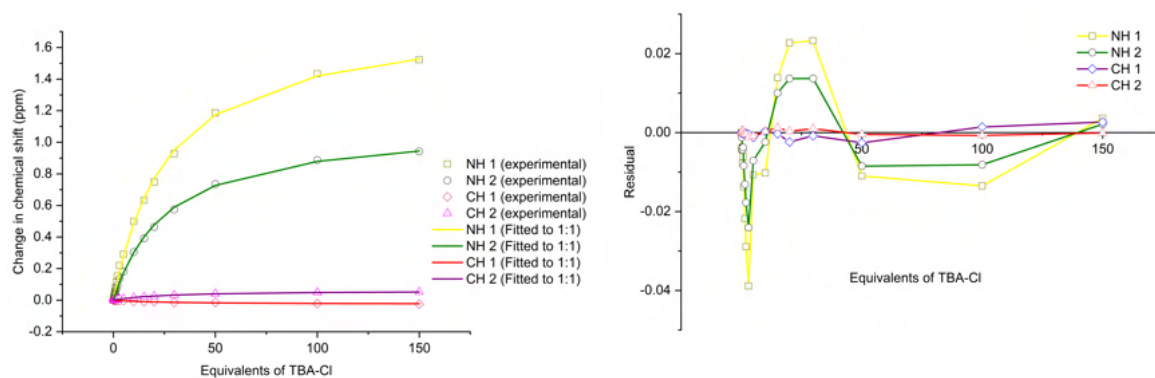

Figure S33. Fitted binding isotherm of **1** + TBACl showing the change in chemical shift of NH protons fitted to the 1:1 binding model (left). K_a = 33.69 M^{-1}. Residual plot showing the random error obtained from the binding isotherm fitting (right). Covariance of fit (cov$_{fit}$) = 2.51 x 10^{-3}. Link to Bindfit fitting: http://app.supramolecular.org/bindfit/view/3d7ecc84-f990-4b32-bd25-84853ea2c174.

Figure S34. ^{1}H NMR titration spectra as a stack plot for **2** (2 mM) + TBACl (0–150 equiv.) in DMSO-d$_6$ /0.5% D$_2$O at 298 K.

.

Figure S35. Fitted binding isotherm of **2** + TBACl showing the change in chemical shift of the NH protons fitted to the 1:1 binding model (left). K_a = 47.84 M^{-1}. Residual plot showing the random error obtained from the binding isotherm fitting (right). Covariance of fit (cov$_{fit}$) = 2.69 x 10^{-3}. Link to Bindfit fitting: http://app.supramolecular.org/bindfit/view/0b1005ac-fdd7-4d45-9405-193794fc5777.

Figure S36. ^{1}H NMR titration spectra as a stack plot for **3** (2 mM) + TBACl (0–150 equiv.) in DMSO-d$_6$ /0.5% D$_2$O at 298 K.

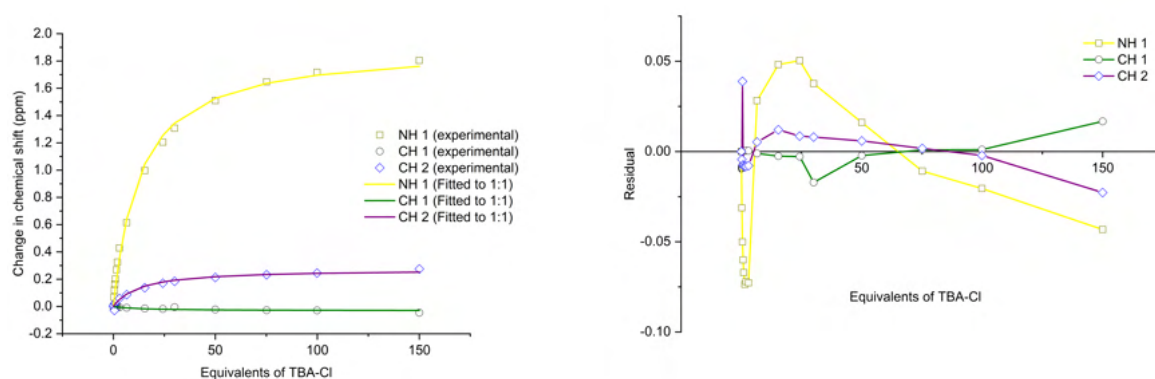**Figure S37**. Fitted binding isotherm of **3** + TBACl showing the change in chemical shift of NH and aromatic CH protons fitted to the 1:1 binding model (left). K_a = 249.09 M^{-1}. Residual plot showing the random error obtained from the binding isotherm fitting (right). Covariance of fit (c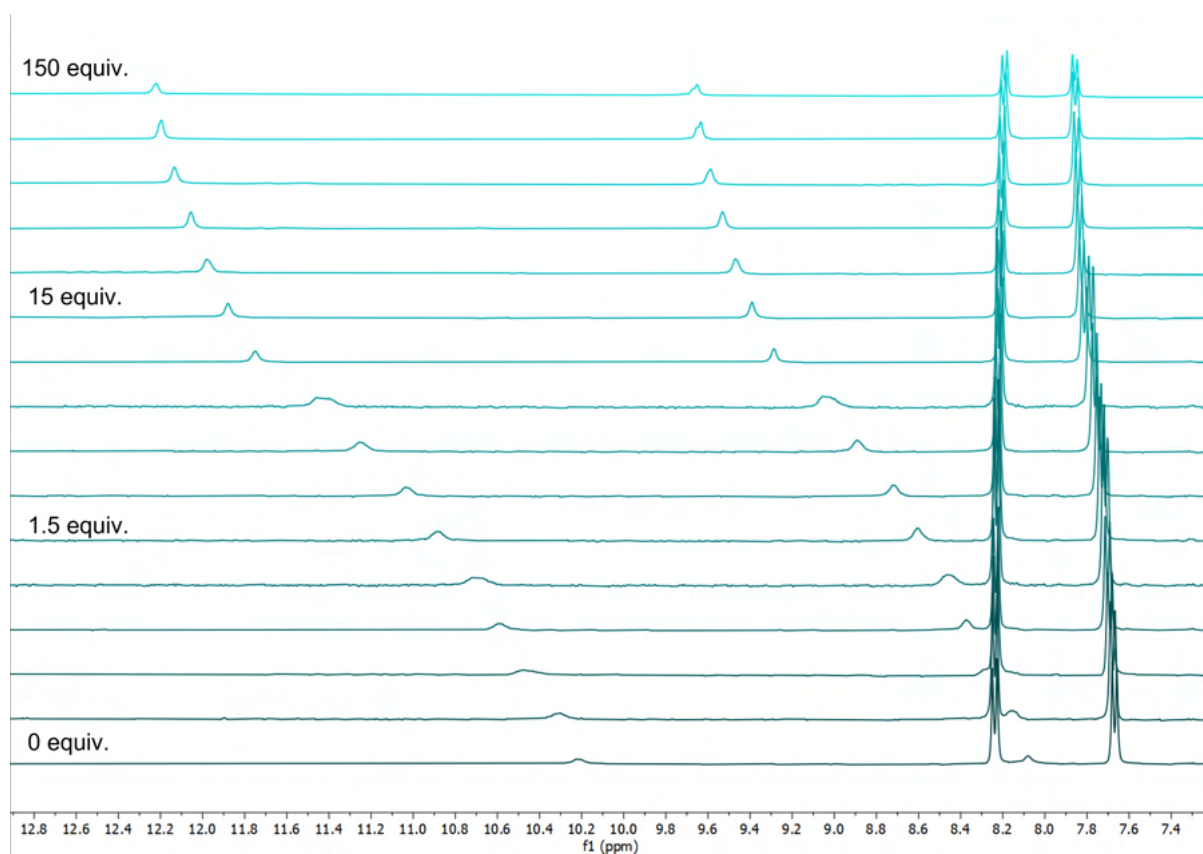ov$_{fit}$) = 1.34 x 10^{-3}. Link to Bindfit fitting: http://app.supramolecular.org/bindfit/view/1c356b9b-999a-4412-9c0e-31ceadb72649.

Figure S38. ^{1}H NMR titration spectra as a stack plot for **4** (2 mM) + TBACl (0–150 equiv.) in DMSO-d$_6$ /0.5% D$_2$O at 298 K.
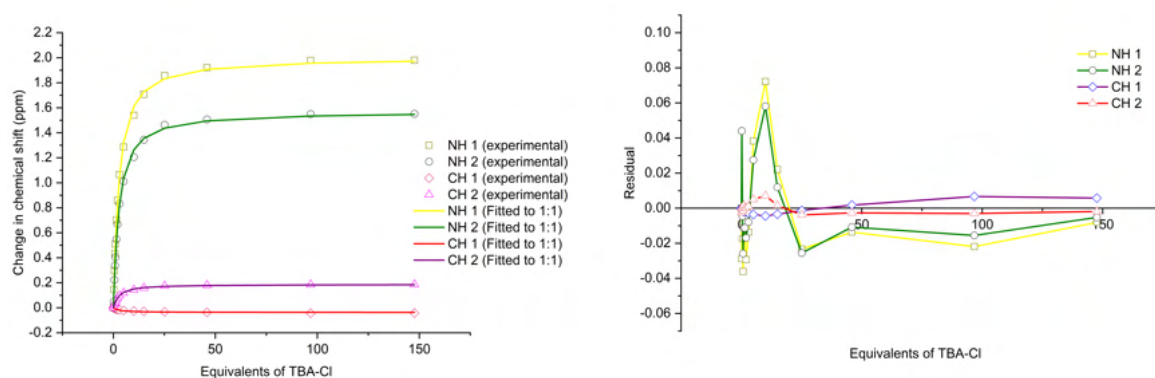

Figure S39. Fitted binding isotherm of **4** + TBACl showing the change in chemical shift of NH and aromatic CH protons fitted to the 1:1 binding model (left). K_a = 21.29 M^{-1}. Residual plot showing the random error obtained from the binding isotherm fitting (right). Covariance of fit (cov$_{fit}$) = 7.48 x 10^{-4}. Link to Bindfit fitting: http://app.supramolecular.org/bindfit/view/db17772a-eff5-4005-975d-5d5dbca35bf5.
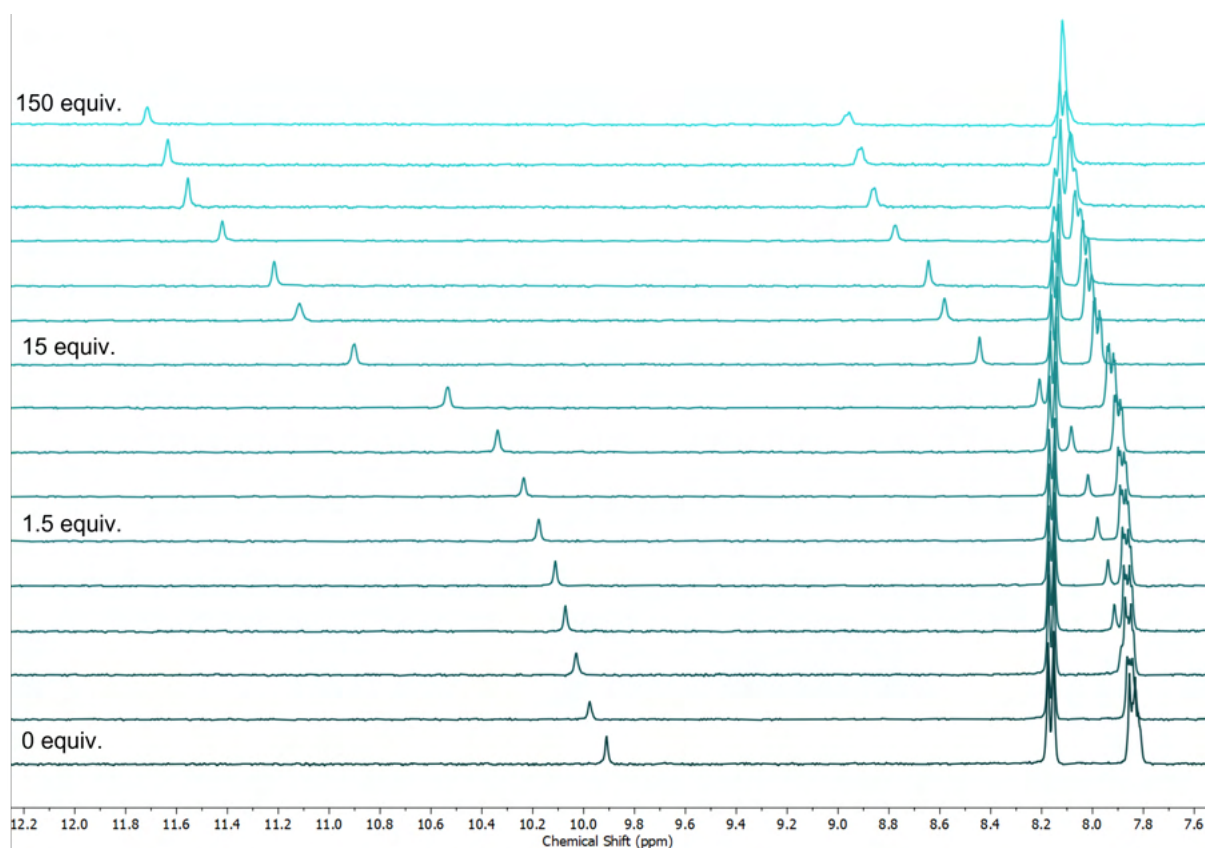
Figure S40. ^{1}H NMR titration spectra as a stack plot for **5** (2 mM) + TBACl (0–150 equiv.) in DMSO-d$_6$ /0.5% D$_2$O at 298 K.

Figure S41. Fitted binding isotherm of **5** + TBACl showing the change in chemical shift of a NH proton and 2 aromatic CH protons fitted to the 1:1 binding model (left). K_a = 38.56 M^{-1}. Residual plot showing the random error obtained from the binding isotherm fitting (right). Covariance of fit (cov$_{fit}$) = 3.08 x 10^{-3}. Link to Bindfit fitting: http://app.supramolecular.org/bindfit/view/37a72349-1087-4b8d-a0db-6a6f226d9a59.

Figure S42. ^{1}H NMR titration spectra as a stack plot for **6** (2 mM) + TBACl (0–150 equiv.) in DMSO-d_6 /0.5% D_2O at 298 K.

Figure S43. Fitted binding isotherm of **6** + TBACl showing the change in chemical shift of NH and aromatic CH protons fitted to the 1:1 binding model (left). K_a = 211.22 M^{-1}. Residual plot showing the random error obtained from the binding isotherm fitting (right). Covariance of fit (cov$_{fit}$) = 8.35 x 10^{-4}. Link to Bindfit fitting: http://app.supramolecular.org/bindfit/view/cceb5ef1-3e56-443e-af5a-d66fe42b2a26.

7. Inclusion Complex Preparation

The most energetically stable configuration of the cyclodextrins takes the form of a conical cylinder, with a slightly larger opening on the face containing the secondary hydroxyl groups.[2] The internal cavity contains multiple hydrogen atoms and glycosidic oxygen bridges, which create an apolar, hydrophobic microenvironment, whilst the multitude of hydroxyl groups situated on the exterior of the cavity creates a hydrophilic rim on either end of the cyclodextrin cylinder. The ^{1}H NMR spectrum of HP-β-CD is shown in **Figure S44** with the internal and external protons labelled. The contrasting properties of the hydrophilic outer surface and the hydrophobic inner cavity of cyclodextrins means the macrocycles possess the ability to act as molecular containers for non-polar guests of an appropriate size. This interaction is purely supramolecular in nature, driven by van der Waals forces, host:guest hydrogen bonding interactions, and the dehydration of the non-polar internal cavity by the insertion of a guest molecule (hydrophobic effect).[3] A solute can be fully or partially encapsulated by a CD host and, in solution, the free CD, free guest, and inclusion complex maintain a dynamic equilibrium. The most important consequence of this encapsulation is an increase in the aqueous solubility of the guest molecule.

Cyclodextrin inclusion complex strategies have been widely implemented to improve the aqueous solubility and bioavailability of drug molecules.[4] CDs are available on an industrial scale from a renewable natural resource and are recognised as non-toxic.[5-7] The complexation of drugs can also reduce irritation to the stomach or skin by reducing the local concentration of the molecule, mask an unpleasant odour or taste, and prevent the crystallisation of active ingredients.[8-10]
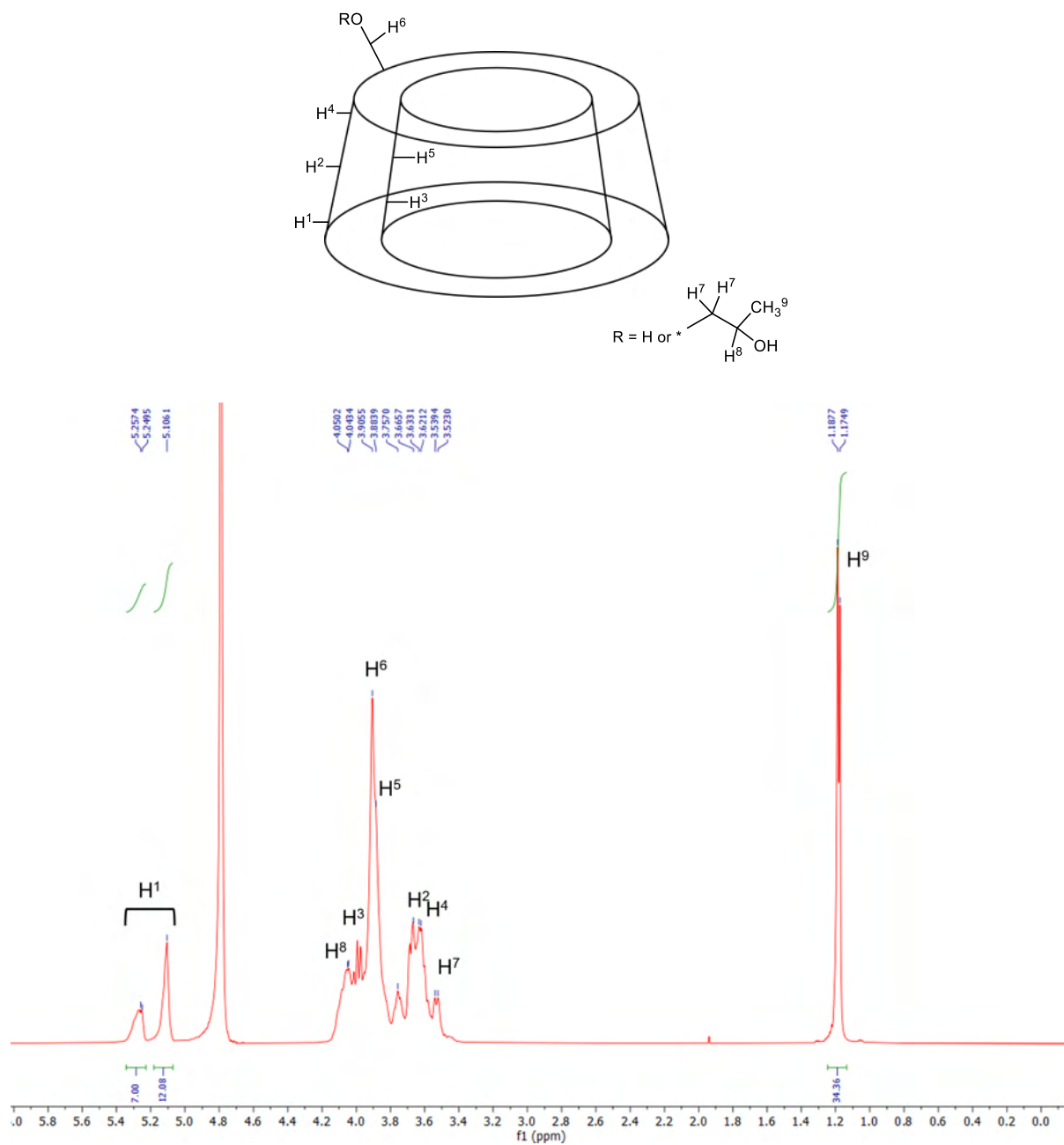
Figure S44. The ^{1}H NMR spectrum (500 MHz) for HP-β-CD in D$_2$O. The signals attributed to each proton are labelled and correspond to the diagram of HP-β-CD diagram above, adapted from the literature.[11]
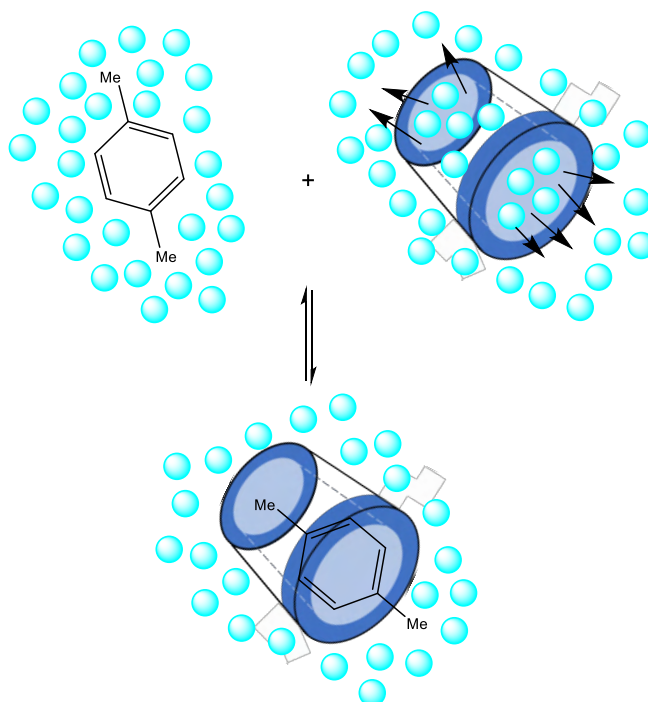
Figure S45. Schematic representation of the CD inclusion complex equilibrium adapted from the literature.[2] *p*-Xylene is the guest molecule, and the water molecules (blue spheres) are excluded from the hydrophobic cavity of the cyclodextrin host during the inclusion process.

The formation of an inclusion complex between HP-β-CD and each of the compounds **1**−**6** was attempted using three different methods, adapted from procedures employed in the literature.[12, 13] Each method involved using a 1:1 water:ethanol solvent mixture to ensure that both host and guest were partially solubilised during the process and can reorientate to form an inclusion complex. Additionally, each inclusion complex mixture was added to pure water after the completion of the inclusion process. This addition resulted in the precipitation of any uncomplexed transporter, which was filtered and removed, leaving a filtrate containing a mixture of free HP-β-CD host and the desired inclusion complex. A total of 24 inclusion complex procedures were attempted.

7.1 Method 1: Kneading

An equimolar physical mixture of HP-β-CD (138 mg, 0.01 mmol) and transporter (0.01 mmol) was combined with a mortar and pestle. A small volume (~0.5−1.0 mL) of 1:1 water:ethanol solvent mixture was added dropwise, and the components were ground together into a homogenous paste for 30 min. Additional solvent was added when required to keep the paste from drying out. Following this, the product was dried at 65 °C in a vacuum oven for 2 h to

remove residual solvent. The dry powder was transferred to a glass vial (21 mL), and a portion of Milli-q water (5 mL) was added. The resulting precipitate was filtered out, and the filtrate was collected. The solvent was removed under nitrogen before the solid residue was dried overnight *in vacuo* yielding a crystalline solid.

7.2 Method 2: Microwave Irradiation (Minimum Solvent)

An equimolar physical mixture of HP-β-CD (138 mg, 0.01 mmol) and transporter (0.01 mmol) was combined with a mortar and pestle. In the absence of solvent, the two components were ground together for 10 min to form a homogenous and amorphous solid mixture. The two components were transferred to a 10 mL Pyrex microwave vessel, and a *w/w* mass of 1:1 water:ethanol solvent mixture was added (approx. 200 mg). The mixture was sonicated to ensure that all the powder mixture was saturated by solvent. Next, the reaction vessel was subjected to microwave irradiation for 10 min using a single-mode CEM Discover® microwave synthesiser kept at 80 °C through moderation of the initial microwave power (150 W). Subsequently, the product was dried at 65 °C in a vacuum oven for 2 h to remove residual solvent. The dry powder was transferred to a glass vial (21 mL), and a portion of Milli-q water (5 mL) was added. The resultant precipitate was filtered and removed whilst the filtrate was collected. The solvent was removed under nitrogen before being dried overnight *in vacuo* to yield a crystalline solid.

7.3 Method 3: Microwave Irradiation (2.5 mL of Solvent)

This method was adapted from the procedure outlined by Noto and co-workers.[13] An equimolar physical mixture of HP-β-CD (138 mg, 0.01 mmol) and transporter (0.01 mmol) was combined with a mortar and pestle, ground together for 10 min to form a homogenous and amorphous solid mixture in the absence of solvent. The two components were transferred to a 10 mL Pyrex vessel, and a portion of 1:1 water:ethanol solvent mixture (2.5 mL) was added. The mixture was sonicated to ensure that all the powder mixture was saturated by solvent and not stuck to the walls of the vessel. Next, the reaction vessel was subjected to microwave irradiation for 25 min using a single-mode CEM Discover® microwave synthesiser kept at 80 °C through moderation of the initial microwave power (150 W). A portion of pure water (5 mL) was added to the Pyrex vessel, and the resultant precipitate was filtered and removed

whilst the filtrate was collected. The solvent was removed under nitrogen before being dried overnight *in vacuo* to yield a crystalline solid.

8. Proton NMR Spectroscopy Analysis of Inclusion Complexes

The water-soluble filtrates of all 24 inclusion attempts (Compounds **1–6**, methods 1–3) were collected and dried to leave crystalline solids. Subsequently, a small portion of each solid (10–15 mg) was dissolved in D_2O, and a ^1H NMR spectrum (400 MHz) was collected. Dissolution attempts in D_2O of several solid mixtures resulted in the precipitation of a solid, which was removed before a spectrum was obtained. The solid obtained is likely free transporter and suggests that, for these attempts, an inclusion complex did not fully form or that the compounds decomplexed from HP-β-CD as the water was removed during the last step of each method.

Crucial evidence supporting the existence of an inclusion complex is the appearance of resonance signals in the D_2O spectrum that can be attributed to the protons of the transporter compound. Compounds **1–6** exhibit very low solubility in D_2O, and the appearance of signals associated with these molecules suggests that their aqueous solubility has been enhanced. The integrations of the resonances attributed to the transporter molecule relative to the HP-β-CD signals provide an indication of how much of the transporter is present in the inclusion complex. However, the relative integrations cannot be used to calculate the exact stoichiometric ratios of transporter and HP-β-CD. Commercial HP-β-CD is prepared via the condensation of native β-CD with an excess of propylene oxide, but this does not result in the complete substitution of the hydroxyl groups.[14] Therefore, HP-β-CD typically contains a mixture of hydroxypropyl derivatives and free hydroxyl groups, and the supplier provides an average molecular weight (M.W. ~ 1380 $gmol^{-1}$). This means that integration cannot be reliably determined and used to calculate the relative stoichiometry. In addition, the proximity of some signals to the water resonances means that the integration of these protons may correspond to a number larger than the true value. Nevertheless, the appearance of large and distinct resonance peaks attributed to the transporter compound is reliable evidence for the formation of an inclusion complex.

The ^1H NMR spectra of the inclusion complex formed between **1** and HP-β-CD using method 3 in D_2O is showed in **Figure S46**, and peaks attributed to compound **1** are clearly visible. The

aromatic peaks at 8.2 and 7.7 ppm, the methyl spacer protons at 3 ppm, and adamantyl peaks at 2.2, 1.8, and 1.7 ppm can all be distinguished and have the correct proportionality when integrated. The signals for the urea protons of **1** are not present in the spectrum, which is likely a consequence of the deuterium exchange of these acidic protons with the bulk solvent. Guest molecule resonances of appreciable intensity were distinguished in the ^{1}H NMR spectra, in D$_2$O, of HP-β-CD·**1** (methods 1–3), HP-β-CD·**2** (methods 1–3), HP-β-CD·**4** (methods 1–3) and HP-β-CD·**6** (methods 1–2). Proton NMR spectra for all inclusion attempts can be viewed below.
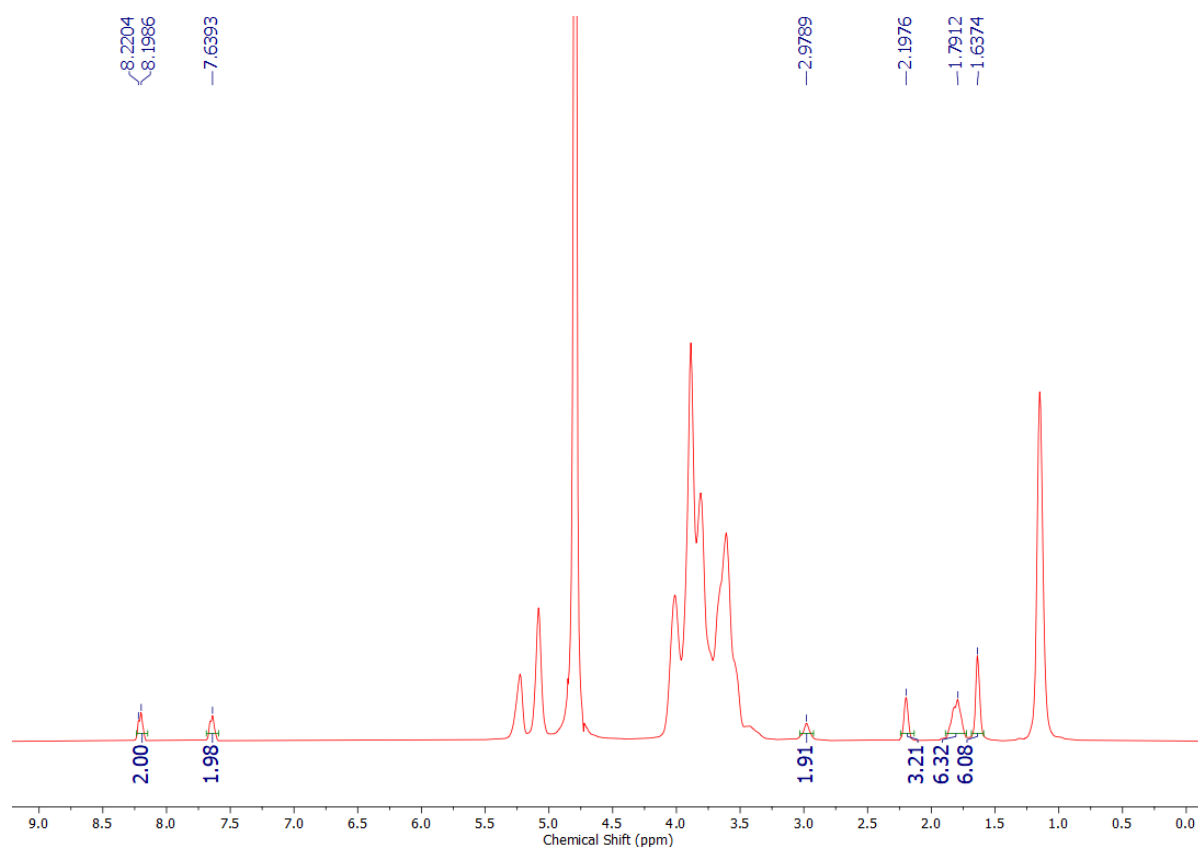
Figure S46. ^{1}H NMR (400 MHz) spectrum of HP-β-CD·**1** (method 1) in D$_2$O at 298 K.
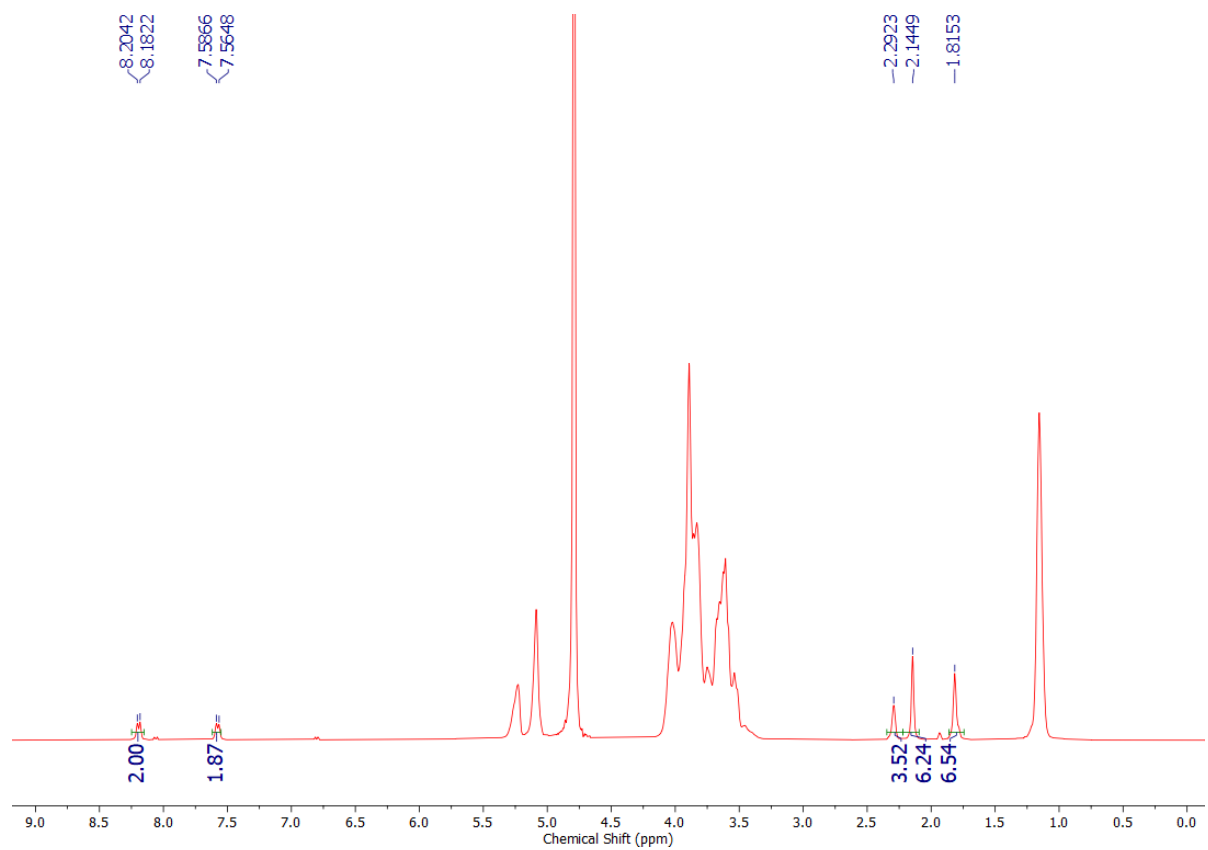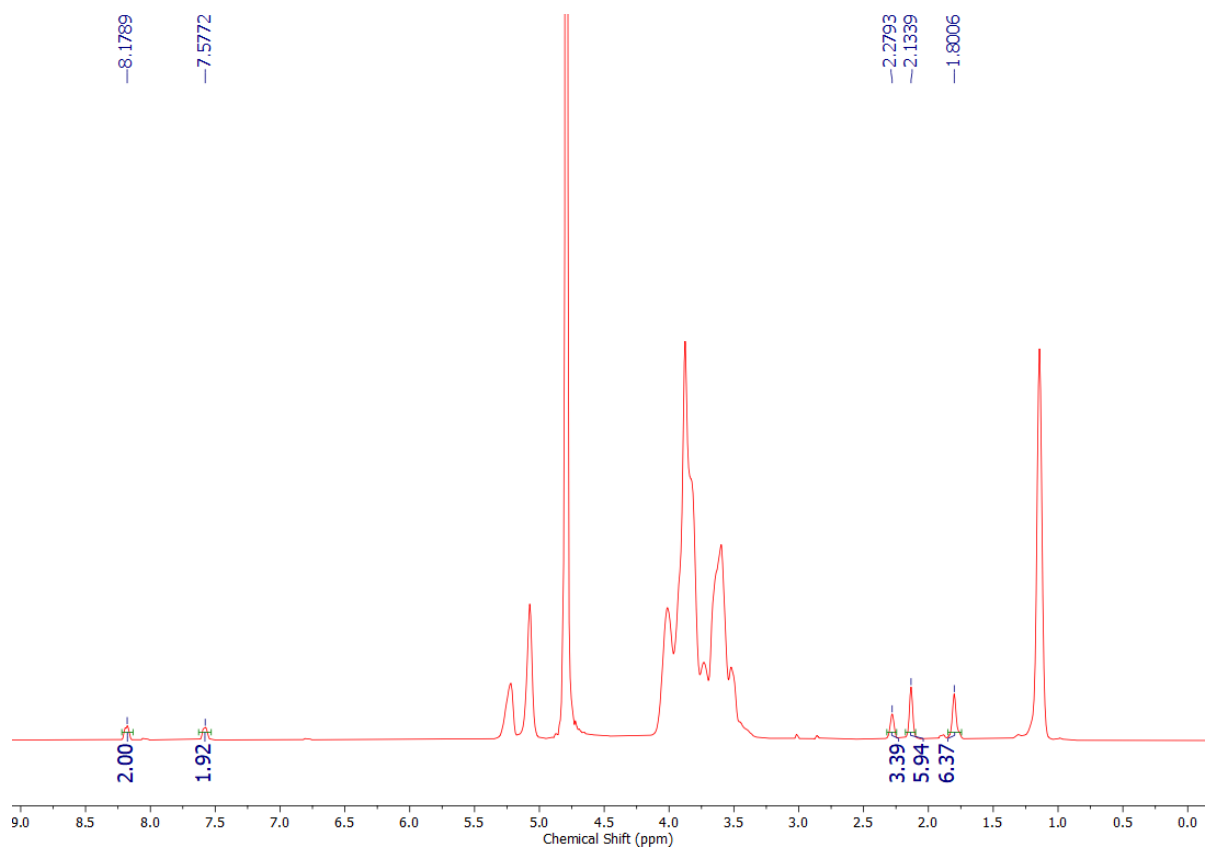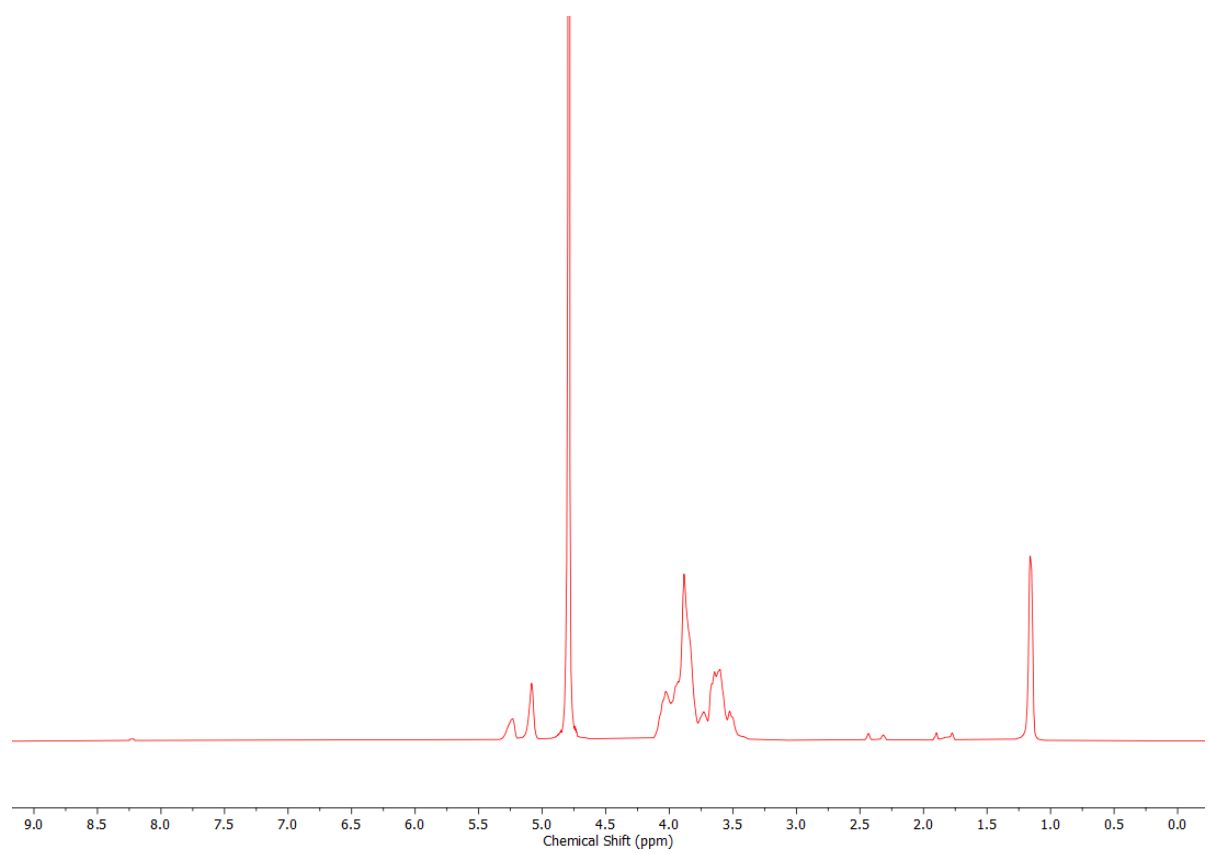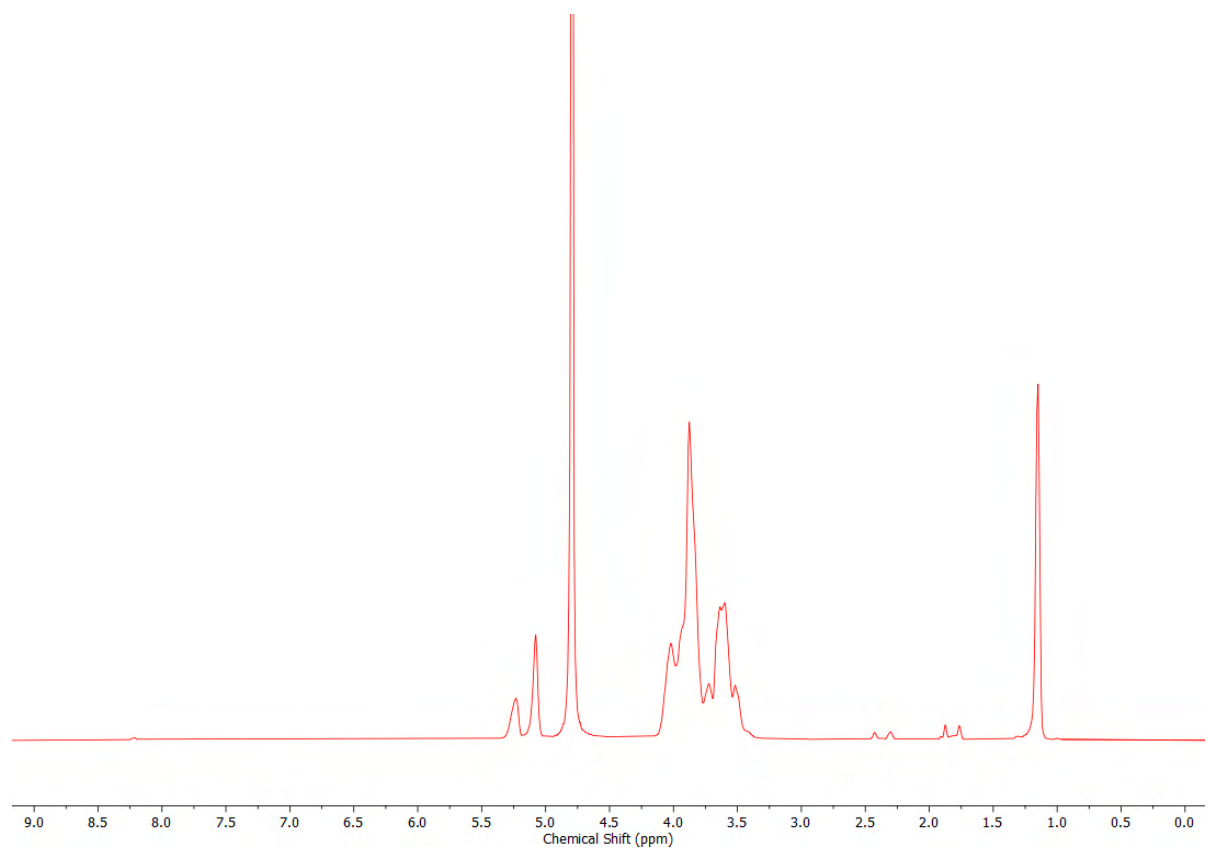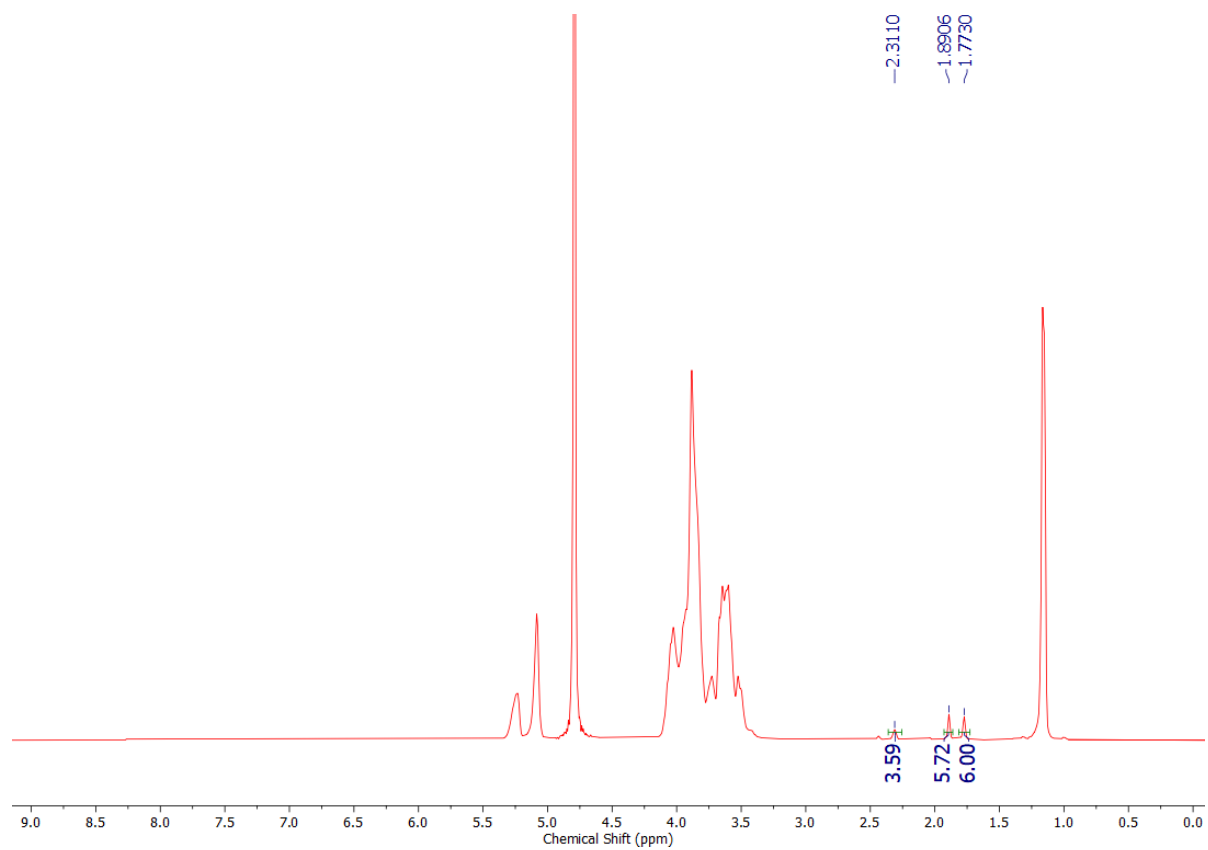
55
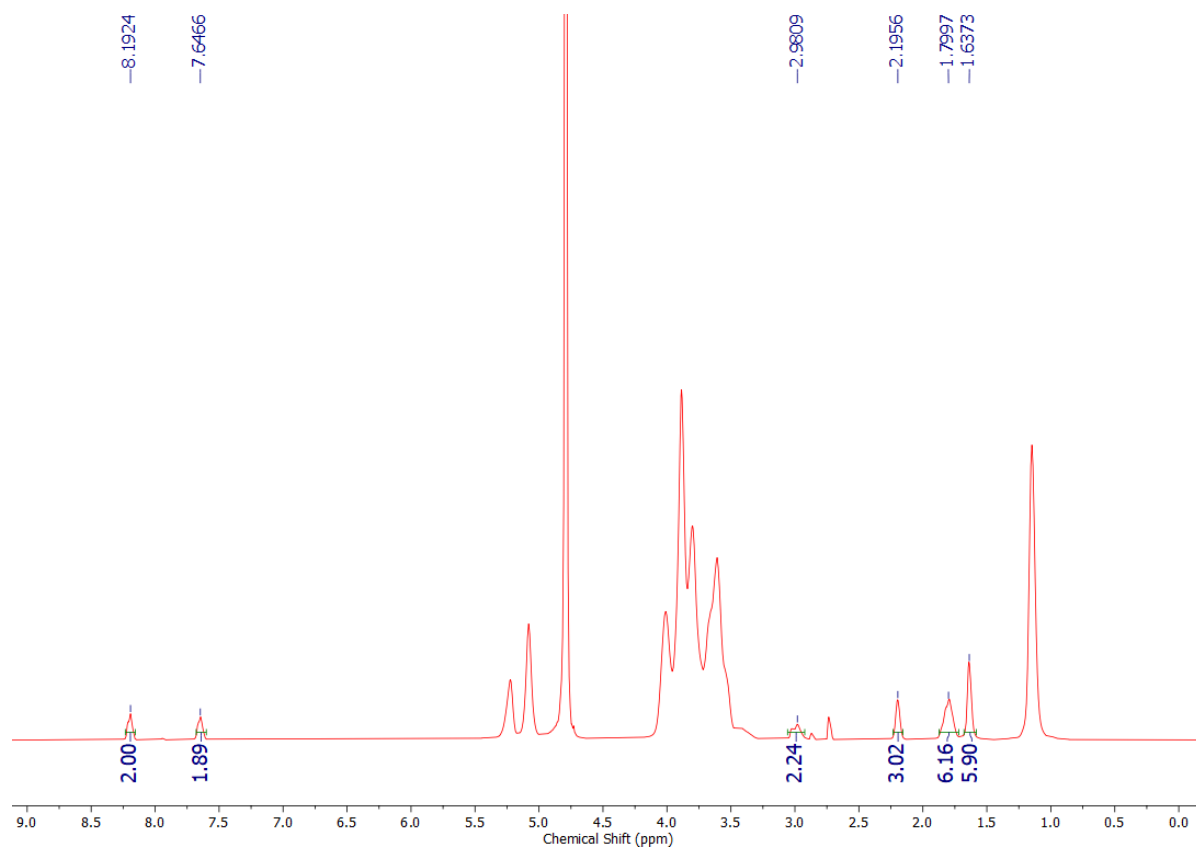
Figure S47. ^{1}H NMR (400 MHz) spectrum of HP-β-CD·**1** (method 2) in D₂O at 298 K.
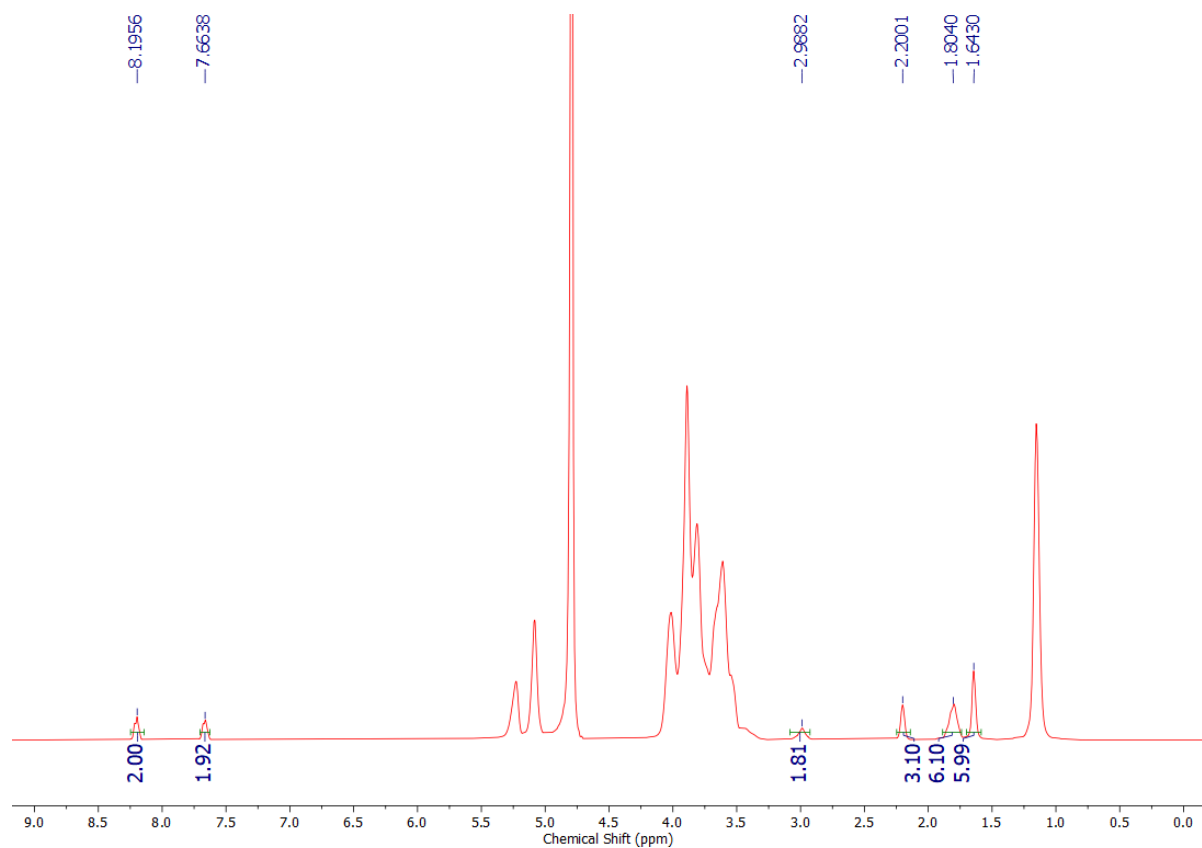
Figure S48. ^{1}H NMR (400 MHz) spectrum of HP-β-CD·**1** (method 3) in D₂O at 298 K.
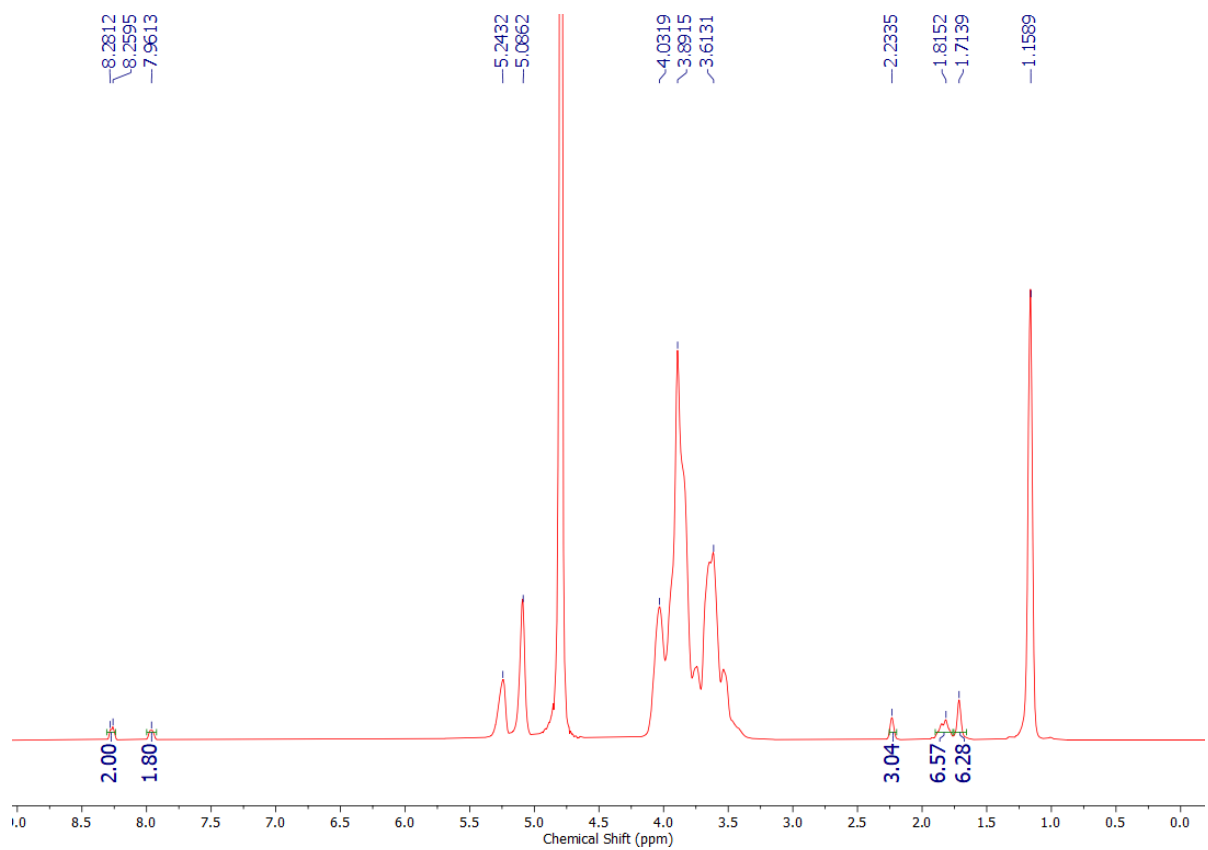
Figure S49. ^{1}H NMR (400 MHz) spectrum of HP-β-CD·**2** (method 1) in D$_2$O at 298 K.
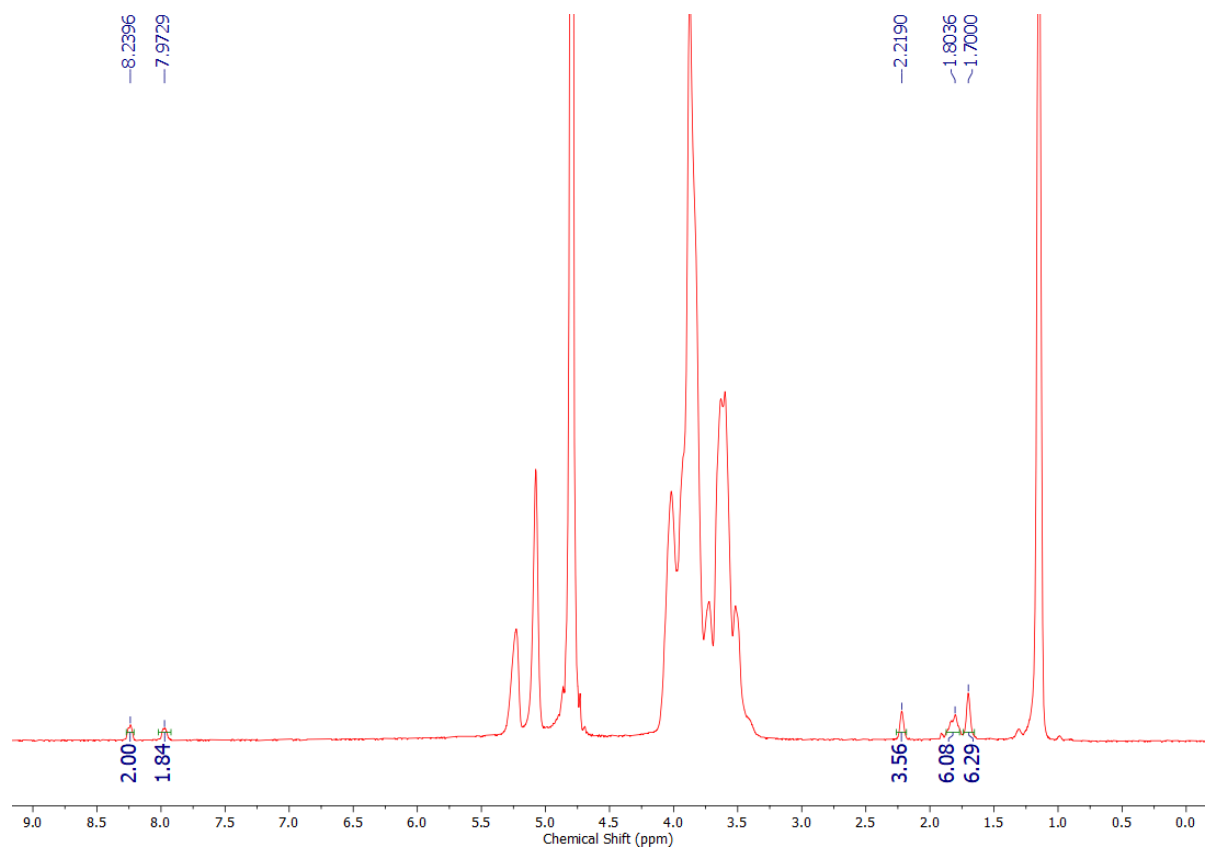
Figure S50. ^{1}H NMR (400 MHz) spectrum of HP-β-CD·**2** (method 2) in D$_2$O at 298 K.
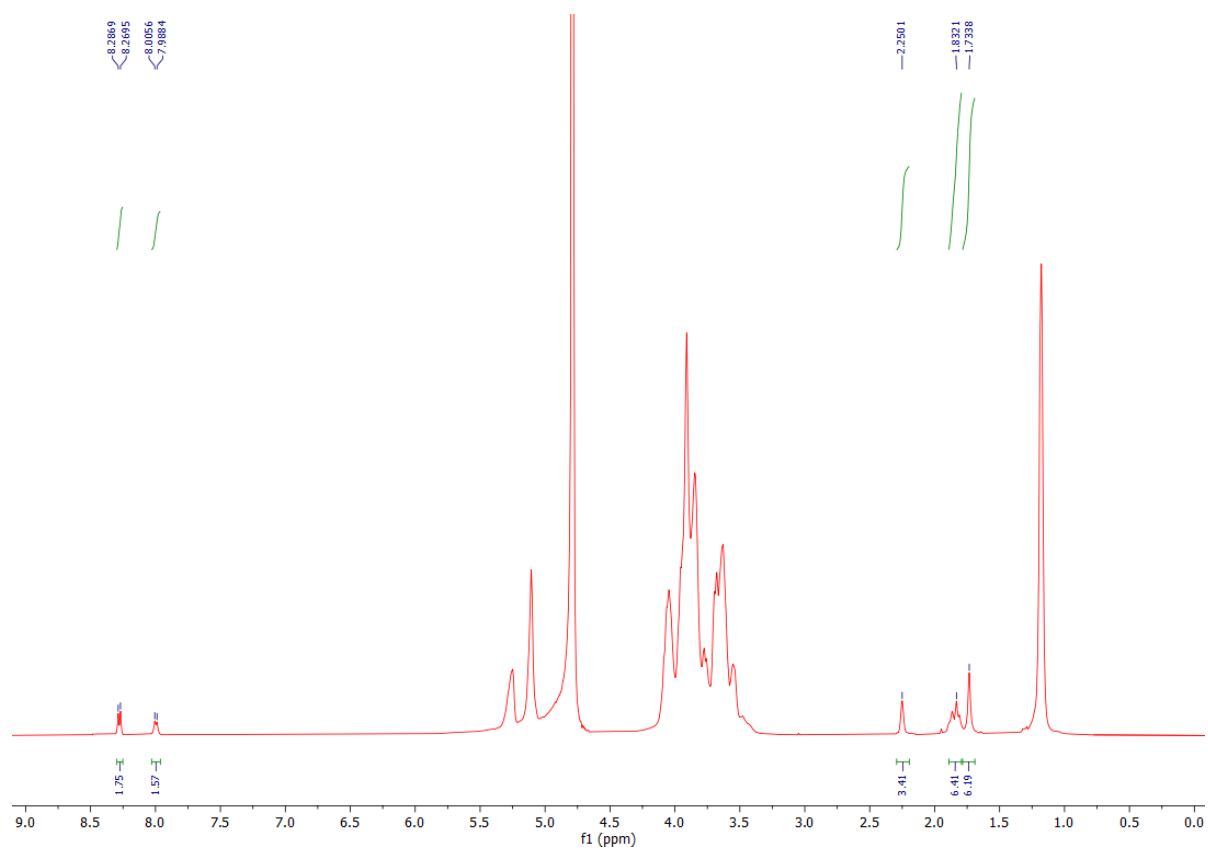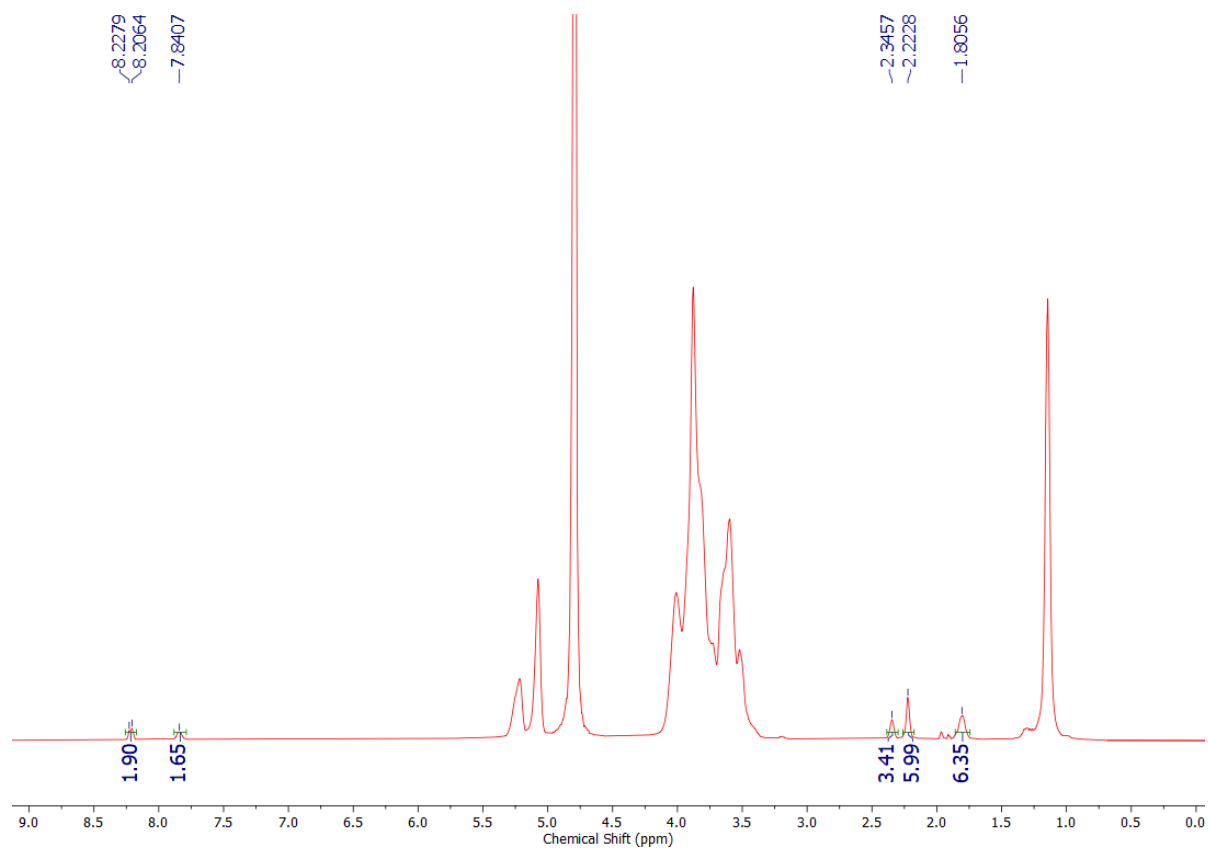
Figure S51. ^{1}H NMR (400 MHz) spectrum of HP-β-CD·**2** (method 3) in D₂O at 298 K.
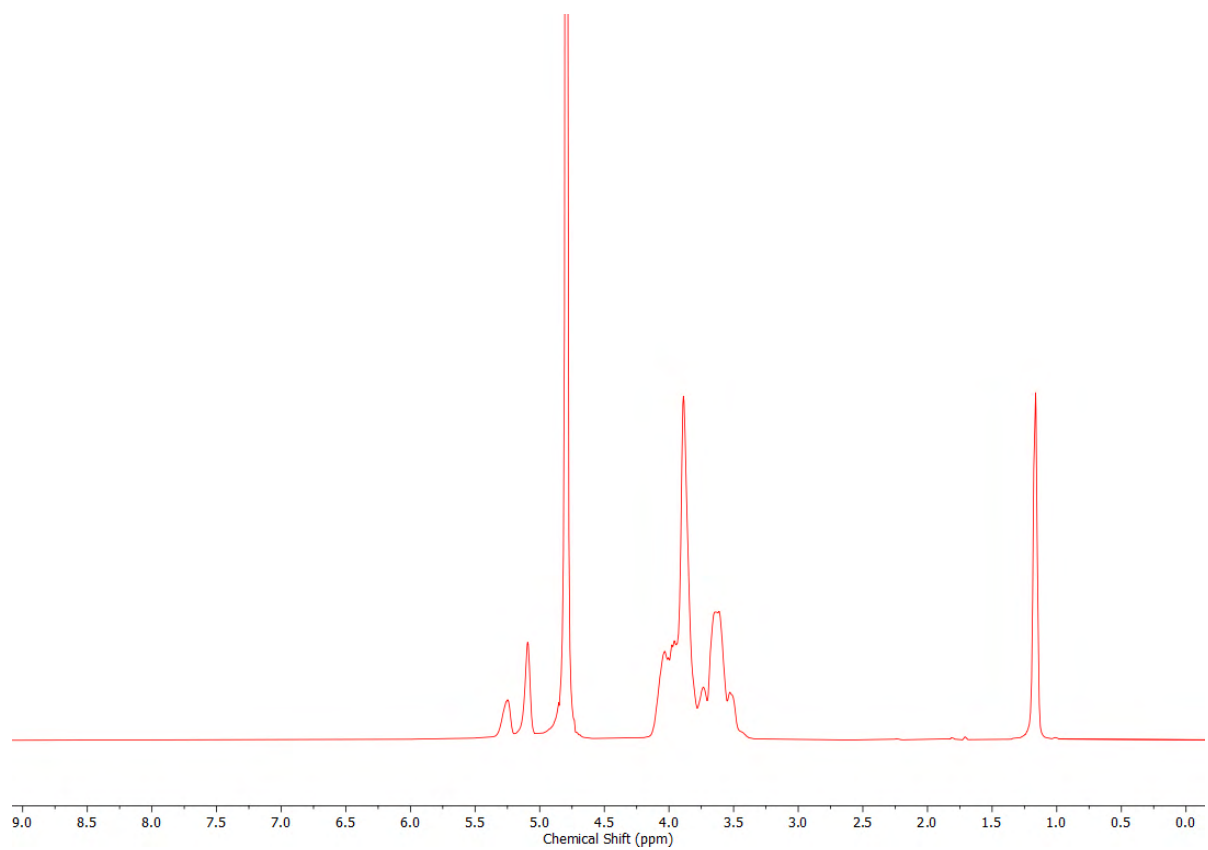
Figure S52. ¹H NMR (400 MHz) spectrum of HP-β-CD·**3** (method 1) in D₂O at 298 K.
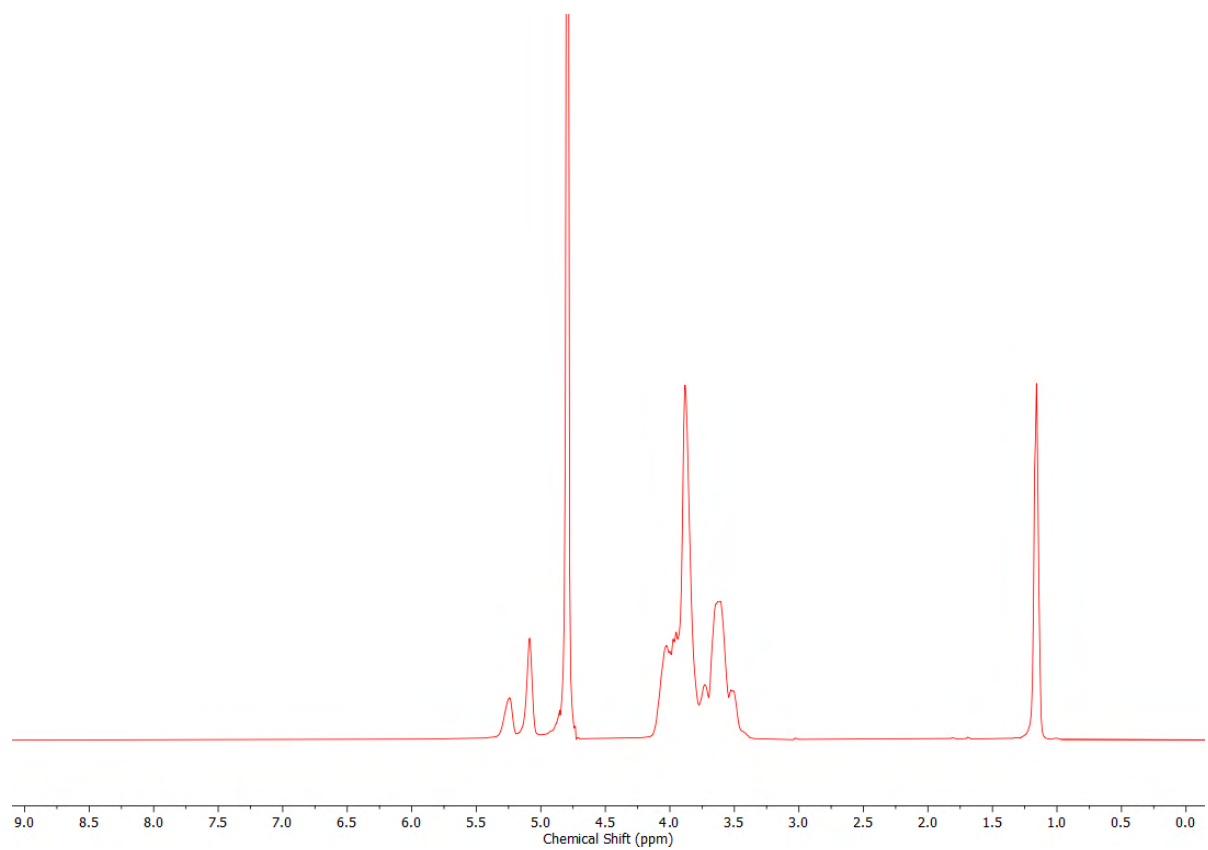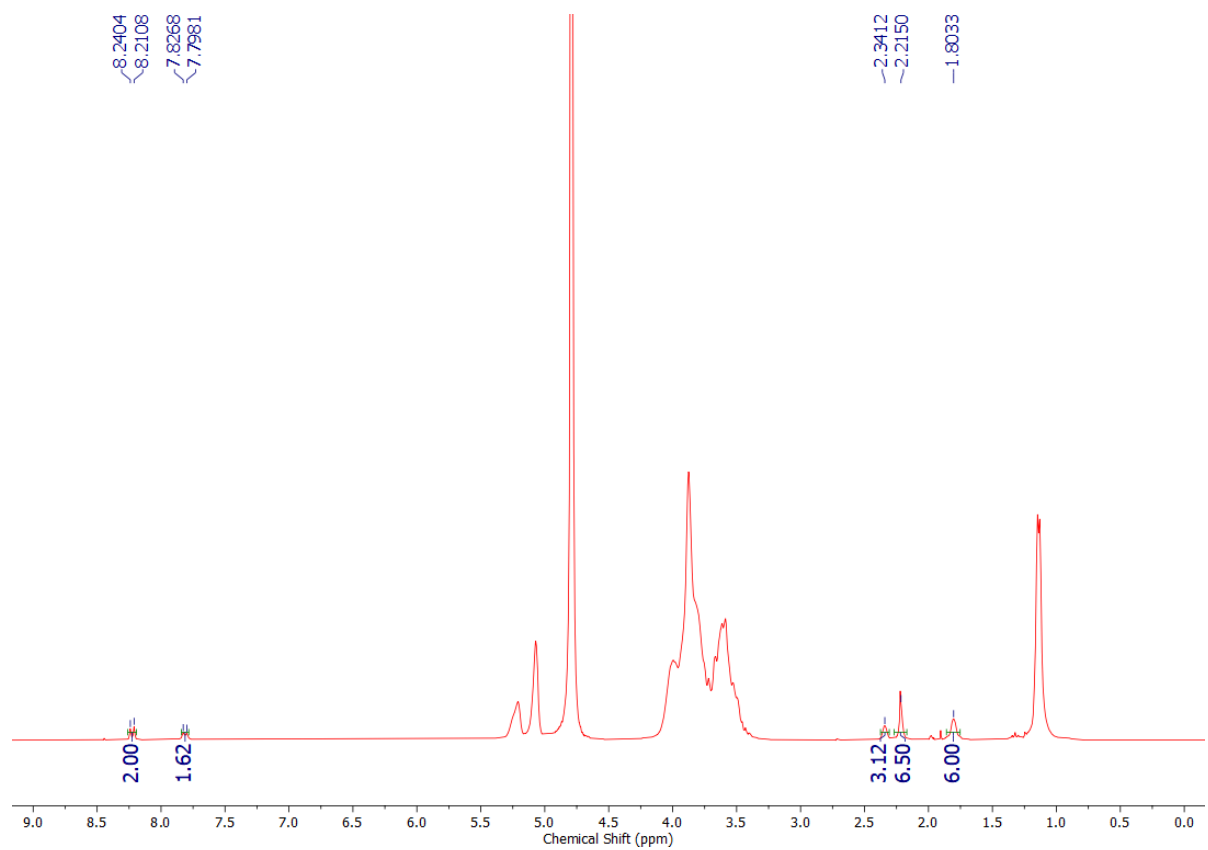
Figure S53. ^{1}H NMR (400 MHz) spectrum of HP-β-CD·**3** (method 2) in D₂O at 298 K.
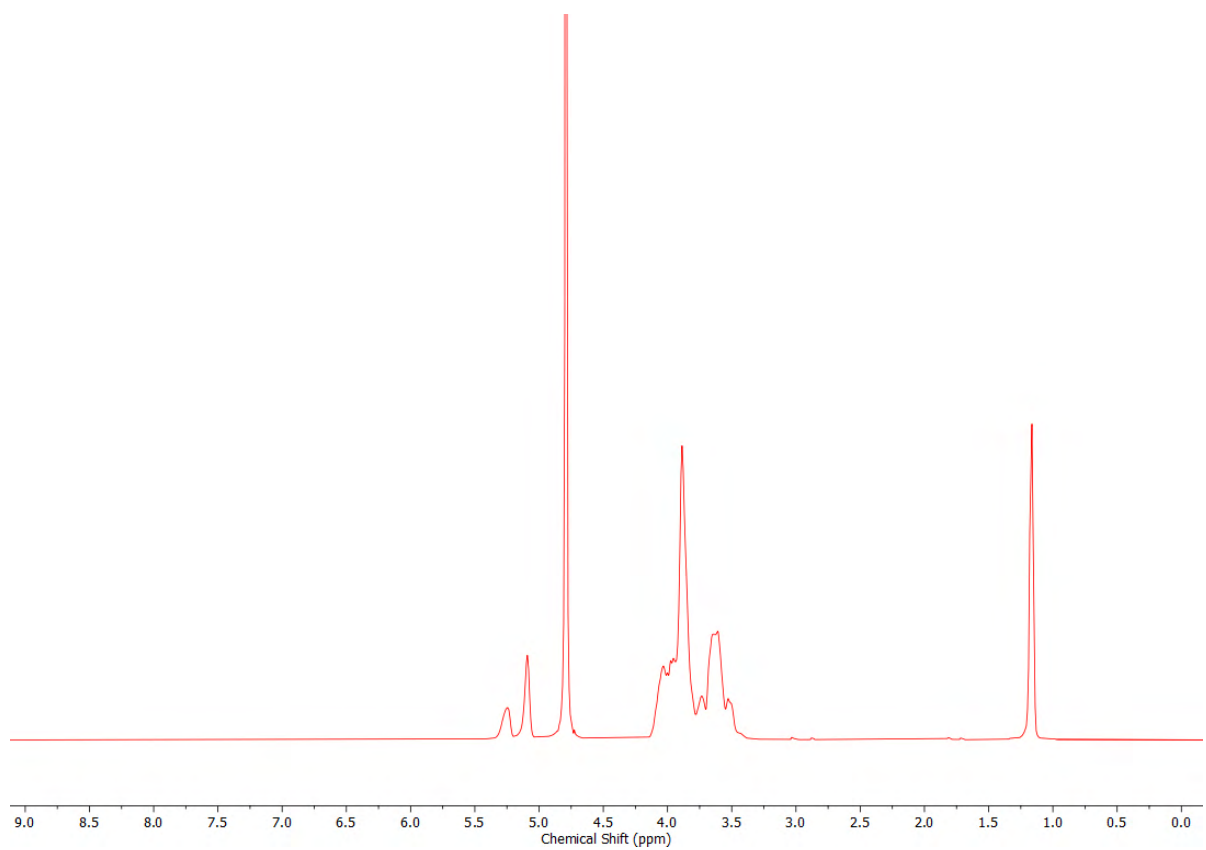
Figure S54. ^{1}H NMR (400 MHz) spectrum of HP-β-CD·**3** (method 3) in D₂O at 298 K.
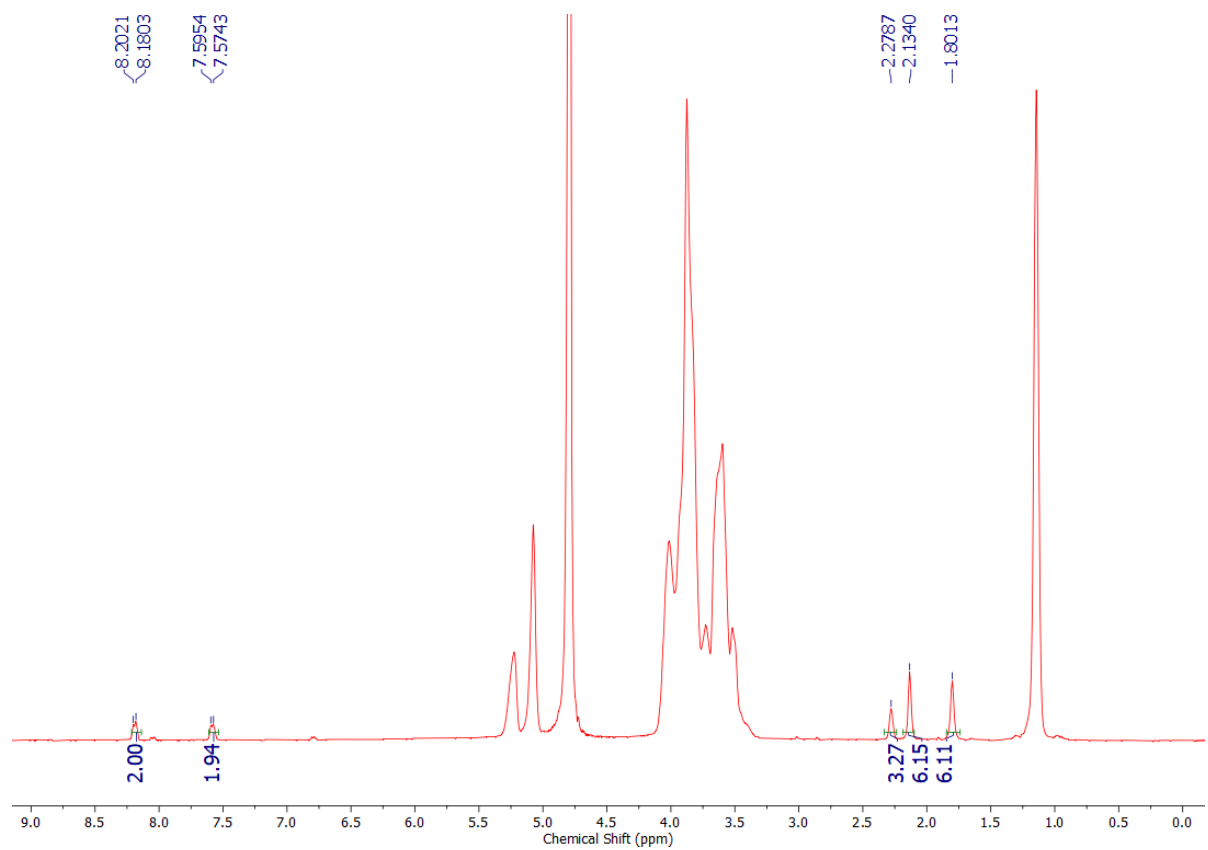
Figure S55. ^{1}H NMR (400 MHz) spectrum of HP-β-CD·**4** (method 1) in D$_2$O at 298 K.

Figure S56. ¹H NMR (400 MHz) spectrum of HP-β-CD·**4** (method 2) in D₂O at 298 K.
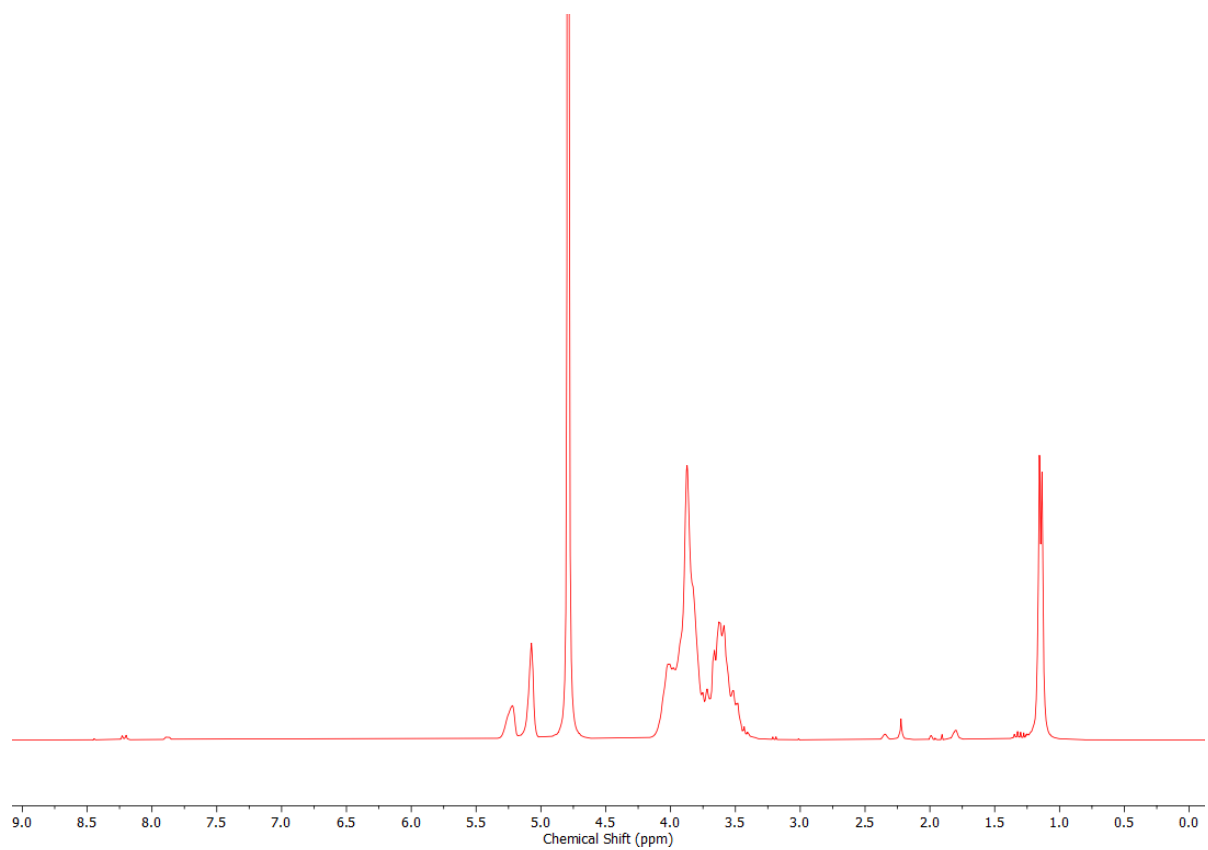
Figure S57. ^{1}H NMR (400 MHz) spectrum of HP-β-CD·**4** (method 3) in D$_2$O at 298 K.

Figure S58. ^{1}H NMR (400 MHz) spectrum of HP-β-CD·**5** (method 1) in D$_2$O at 298 K.

Figure S59. ^{1}H NMR (400 MHz) spectrum of HP-β-CD·**5** (method 2) in D₂O at 298 K.

Figure S60. ^{1}H NMR (400 MHz) spectrum of HP-β-CD·**5** (method 3) in D₂O at 298 K.

Figure S61. ^{1}H NMR (400 MHz) spectrum of HP-β-CD·**6** (method 1) in D₂O at 298 K.

Figure S62. ^{1}H NMR (400 MHz) spectrum of HP-β-CD·**6** (method 2) in D$_2$O at 298 K.

Figure S63. ^{1}H NMR (400 MHz) spectrum of HP-β-CD·**6** (method 3) in D$_2$O at 298 K.

9. UV-Vis Spectrometry

9.1 UV-Vis Calibration Spectra

UV-Vis studies in DMSO were performed to ascertain the percentage mass of transporter present in each inclusion complex. DMSO was used ahead of H_2O as the free transporters **1–6** readily dissolve in this medium, and the solvent possesses a relatively low UV wavelength cut-off.[15] The UV cut-off is the wavelength at which the solvent absorbance in a 1 cm path length equals 1 absorbance unit (A), and absorbance becomes excessive at wavelengths below this value. UV-vis spectra were initially collected at five concentrations ranging from 5–50 µM for the free compounds **1–6**. Plotting concentration against the maximum absorbance returned a linear relationship in accord with the Beer-Lambert Law. This is given in **Equation S1**:

$$A = \varepsilon cl$$

Equation S1. The Beer-Lambert Law

Where; A is absorbance, c is the concentration of the species, l is the path length in cm (for these experiments, $l = 1$ cm), and ε is the molar extinction coefficient. The gradient of the linear fit calculated for the plot of A against c can be taken as equal to ε.
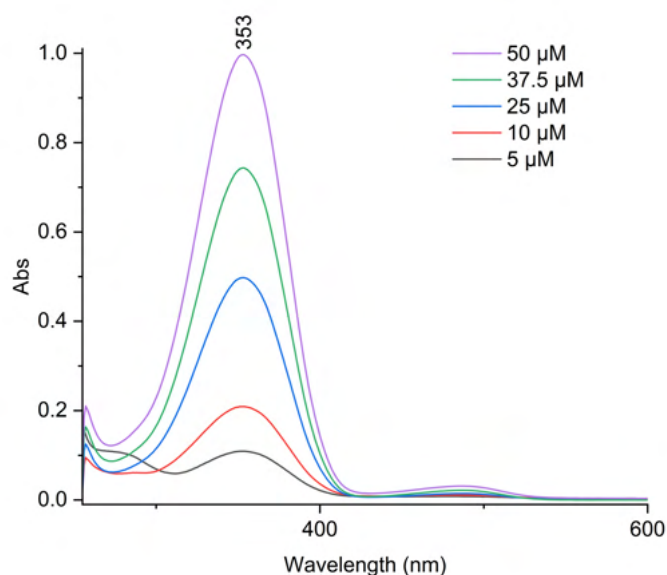

Figure S64. The UV-Vis calibration traces of **1**, for concentrations ranging from 5–50 µM. The wavelength of maximum absorbance is labelled (353 nm).

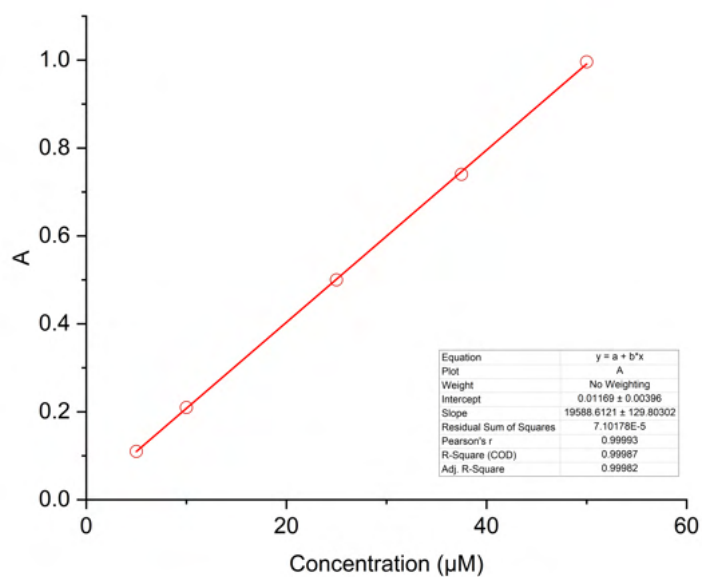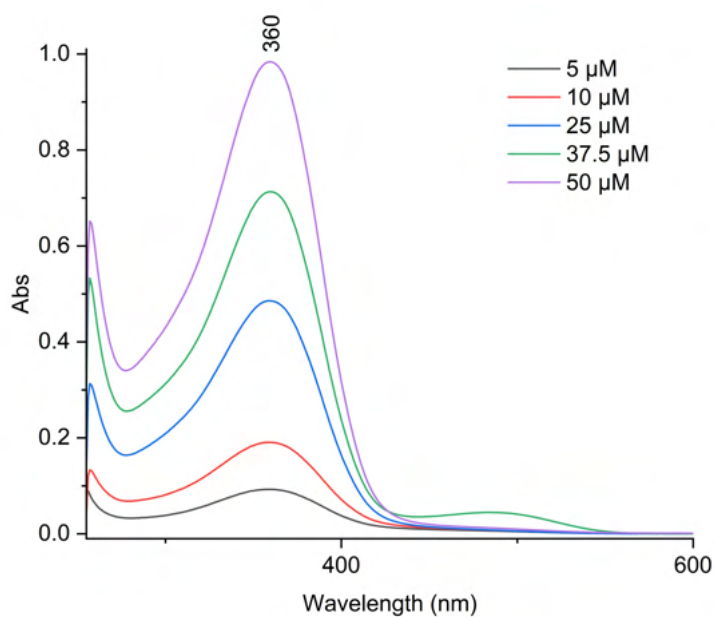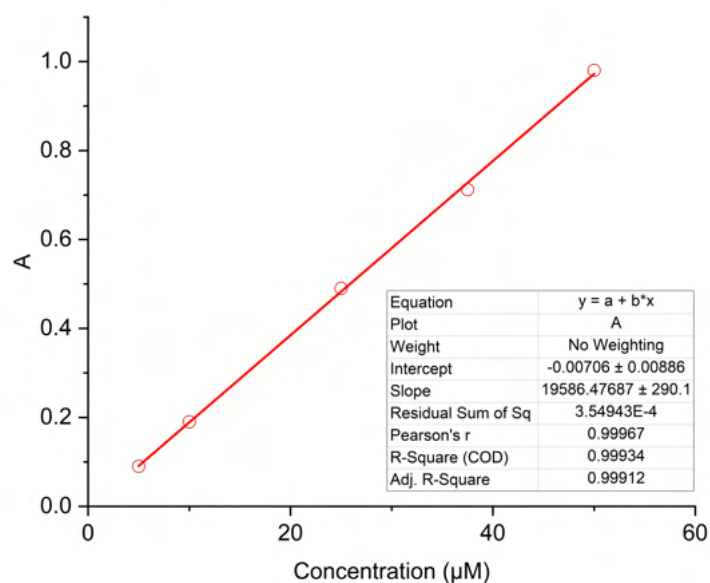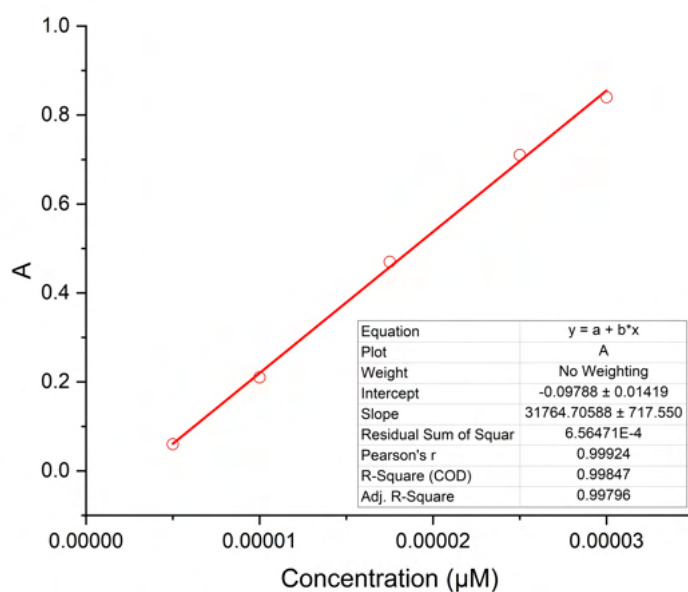| Equation	y = a + b*x
Plot	A
Weight	No Weighting
Intercept	0.01169 ± 0.00396
Slope	19588.6121 ± 129.80302
Residual Sum of Squares	7.10178E-5
Pearson's r	0.99993
R-Square (COD)	0.99987
Adj. R-Square	0.99982

Figure S65. Plot of maximum absorbance against concentration for **1**. The gradient provides a molar extinction coefficient value of $\varepsilon = 19589$ M^{-1} cm^{-1}.

Figure S66. The UV-Vis calibration traces of **2**, for concentrations ranging from 5–50 µM. The wavelength of maximum absorbance is labelled (360 nm).

Equation	y = a + b*x
Plot	A
Weight	No Weighting
Intercept	-0.00706 ± 0.00886
Slope	19586.47687 ± 290.1
Residual Sum of Sq	3.54943E-4
Pearson's r	0.99967
R-Square (COD)	0.99934
Adj. R-Square	0.99912

Figure S67. Plot of maximum absorbance against concentration for **2**. The gradient provides a molar extinction coefficient value of ε = 19586 M^{-1} cm^{-1}.
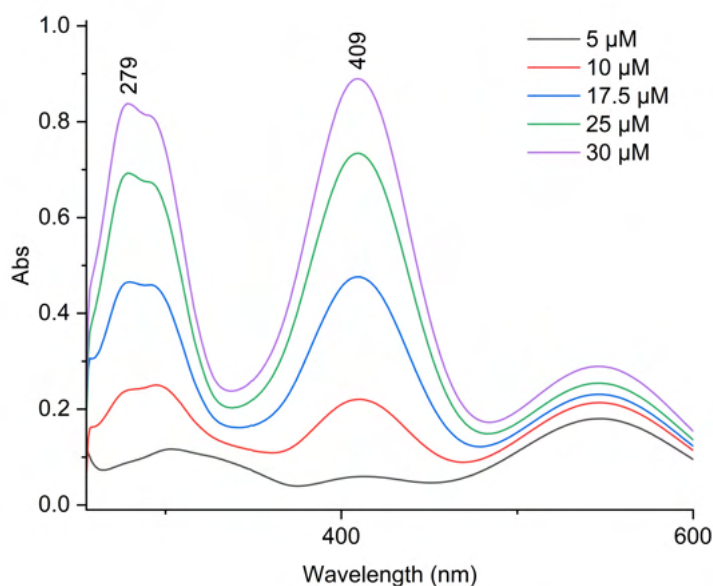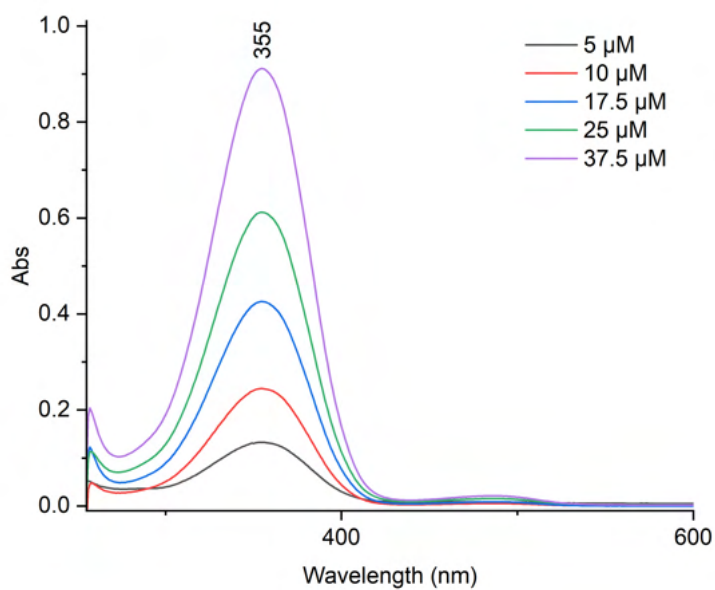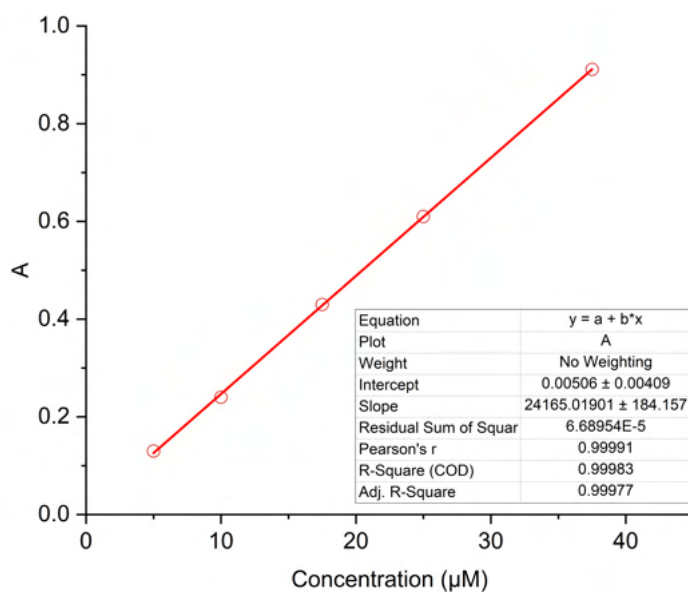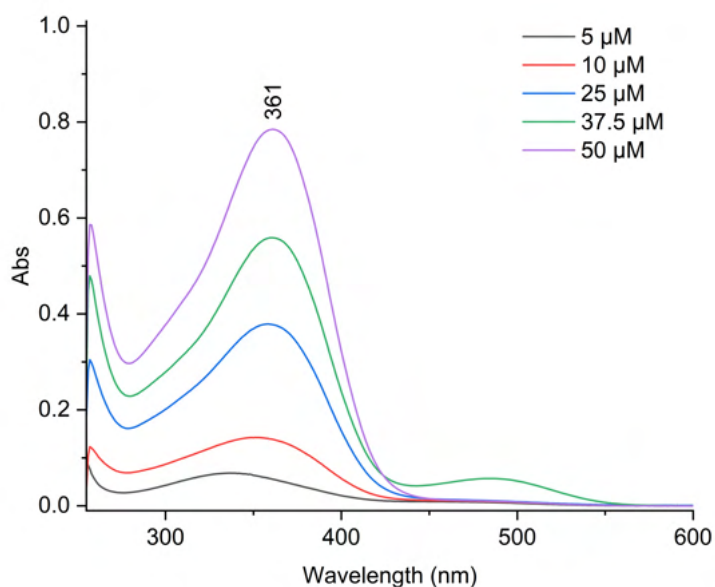

Figure S68. The UV-Vis calibration traces of **3**, for concentrations ranging from 5–30 µM. The wavelength of maximum absorbance is labelled (409 nm).

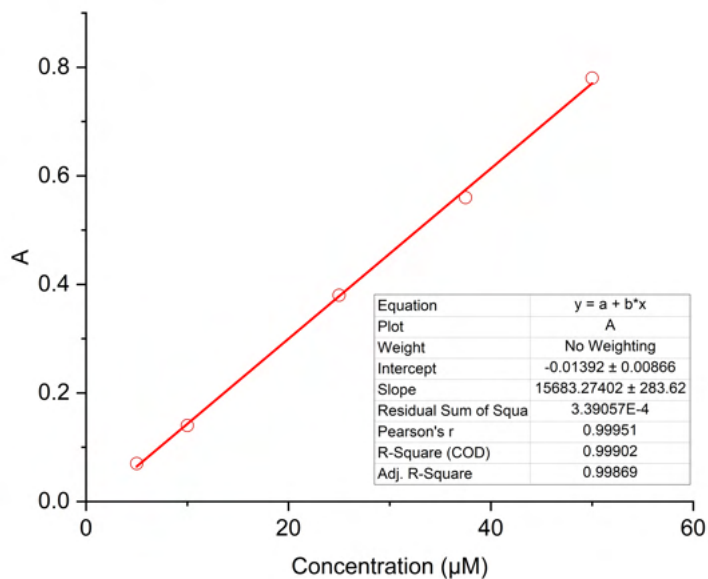| Equation	y = a + b*x
Plot	A
Weight	No Weighting
Intercept	-0.09788 ± 0.01419
Slope	31764.70588 ± 717.550
Residual Sum of Squar	6.56471E-4
Pearson's r	0.99924
R-Square (COD)	0.99847
Adj. R-Square	0.99796

Figure S69. Plot of maximum absorbance against concentration for **3**. The gradient provides a molar extinction coefficient value of $\varepsilon = 33412$ M^{-1} cm^{-1}.

The small quantities of **3** present in the inclusion complex mixtures for this compound meant that calibration quantification was not repeated in the presence of perchloric acid (explained below).

Figure S70. The UV-Vis calibration traces of **4**, for concentrations ranging from 5–37.5 μM. The wavelength of maximum absorbance is labelled (355 nm).

Equation	y = a + b*x
Plot	A
Weight	No Weighting
Intercept	0.00506 ± 0.00409
Slope	24165.01901 ± 184.157
Residual Sum of Squar	6.68954E-5
Pearson's r	0.99991
R-Square (COD)	0.99983
Adj. R-Square	0.99977

Figure S71. Plot of maximum absorbance against concentration for **4**. The gradient provides a molar extinction coefficient value of $\varepsilon = 24165$ M^{-1} cm^{-1}.

Figure S72. The UV-Vis calibration traces of **5**, for concentrations ranging from 5–50 µM. The wavelength of maximum absorbance is labelled (361 nm).

Equation	y = a + b*x
Plot	A
Weight	No Weighting
Intercept	-0.01392 ± 0.00866
Slope	15683.27402 ± 283.62
Residual Sum of Squa	3.39057E-4
Pearson's r	0.99951
R-Square (COD)	0.99902
Adj. R-Square	0.99869

Figure S73. Plot of maximum absorbance against concentration for **5**. The gradient provides a molar extinction coefficient value of ε = 15683 M^{-1} cm^{-1}.

An interesting property of squaramide receptors **3** and **6** was encountered during the serial dilution and initial UV-Vis calibration experiments of these compounds. Both compounds

were a dark yellow colour at a concentration of 200 μM in DMSO. This colour faded as the concentration decreased until around 50 μM, where a new hue began to appear. At a concentration of 5 μM, the solutions were a vibrant purple in colour (**Figure S74**). The photophysical behaviour underpinning this colour change became apparent when examining the UV-Vis calibration spectra for **6**. The absorbance peaks at wavelengths 283, 293, and 408 nm decreased linearly with concentration, whereas the peak at 539 nm decreased in a non-linear fashion. In the UV-Vis spectrum for **6** at 5 μM, the peak at 539 nm was the maximum absorbance of the system.

A similar phenomenon was reported by Rostami *et al.* during their investigations into *N,N'*-diarylsquaramides also containing a *p*-nitrophenyl derivative.[16] Due to the high polarity of DMSO, deprotonation of one of the squaramide N−H groups occurs at low concentrations without the addition of a base. Whereas at high concentrations, intermolecular hydrogen bonding between the N−H groups and the dicarbonyl moieties of other squaramide molecules limited the level of deprotonation. Dilution caused the molecules to be more dispersed in solution and reduced the self-association of the molecules. Less intermolecular hydrogen bonds cause deprotonation to occur more regularly, resulting in the observed colour change from yellow to purple. To circumvent possible deprotonation, a small aliquot of perchloric acid (0.01 M) was added to the solutions **6** used in UV-Vis experiments. Perchloric acid does not interfere with the UV-Vis trace and ensures the compounds do not deprotonate. The amount of transporter present in the inclusion complex mixtures of **3** did not justify the repetition of experiments in the presence of perchloric acid.
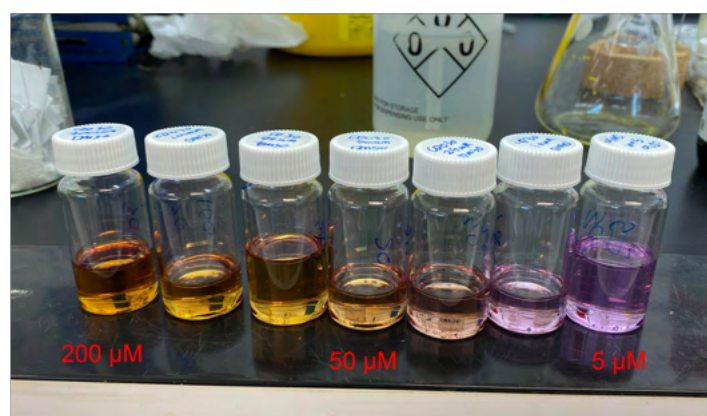
 Figure S74. The colour change from orange to purple occurred during the serial dilution of compound **6** due to the deprotonation of the receptor at low concentrations.[16] The problem was circumvented with the addition of an aliquot of perchloric acid (0.01 M).
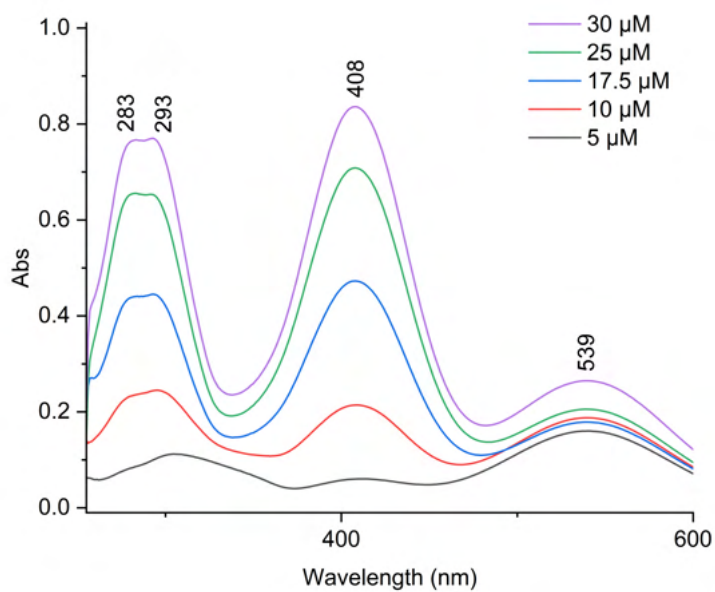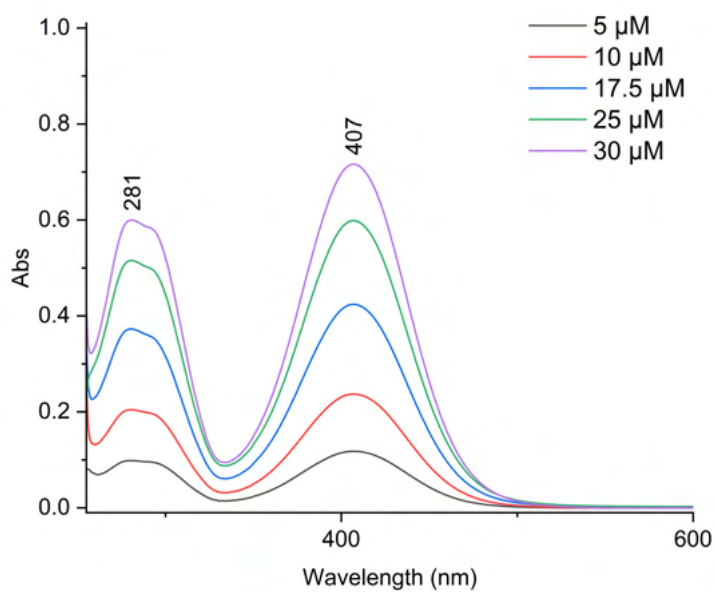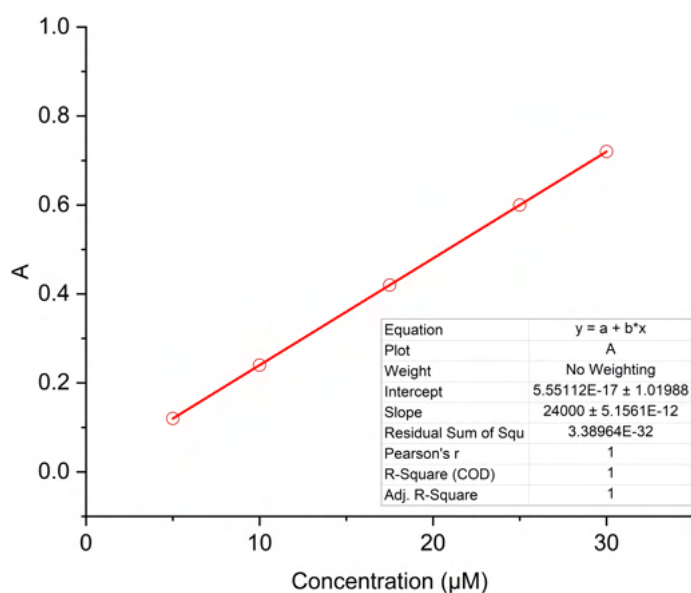

Figure S75. The UV-Vis calibration traces of **6**, for concentrations ranging from 5–30 μM. The wavelength of maximum absorbance is labelled (408 nm). These traces were collected in the absence of perchloric acid.

Figure S76. The UV-Vis calibration traces of **6**, for concentrations ranging from 5–30 µM. The wavelength of maximum absorbance is labelled (407 nm). These traces were collected in the presence of perchloric acid.

Equation	y = a + b*x
Plot	A
Weight	No Weighting
Intercept	5.55112E-17 ± 1.01988
Slope	24000 ± 5.1561E-12
Residual Sum of Squ	3.38964E-32
Pearson's r	1
R-Square (COD)	1
Adj. R-Square	1

Figure S77. Plot of maximum absorbance against concentration for **6**. The gradient provides a molar extinction coefficient value of $\varepsilon = 24000\ M^{-1}\ cm^{-1}$.

9.2 UV-Vis Quantification of Transporter Mass Percentage

HP-β-CD is not active in the UV-Vis region, and the UV-Vis spectrum of HP-β-CD contains no peaks or artefacts (**Figure S96**). Therefore, any peaks in the UV-Vis spectrum of an inclusion complex mixture were attributed solely to the transporter molecule. Spectra were collected for each of the inclusion complex mixtures (**1**−**6**, methods 1−3). A mass for each inclusion complex was recorded, and the mixtures were dissolved in 10 mL of DMSO. The maximum absorbance recorded from these spectra and the ε calculated from the calibration fit for each transporter were input into a rearranged Beer-Lambert Law equation to calculate the concentration of transporter present in each experimental solution. This concentration value was then applied to calculate the mass of the transporter present in the experimental solution and, hence, the mass percentage of transporter present in each inclusion complex mixture compared to the mass percentage of HP-β-CD was found.

The calculations used to quantify the mass percentage of transporter present in the inclusion complex mixture of HP-β-CD and **1** from method 3 are detailed below as an example. Initially, HP-β-CD·**1** (3.77 mg, method 3) was dissolved in DMSO (10 mL), and a UV-Vis trace was collected. This spectrum's maximum absorbance was above $A = 1$, so the solution was diluted by half, and a second spectrum was collected (**Figure S80**). Absorbance readings above $A = 1$ are inaccurate because of the logarithmic relationship between absorption and transmittance. At $A = 1$, only 10% of the available spectrometer light reaches the receiver as the sample absorbs the rest, and absorbance values rise rapidly over the remaining 10%. A lack of light reaching the receiver means that transmittance and, thus, absorbance values become less precise. Therefore, concentrations that give absorbance measurements between a range of $A = 0.1$−0.8 are optimal to ensure accuracy.

The maximum absorbance of the UV-Vis spectrum displayed in **Figure S80** is $A_{max} = 0.777$. The gradient of the calibration fit of **1** shown in **Figure S65** provided a value for the molar extinction coefficient of $\varepsilon = 19588.6$ M^{-1} cm^{-1} (the gradient is equal to $\varepsilon \times l$, and $l = 1$ cm). A 1 cm cuvette was also used for the UV-Vis experiments on the inclusion complex mixtures. To find the concentration of transporter, the Beer-Lambert law was rearranged to give **Equation 2** as follows:

$$c = \frac{A}{\varepsilon l} = \frac{0.77649}{(19588.6 \ M^{-1}cm^{-1}) \times (1 \ cm)} = 39.64 \ \mu M$$

Equation 2. The rearranged Beer-Lambert Law with values input for compound **1** calculations.

For the example of **1**, the concentration value was doubled, accounting for the 50% dilution, to provide a transporter concentration in the original inclusion mixture sample of 79.28 μM in DMSO (10 mL). The concentration value was be used to find the mass of transporter present by combining the equations below:

$$n = \frac{m}{M} = cv$$

Equation 3. The combined mass molarity and molar concentration equations.

Where; n is the number of moles (mol), m is the mass of the compound (g), M is the molar mass of the compound (gmol^{-1}), c is the concentration (molL^{-1}), and v is volume (L). The molar mass of **1** is 329 gmol^{-1}. This equation was rearranged to **Equation 4**, and the values input, to give the mass of transporter:

$$m = cvM = (79.28 \times 10^{-6} \ mol \ L^{-1}) \times (0.01 \ L) \times (329 \ g \ mol^{-1}) = 0.261 \ \text{mg}$$

Equation 4. The rearranged molarity equations with values input for compound **1** calculations.

The total mass of the inclusion complex mixture dissolved in DMSO was noted prior to obtaining the UV-Vis spectrum. Therefore, the mass percentage of the transporter was calculated using:

$$mass \ \% = \frac{m_{transporter}}{m_{total}} = \frac{0.261 \ g}{3.77 \ g} = 6.92\%$$

Equation 5. The mass percentage of transporter present with values input for compound **1** calculations.

The mass percentage appeared to suggest only that a small amount of transporter is present in the mixture; however, the difference in the molar mass of **1** and HP-β-CD must be considered. The molar mass of **1** is 329 gmol⁻¹ and the average molar mass of HP-β-CD provided by the supplier, based on the estimated number of substitutions of free hydroxyl groups, is 1380 gmol⁻¹. This means a 1:1 stoichiometric mixture of the two components would provide an estimated mass percentage of **1** of 19.3%. The stoichiometry of HP-β-CD·**1** (method 3) was evaluated using the average molar mass of HP-β-CD as follows:

$$\frac{n_{HP-\beta-CD}}{n_{401}} = \frac{(\frac{m}{M})_{HP-\beta-CD}}{(\frac{m}{M})_{401}} = \frac{\frac{(3.77-0.261)g}{(1380\ g\ mol^{-1})}}{\frac{(0.261\ g)}{(329\ g\ mol^{-1})}} = \frac{(2.54\times10^{-3}\ mol)}{(7.9\times10^{-4}\ mol)} = 3.21$$

Equation 6. The stoichiometric ratio of HP-β-CD:transporter present in the inclusion complex mixtures with values input for compound **1** calculations.

Therefore, there is approximately a 3:1 molar ratio of HP-β-CD to **1** present in the inclusion complex mixture of HP-β-CD·**1** (method 3). Calculations for the other compounds and inclusion methods are detailed below, and the results for each method are displayed for comparison in **Table S10**. In general, method 3 provided the highest level of transporter inclusion. Microwave irradiation has appeared as a reliable and effective method for the formulation of inclusion complexes.[17, 18] Method 1 (kneading) resulted in the lowest amount of guest inclusion, which is in agreement with other comparisons of inclusion methods reported in the literature.[19, 20]

Table S10. The mass percentage of transporter present in the inclusion complex mixtures formed between HP-β-CD and compounds **1**−**6** via methods 1−3.

Compound	Inclusion Method 1	Inclusion Method 2	Inclusion Method 3
1	3.05%	5.34%	6.92%
2	4.17%	3.96%	6.46%
3	− [a]	− [a]	− [a]
4	2.94%	4.83%	6.05%
5	1.82%	4.72%	0.92%

6	5.51% [b]	6.84% [b]	1.83% [b]

[a] Maximum absorbance peak in the UV-Vis spectrum is not large enough to quantify the mass percentage. [b] Calculated in the presence of 0.01 M of perchloric acid.

Inclusion complex mixtures containing more than 5% of **5** were not formed successfully, which seems likely to result from steric effects. This molecule lacks a methyl spacer to separate the hydrogen bond donor from the adamantyl group. The proximity of the adamantane to the bulky thiourea sulfur atom may sterically inhibit the approach of HP-β-CD and the inclusion of this part of the molecule inside the macrocycle. Inclusion complexes with compound **3** did not form whatsoever, and the process seems to be impacted by the limited solubility of the compound in ethanol. It appears that the inclusion process is more effective when both components are in the solution phase, and the limited solubility of compound **3** had already been encountered during Cl⁻ transport experiments. Compound **6** lacks a methyl spacer; however, it possesses a higher intrinsic solubility than **3** in organic solvents. This was evidenced during the synthesis of these compounds, where **6** did not crash out of the methanolic solvent, and was also reflected in the inclusion attempts, where a complex was successfully formed between **6** and HP-β-CD.
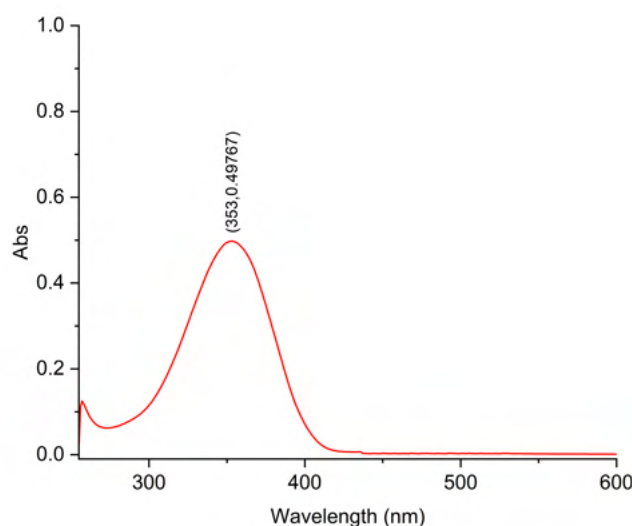
Figure S78. The UV-Vis spectrum of HP-β-CD·**1** (method 1, 4.11 mg) in DMSO (10 mL).

A_{max} =0.49767, ε = 19588.6 M^{-1} cm^{-1}

c = 25.41 µM

Solution was diluted by 1.5 so true concentration = 38.12 µM

m = (38.12 × 10^{-6}) × 0.01 × 329 = 0.125 mg

mass % = 3.05%
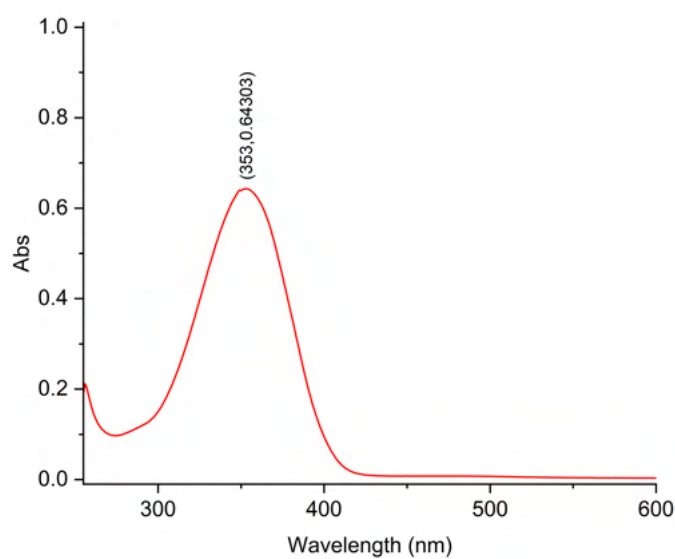
Figure S79. The UV-Vis spectrum of HP-β-CD·**1** (method 2, 4.04 mg) in DMSO (10 mL).

A_{max} = 0.64303, ε = 19588.6 M^{-1} cm^{-1}

c = 32.83 µM

Solution was diluted by 2 so true concentration = 65.65 µM

m = (65.65 × 10^{-6}) × 0.01 × 329 = 0.216 mg

mass % = 5.34%
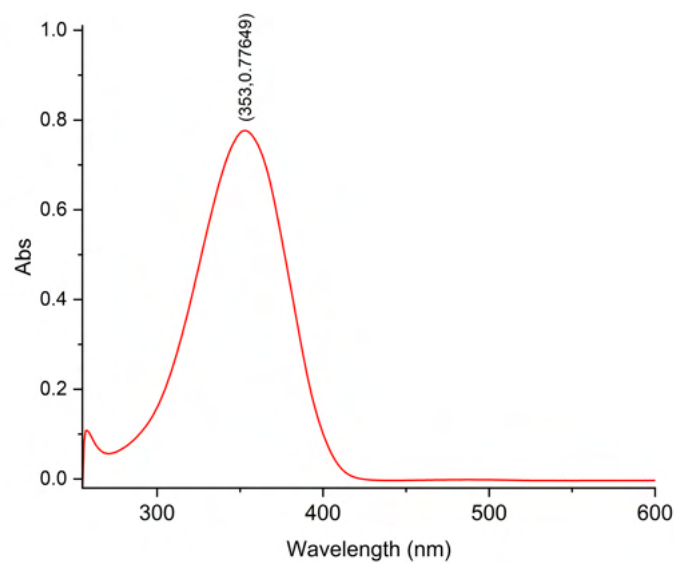
Figure S80. The UV-Vis spectrum of HP-β-CD·**1** (method 3, 3.77 mg) in DMSO (10 mL).

A_{max} = 0.77649, ε = 19588.6 M^{-1} cm^{-1}

c = 39.64 μM

Solution was diluted by 2 so true concentration = 79.28 μM

m = (79.28 × 10^{-6}) × 0.01 × 329 = 0.261 mg

mass % = 6.92%
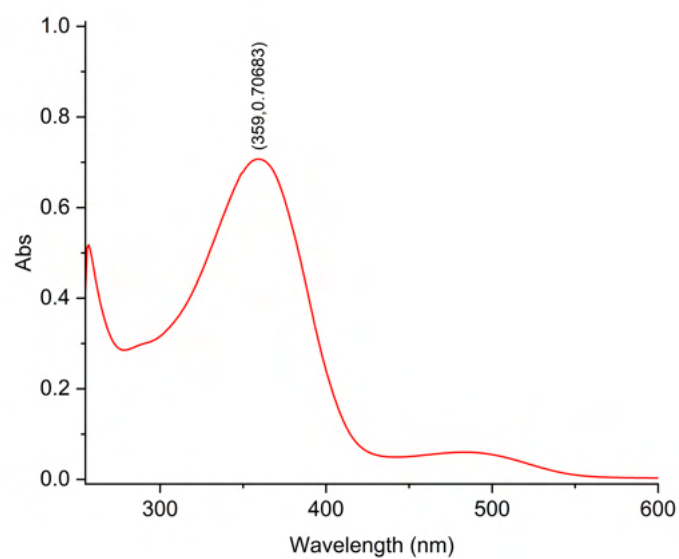
Figure S81. The UV-Vis spectrum of HP-β-CD·**2** (method 1, 1.77 mg) in DMSO (6 mL).

A_{max} = 0.70683, ε = 19586.5 M^{-1} cm^{-1}

c = 36.09 μM

$m = (36.09 \times 10^{-6}) \times 0.006 \times 341 = 0.0738$ mg

mass % = 4.17%
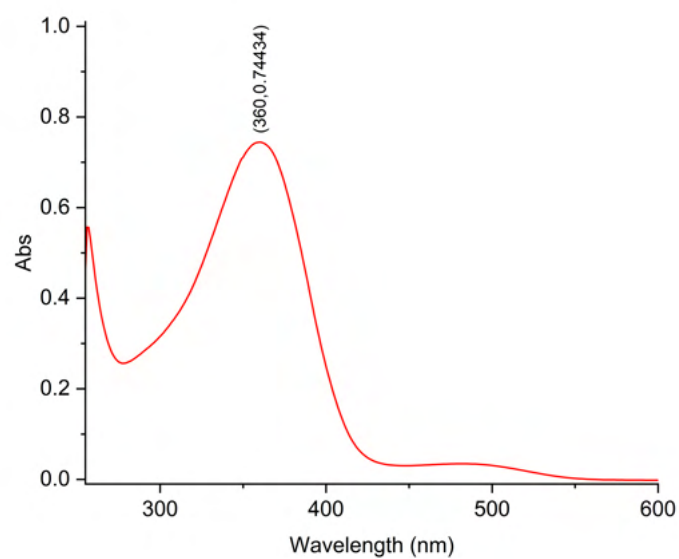
Figure S82. The UV-Vis spectrum of HP-β-CD·**2** (method 2, 3.27 mg) in DMSO (10 mL).

A_{max} = 0.74434, ε = 19586.5 M^{-1} cm^{-1}

c = 38.00 μM

m = (38.00 × 10^{-6}) × 0.01 × 341 = 0.129 mg

mass % = 3.96%
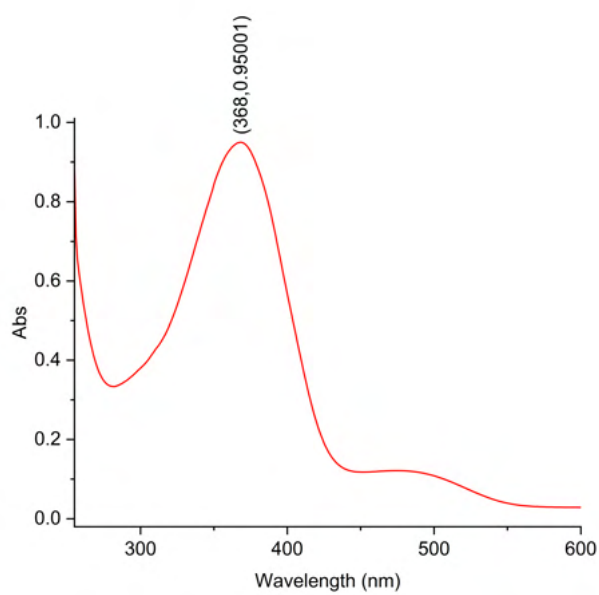
Figure S83. The UV-Vis spectrum of HP-β-CD·**2** (method 3, 1.28 mg) in DMSO (5 mL).

A_{max} = 0.95001, ε = 19586.5 M^{-1} cm^{-1}

c = 48.50 μM

m = (48.50 × 10^{-6}) × 0.005 × 341 = 0.0827 mg

mass % = 6.46%
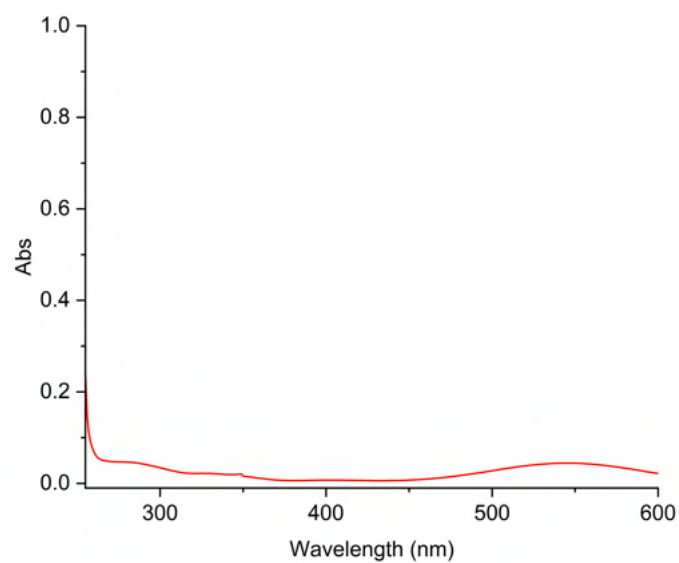
Figure S84. The UV-Vis spectrum of HP-β-CD·**3** (method 1, 4.00 mg) in DMSO (10 mL). The A_{max} for this compound was too low for calculations to be performed.
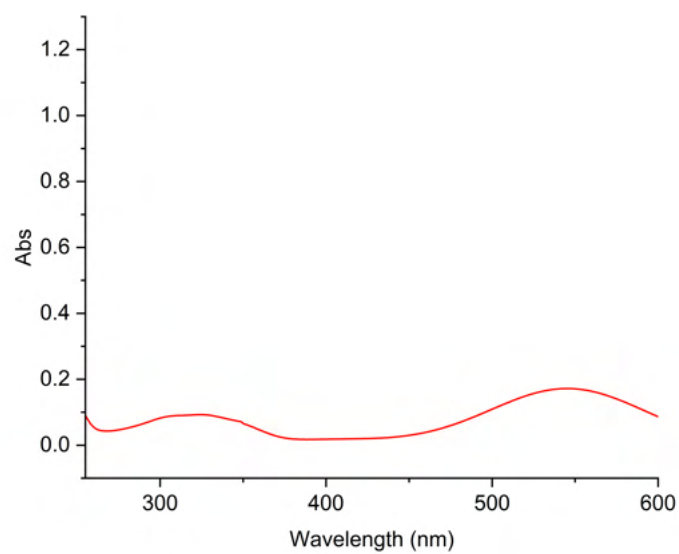
Figure S85. The UV-Vis spectrum of HP-β-CD·**3** (method 2, 5.17 mg) in DMSO (10 mL). The A_{max} for this compound was too low for calculations to be performed.
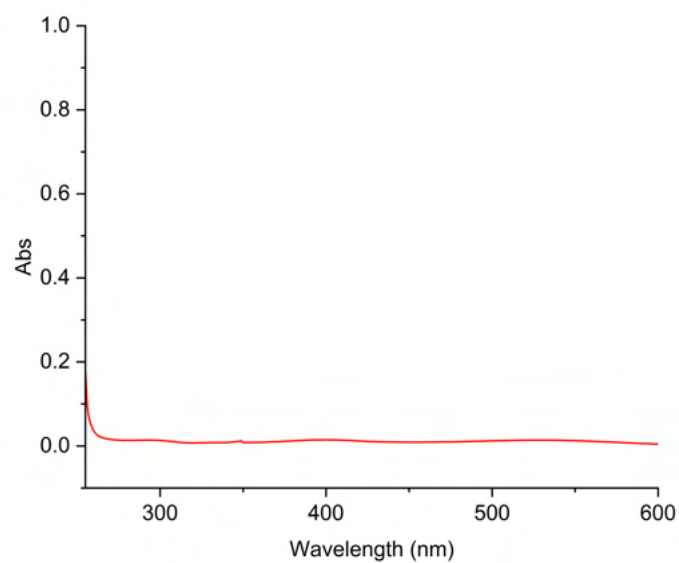
Figure S86. The UV-Vis spectrum of HP-β-CD·**3** (method 3, 4.31 mg) in DMSO (10 mL). The A_{max} for this compound was too low for calculations to be performed.
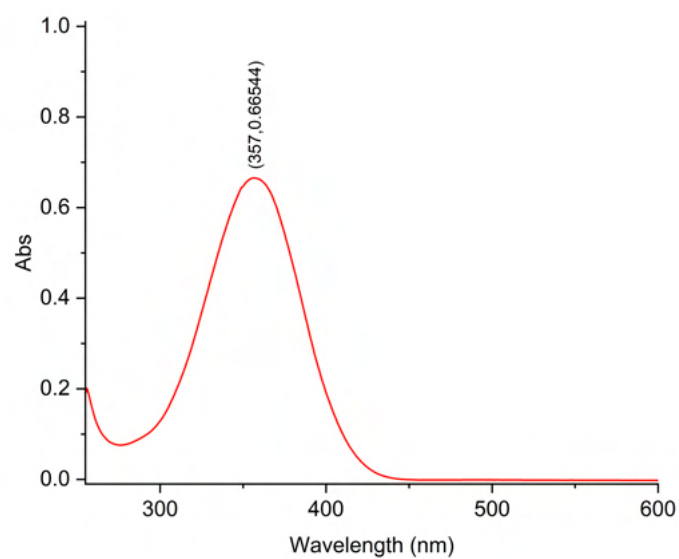
Figure S87. The UV-Vis spectrum of HP-β-CD·**4** (method 1, 4.42 mg) in DMSO (10 mL).

A_{max} = 0.66544, ε = 24165.0 M^{-1} cm^{-1}

c = 27.54 μM

Solution was diluted by 1.5 so true concentration = 41.31 μM

m = (41.31 × 10^{-6}) × 0.01 × 315 = 0.130 mg

mass % = 2.94%
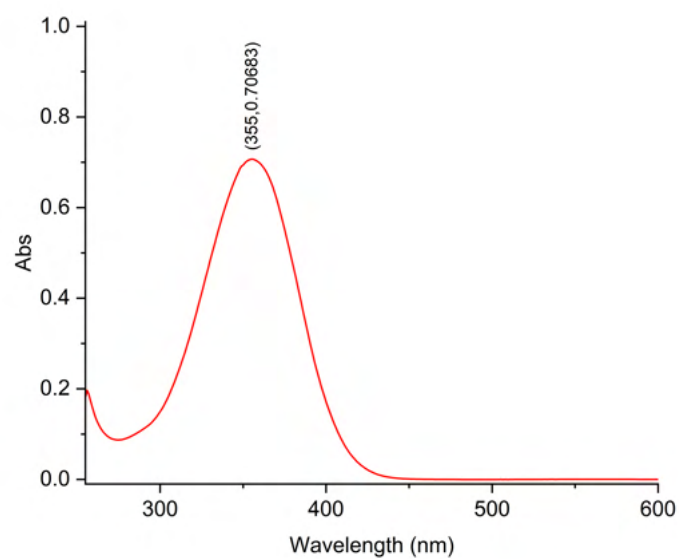
Figure S88. The UV-Vis spectrum of HP-β-CD·**4** (method 2, 3.82 mg) in DMSO (10 mL).

A_{max} = 0.70683, ε = 24165.0 M^{-1} cm^{-1}

c = 29.25 μM

Solution was diluted by 2 so true concentration = 58.50 μM

m = (58.5 × 10^{-6}) × 0.01 × 315 = 0.184 mg

mass % = 4.82%
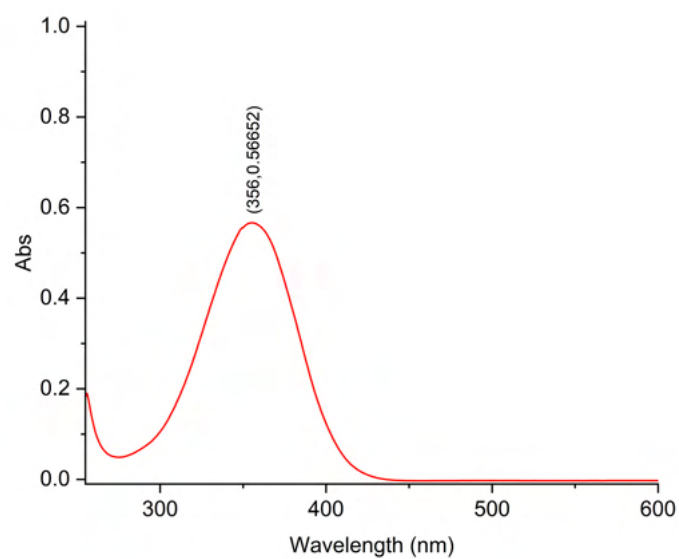
Figure S89. The UV-Vis spectrum of HP-β-CD·**4** (method 3, 3.66 mg) in DMSO (10 mL).

A_{max} = 0.56652, ε = 24165.0 M^{-1} cm^{-1}

c = 23.44 μM

Solution was diluted by 3 so true concentration = 70.33 μM

m = (70.33 × 10^{-6}) × 0.01 × 315 = 0.222 mg

mass % = 6.05%
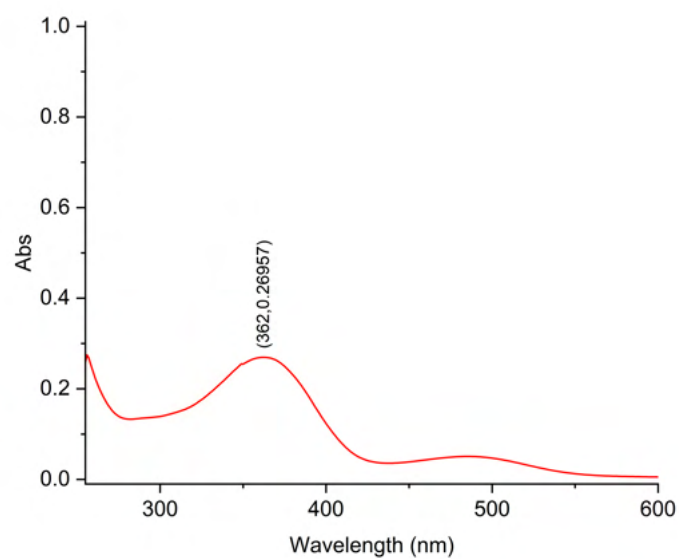
Figure S90. The UV-Vis spectrum of HP-β-CD·**5** (method 1, 3.13 mg) in DMSO (10 mL).

A_{max} = 0.26957, ε = 15683.3 M^{-1} cm^{-1}

c = 17.19 μM

m = (17.19 × 10^{-6}) × 0.01 × 331 = 0.0569 mg

mass % = 1.82%
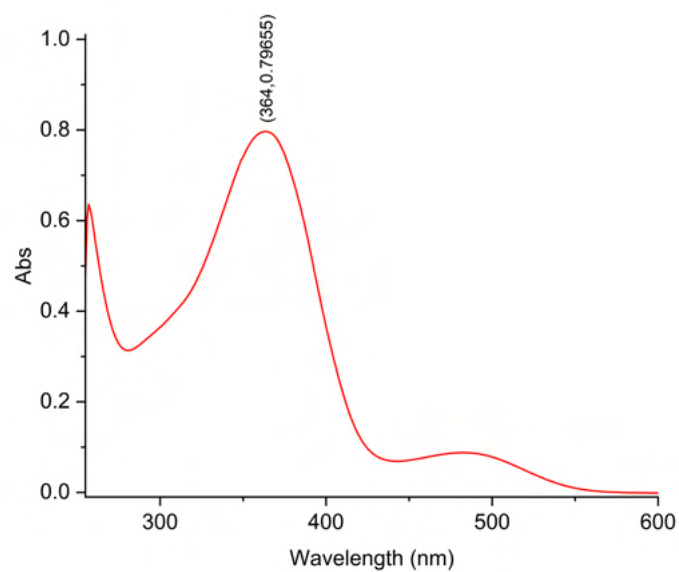
Figure S91. The UV-Vis spectrum of HP-β-CD·**5** (method 2, 3.56 mg) in DMSO (10 mL).

A_{max} = 0.79655, ε = 15683.3 M⁻¹ cm⁻¹

c = 50.79 μM

m = (50.79 × 10⁻⁶) × 0.01 × 331 = 0.168 mg

mass % = 4.72%
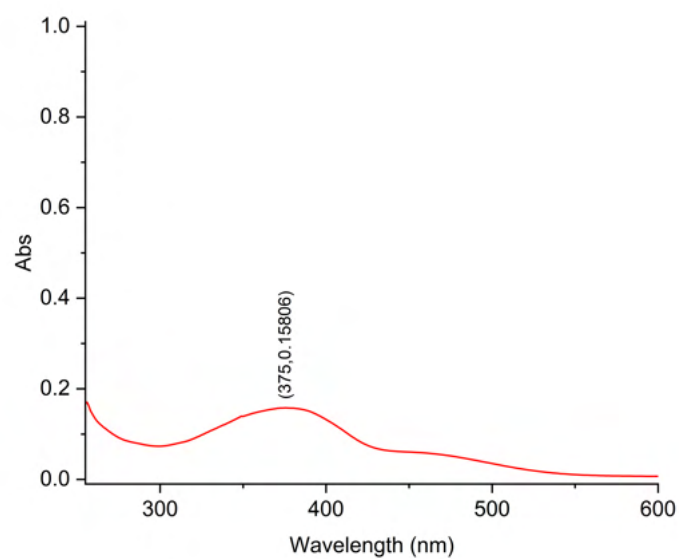
Figure S92. The UV-Vis spectrum of HP-β-CD·**5** (method 3, 3.62 mg) in DMSO (10 mL).

A_{max} = 0.15806, ε = 15683.3 M⁻¹ cm⁻¹

c = 10.08 μM

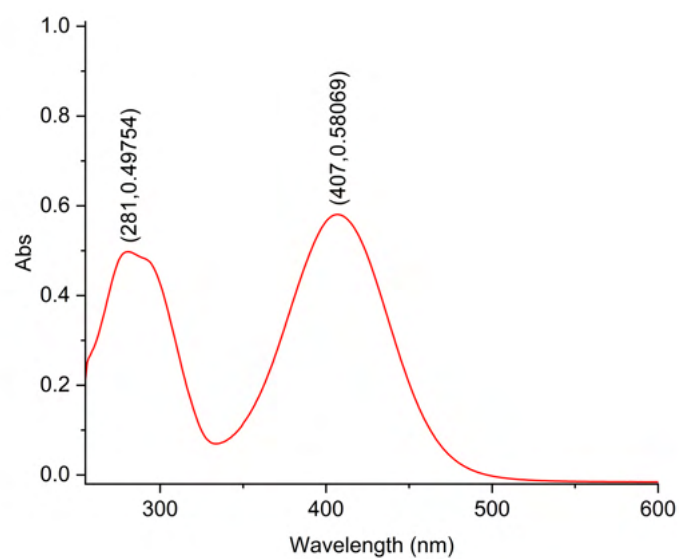m = (50.79 × 10⁻⁶) × 0.01 × 331 = 0.0334 mg

mass % = 0.92%
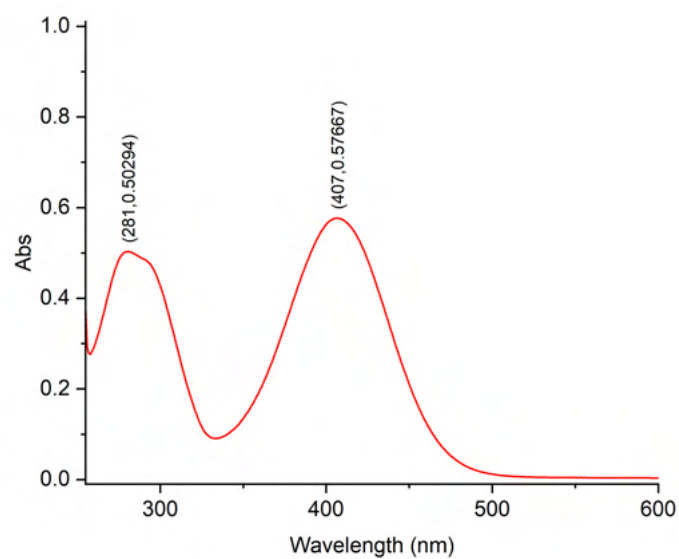
Figure S93. The UV-Vis spectrum of HP-β-CD·**6** (method 1, 1.60 mg) in DMSO (10 mL), in the presence of perchloric acid (0.01 M).

$A_{max} = 0.57667$, $\varepsilon = 24000.0$ M^{-1} cm^{-1}

$c = 24.03$ μM

$m = (24.03 \times 10^{-6}) \times 0.01 \times 367 = 0.0887$ mg

mass % = 5.51%
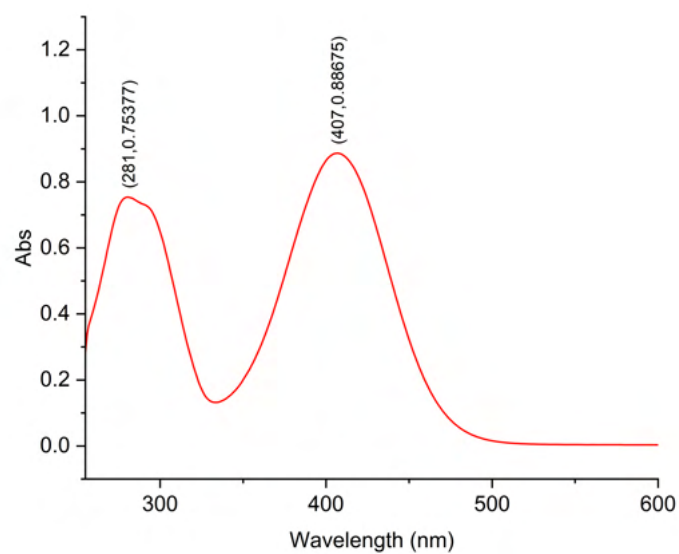
Figure S94. The UV-Vis spectrum of HP-β-CD·**6** (method 2, 1.99 mg) in DMSO (10 mL), in the presence of perchloric acid (0.01 M).

A_{max} = 0.88675, ε = 24000.0 M^{-1} cm^{-1}

c = 36.95 μM

m = (36.95 × 10^{-6}) × 0.01 × 367 = 0.136 mg

mass % = 6.81%

Figure S95. The UV-Vis spectrum of HP-β-CD·**6** (method 3, 4.85 mg) in DMSO (10 mL), in the presence of perchloric acid (0.01 M).

A_{max} = 0.58069, ε = 24000.0 M^{-1} cm^{-1}

c = 24.42 μM

m = (24.42 × 10^{-6}) × 0.01 × 367 = 0.088 mg

mass % = 1.83%

9.3 UV-Vis of Inclusion Complexes in H₂O

UV-Vis spectra of the four inclusion complex mixtures were collected in H₂O. For the mass percentage quantifications, it did not matter whether the inclusion complex was retained when dissolved in DMSO as only the concentration of compound present was necessary for calculations. A UV-Vis spectrum of free transporter **1** in H₂O could not be obtained due to the poor solubility of the compound in this solvent. Therefore, UV-Vis absorbance can be attributed to the transporter molecule when the complex is dissolved in water would indicate an inclusion complex has been formed.

The similarity in the absorbance profile of the inclusion mixture spectra in H₂O and the corresponding free transporter spectrum in DMSO heavily suggested inclusion complexes had been fabricated successfully. The small peak at higher wavelengths in the DMSO spectrum is due to a slight deprotonation. ⌷⌷ The UV-Vis spectrum of HP-β-CD·**6** obtained in H₂O contains a large amount of noise, attributed to the formation of microdispersions in the experimental solution. This could potentially be due to the partial decomplexation and subsequent precipitation of the transporter. The overlaid spectra can be viewed below.
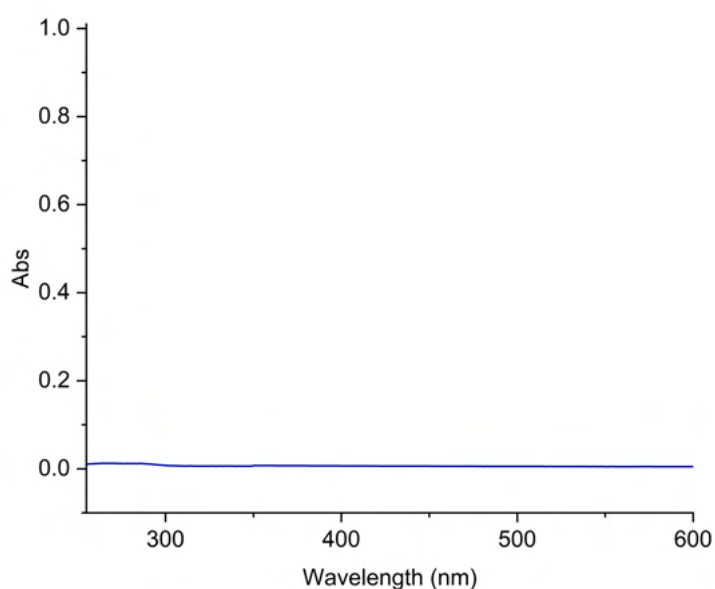

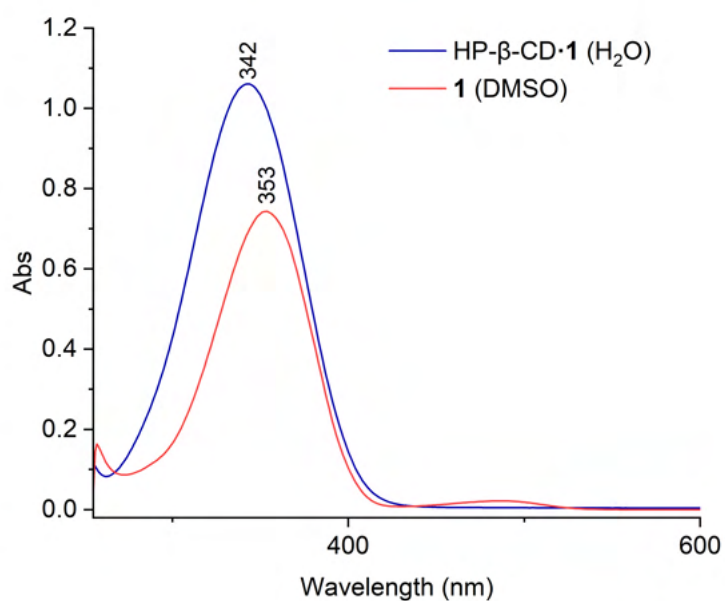**Figure S96**. The UV-Vis trace of HP-β-CD in water.

Figure S97. An overlay of the UV-Vis traces of free transporter **1** dissolved in DMSO (red) and of inclusion complex HP-β-CD·**1** in water (blue).
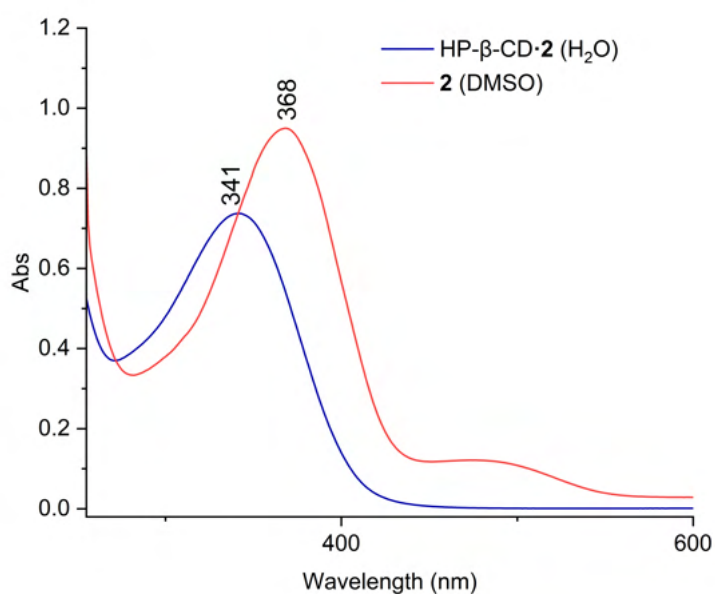

Figure S98. An overlay of the UV-Vis traces of free transporter **2** dissolved in DMSO (red) and of inclusion complex HP-β-CD·**2** in water (blue).
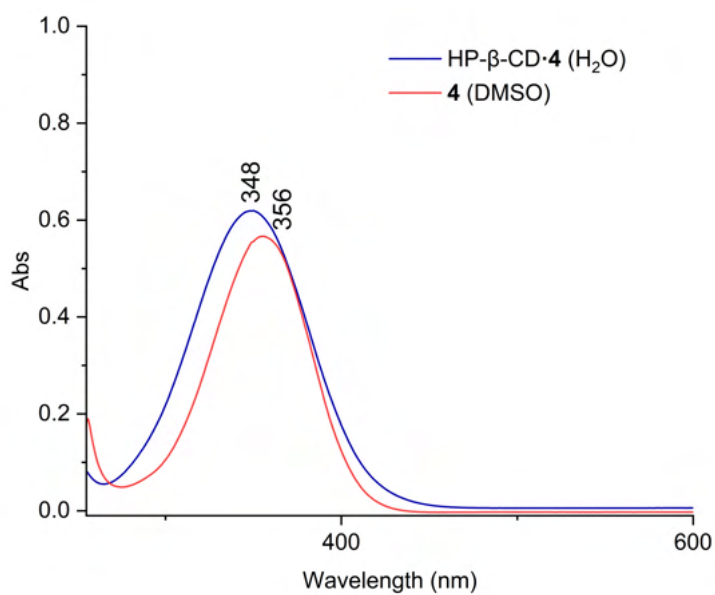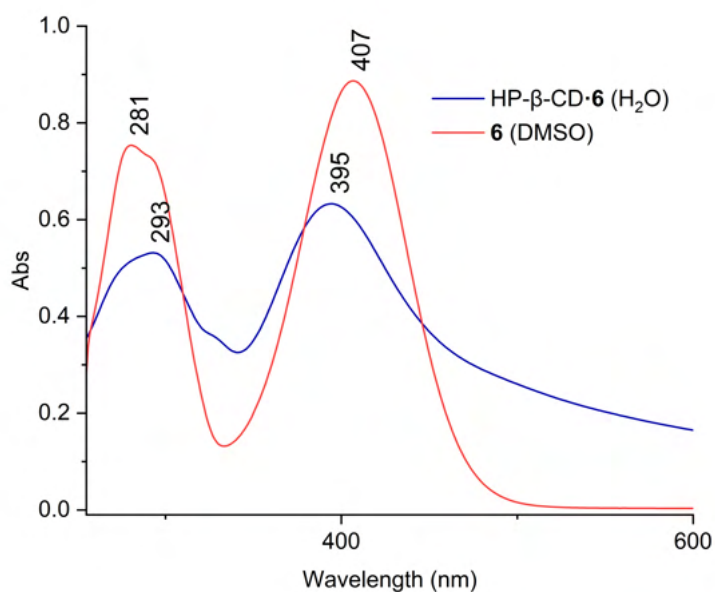
Figure S99. An overlay of the UV-Vis traces of free transporter **4** dissolved in DMSO (red) and of inclusion complex HP-β-CD·**4** in water (blue).

Figure S100. An overlay of the UV-Vis traces of free transporter **6** dissolved in DMSO (red) and of inclusion complex HP-β-CD·**6** in water (blue). The large amount of noise in the spectrum of HP-β-CD·**6** was attributed to the formation of microdispersions in the experimental solution.

10. Infrared Spectroscopy Analysis

Infrared spectroscopy was also employed to examine the inclusion complexes. This technique can be used to identify perturbations in the vibrational modes of the CD host and the guest molecule, which may be due to interactions between the two molecules in the solid-state.[22] A decrease in intensity, a shift in wavenumber, or the disappearance of characteristic stretches associated with the guest can all provide evidence towards the formation of an inclusion complex due to restriction of the guests stretching vibrations when included within the HP-β-CD cavity. Attenuated total reflectance (ATR) Fourier-transform infrared (FTIR) spectra were recorded for free HP-β-CD, free transporters **1**, **2**, **4**, and **6**, and each inclusion complex with the respective transporter. Additionally, ATR spectrums were collected for a physical mixture (P.M) of each transporter and HP-β-CD, prepared by combining an equimolar amount of transporter and HP-β-CD in a mortar and pestle before grinding for 10 min, yielding an amorphous and homogenous solid mixture.

The FTIR spectra relevant to compound **1** can be viewed in **Figure S105**. The FTIR spectrum of HP-β-CD (**Figure S101**) showed prominent absorption bands at 3311 cm^{-1} (O–H stretching vibrations), 2973, and 2915 cm^{-1} (C–H stretching vibrations), and 1151, 1077 and 1023 cm^{-1} (C–H, C–O stretching vibration). The spectrum of **1** (**Figure S102**) consisted of a sharp

absorption band at 3357 cm^{-1} (urea N−H stretching vibration), two strong peaks at 2897 and 2847 cm^{-1} (adamantyl and methyl spacer C−H stretching vibrations), an absorption band at 1671 cm^{-1} (urea C=O stretching vibration) and prominent bands at 1547 and 1329 cm^{-1} which denote the asymmetric and symmetric stretches of the NO$_2$ group. Peaks at 1223, 846, and 638 cm^{-1} are associated with aromatic ring vibrations.

The P.M spectrum (**Figure S103**) contained stretches associated with both compounds and, in general, the bands appeared at the same frequencies as those in the spectra of the single components. At higher wavenumbers (above 2800 cm^{-1}), the bands associated with **1** appeared more prominently. The FTIR spectrum of HP-β-CD·**1** (**Figure S104**) closely resembles the spectrum of HP-β-CD as a free host molecule. There is a high mass content of HP-β-CD present in the inclusion complex, and bands associated with this component are much more intense, leading to overlapping and obscuring of the bands associated with **1**.[22] Previous studies have reported that stretches found between 3600–2800 cm^{-1} rarely provide evidence for the formation of an inclusion complex due to the intensity of the HP-β-CD bands in this region.[23, 24] This is unfortunate, as the bands in the spectra of free **1** (**Figure S102**) attributed to the adamantyl C−H stretch vibrations, which should be affected by the inclusion process, were reported within this region.

The peak at 1325 cm^{-1} in the spectrum of HP-β-CD·**1** can be attributed to the symmetric stretch of the NO$_2$ group present in **1** and confirms the presence of the transporter in the inclusion complex. The intensity of the band at 1231 cm^{-1} (aromatic stretch) is greater in the spectrum for the free guest molecule compared to the band at 1325 cm^{-1} (NO$_2$ group stretch), which is diminished in the spectrum of HP-β-CD·**1**. The peak at 1231 cm^{-1} can be attributed to the stretch vibration of the aromatic C−H bonds. A decrease in the intensity of this band suggests that vibration of the aromatic C−H bonds is restricted by interactions with the HP-β-CD cavity, whereas the NO$_2$ bonds remain unaffected. The complete disappearance of the band at 1671 cm^{-1} indicates that vibration of the urea carbonyl may also be inhibited due to interactions with the HP-β-CD cavity. However, this could also be an artefact of the small mass amount of transporter present in the complex.

The FTIR spectra relevant to compound **2** are displayed in **Figure S109**. The spectrum of free **2** (**Figure S106**) consisted of a sharp band at 3362 cm^{-1} attributed to the thiourea N−H stretch

vibration, peaks at 2987 and 2893 cm^{-1} corresponding to the adamantyl and methyl spacer C−H stretch vibrations. The same spectra also exhibited NO$_2$ group vibrations at 1509 and 1337 cm^{-1}, a characteristic C=S vibration band at 1256 cm^{-1}, and several other aromatic vibration peaks. Interestingly, the N−H vibration band was not visible in the spectrum of the P.M (**Figure S107**) but did appear in the spectrum of HP-β-CD·**2** (**Figure S108**). A number of bands attributed to guest molecule **2** were visible in the spectrum of HP-β-CD·**2**. Correlating stretches present in both the spectra of **2** and HP-β-CD·**2** were found at 1563/1545 cm^{-1}, 1509/1504 cm^{-1}, 1336/1324 cm^{-1}, and 1224/1230 cm^{-1}. The band at 1256 cm^{-1} was present in the spectrum of the P.M but disappeared entirely in the spectrum of HP-β-CD·**2** (**Figure S108**), suggesting that the formation of the inclusion complex inhibits vibration of the C=S bond. The inclusion of the adamantyl group in the HP-β-CD cavity is more likely to affect the vibration of the C=S bond than the aromatic C−H bonds because the thiourea is located closer to the adamantyl moiety. In the IR spectrum of HP-β-CD·**4**, peaks attributed to compound **4** are visible at 2902, 1667 and 1503 cm^{-1}. There is a small upfield shift compared to the corresponding peaks in the spectrum of the free compound. In the spectrum of HP-β-CD·**6**, only peaks at 1415, 1331 and 850 cm^{-1} can be attributed to the transporter molecule.
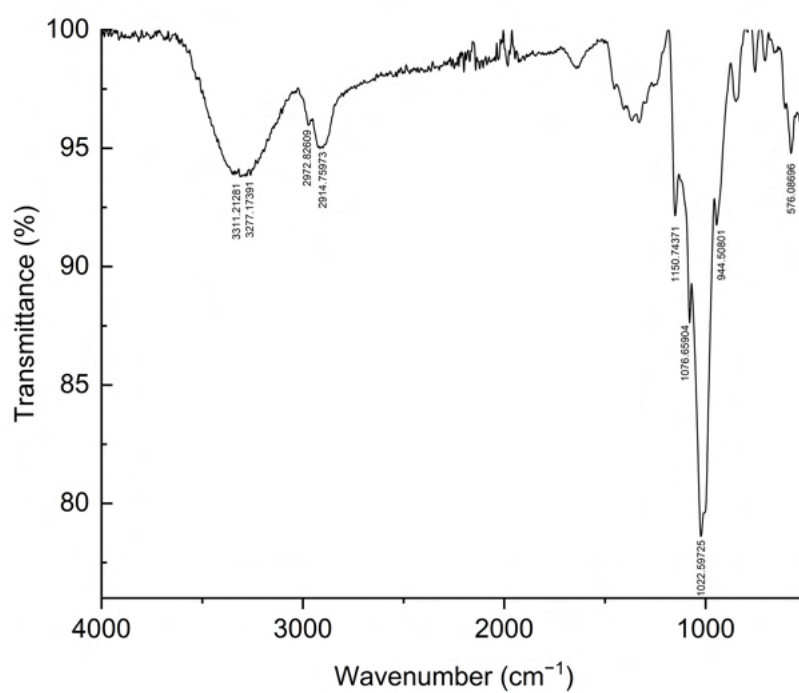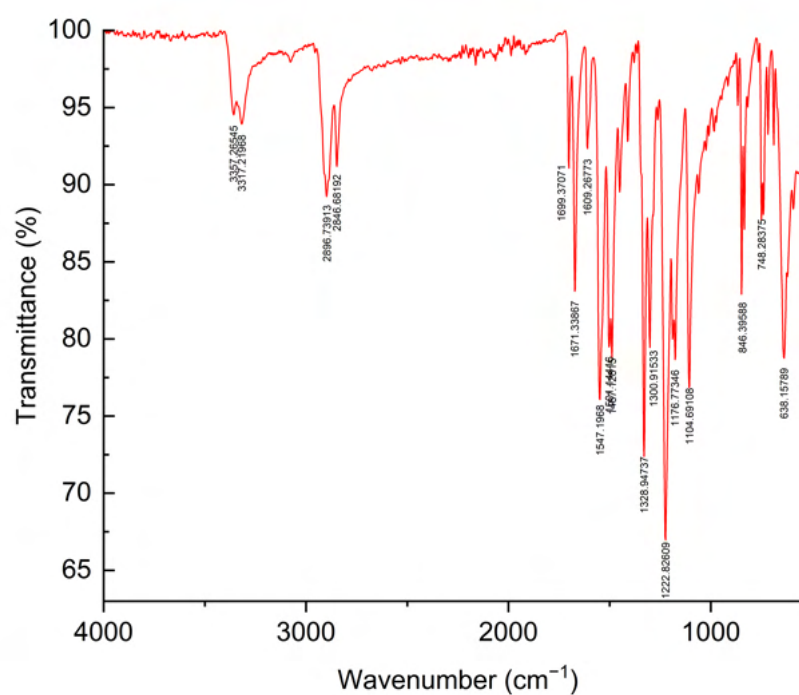
Figure S101. FTIR spectrum of HP-β-CD.

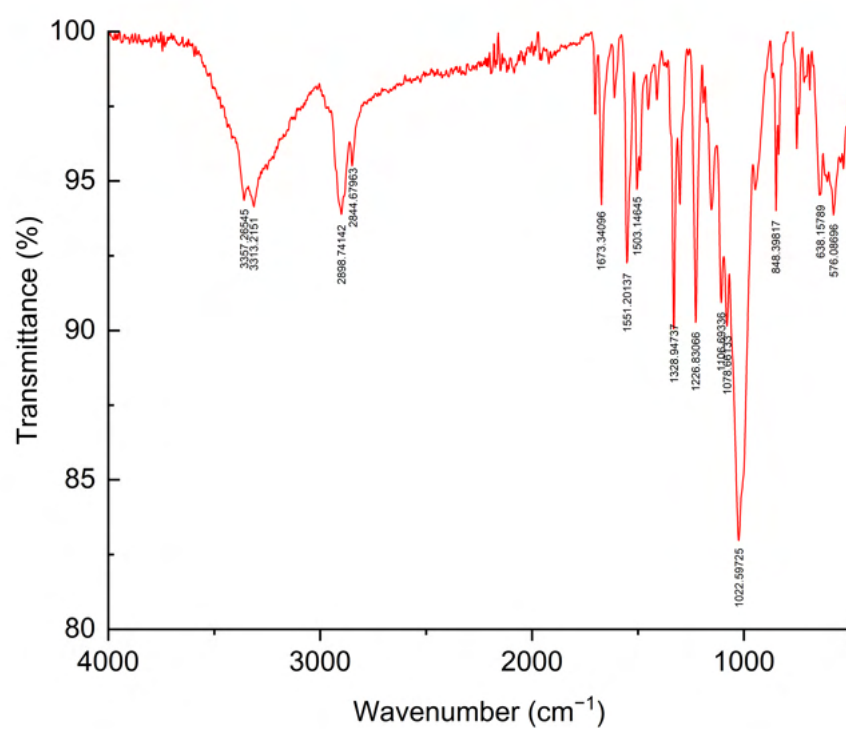**Figure S102**. FTIR spectrum of compound **1**.

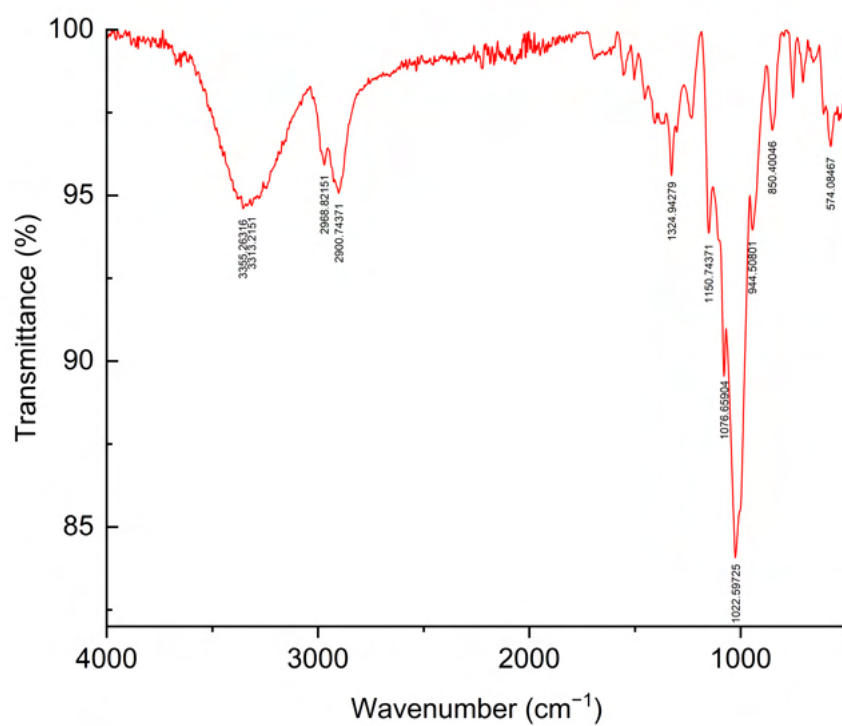**Figure S103**. FTIR spectrum of an equimolar physical mixture of HP-β-CD and compound **1**.
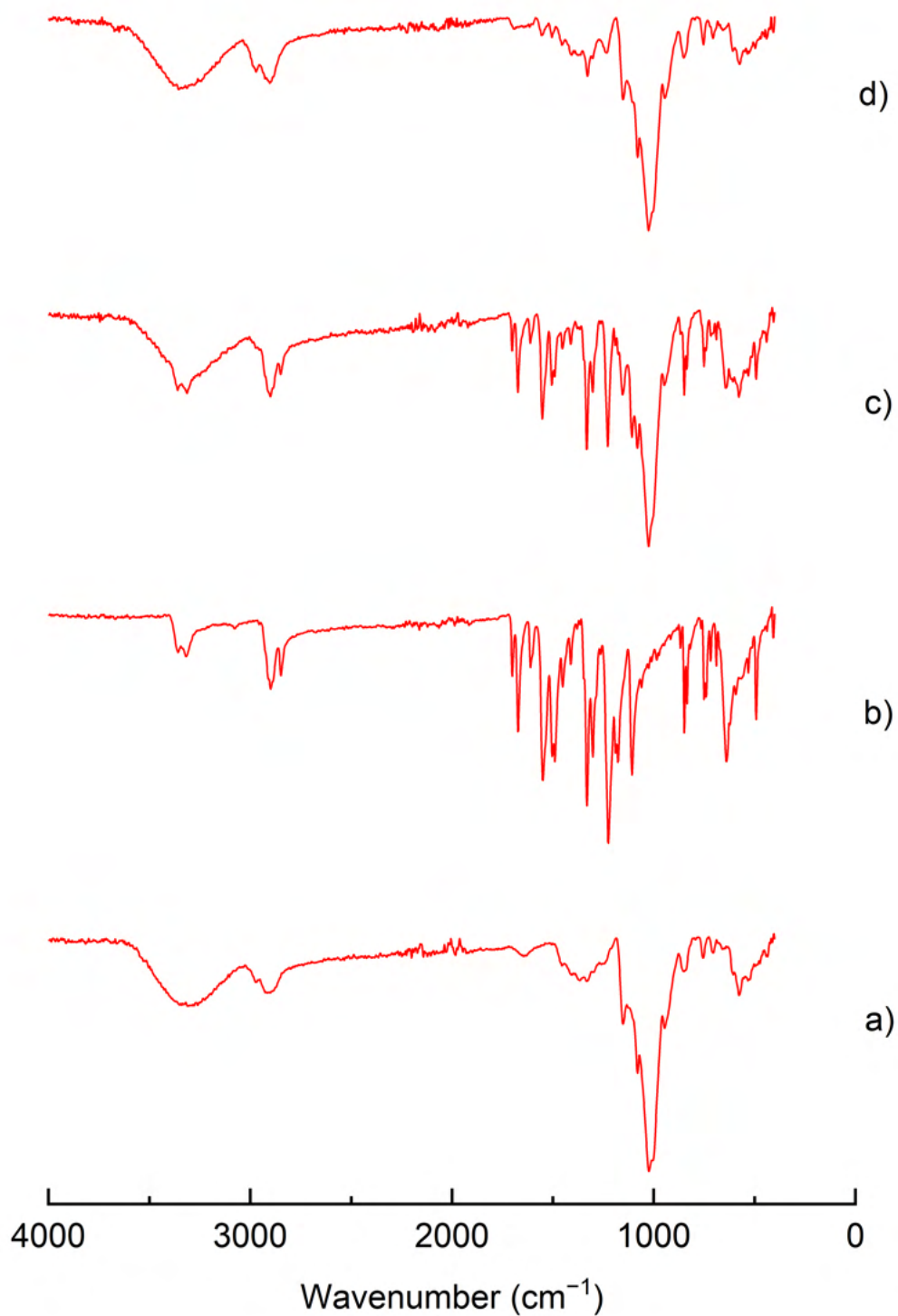

Figure S104. FTIR spectrum of HP-β-CD·**1**.

Figure S105. ATR-FTIR spectrum of (a) HP-β-CD, (b) **1**, (c) physical mixture of HP-β-CD and **1**, (d) inclusion complex HP-β-CD·**1**.
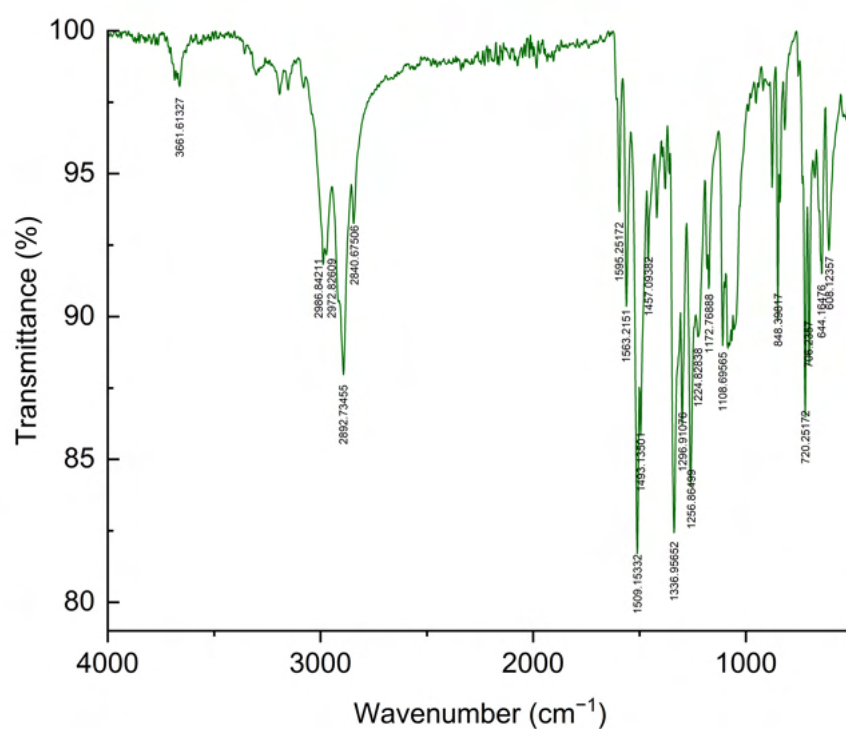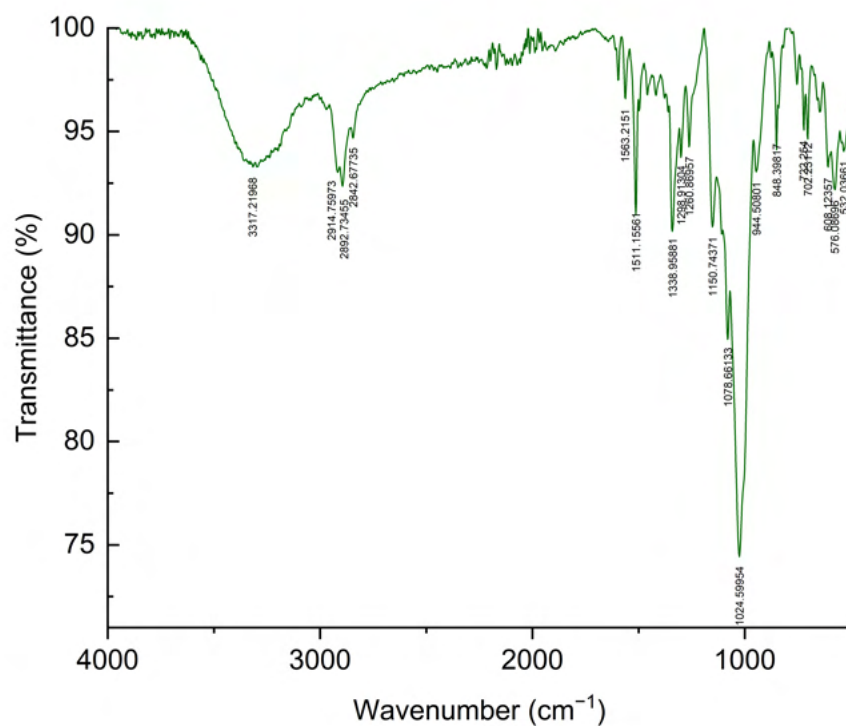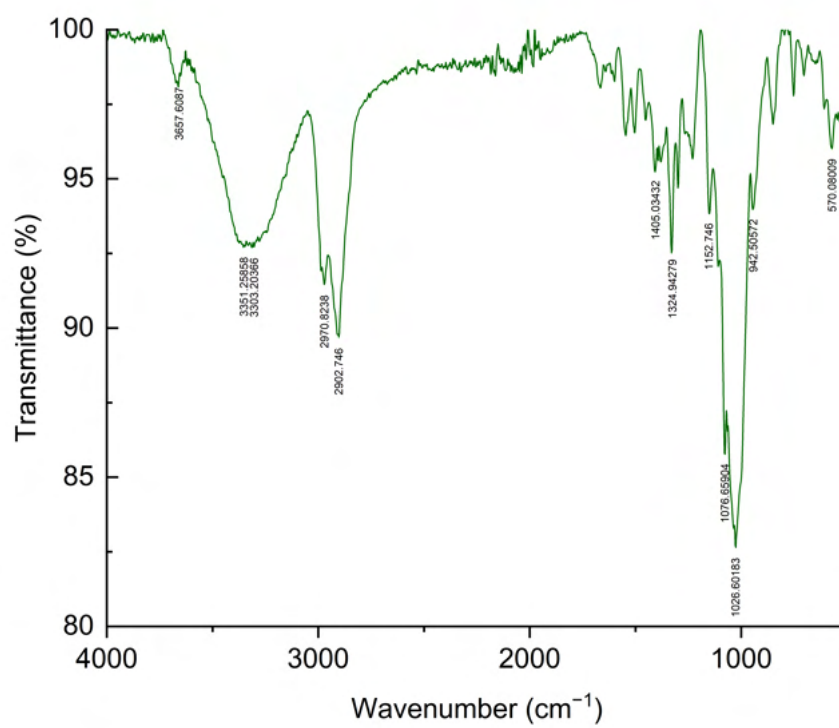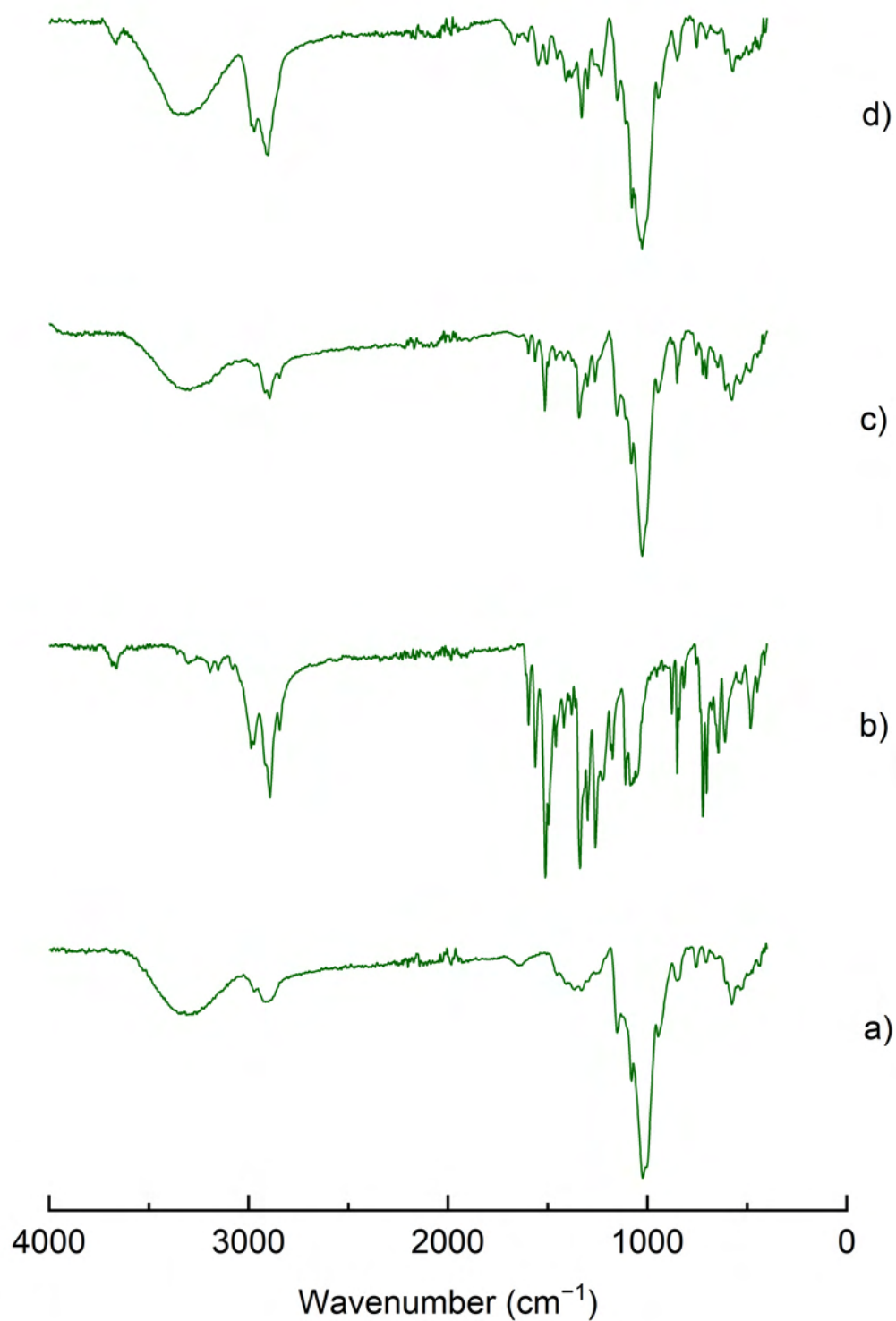
Figure S106. FTIR spectrum of compound **2**.

Figure S107. FTIR spectrum of an equimolar physical mixture of HP-β-CD and compound **2**.

Figure S108. FTIR spectrum of HP-β-CD·**2**.

Figure S109. ATR-FTIR spectrum of (a) HP-β-CD, (b) **2**, (c) physical mixture of HP-β-CD and **2**, (d) inclusion complex HP-β-CD·**2**.

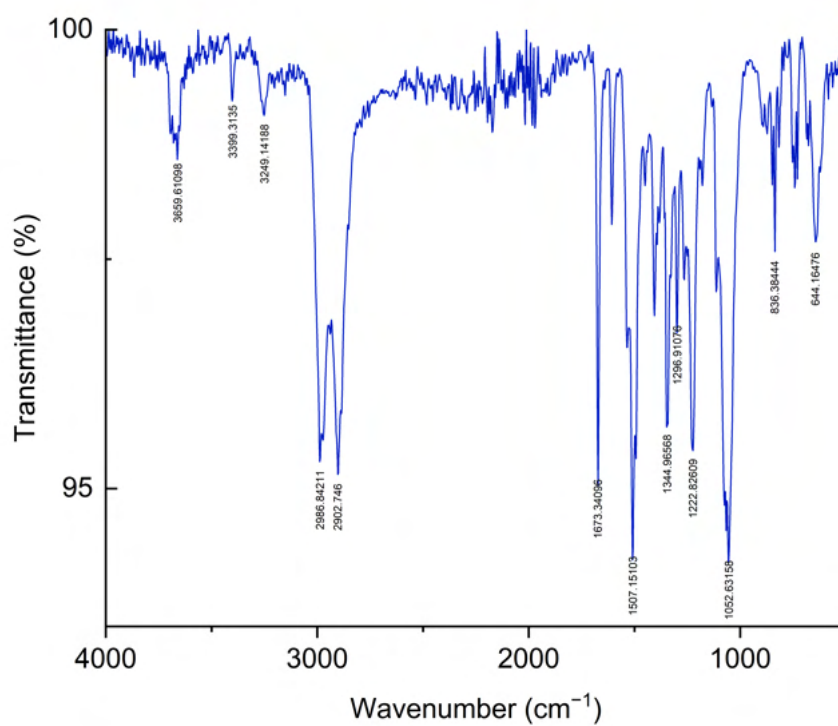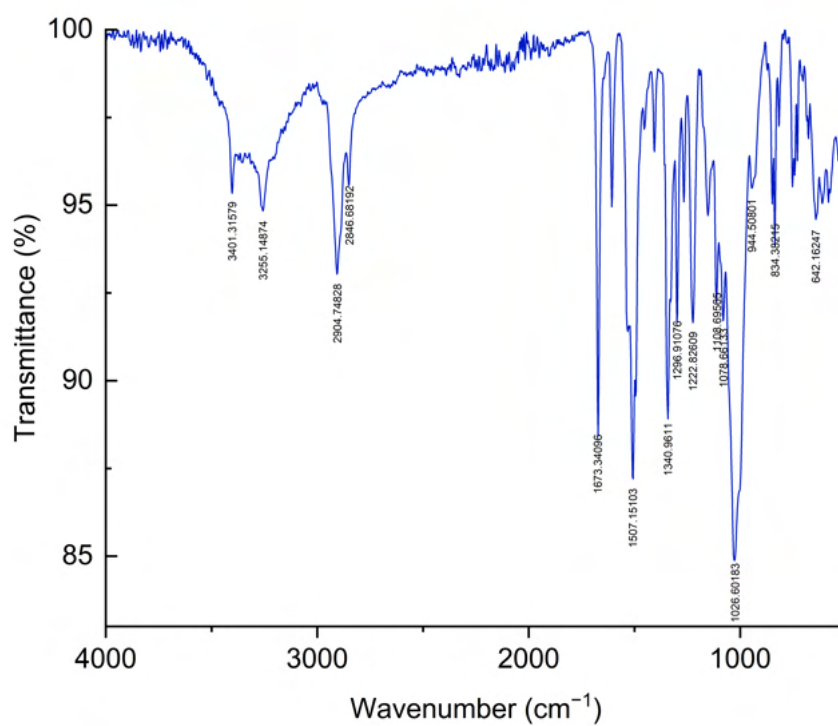**Figure S110**. FTIR spectrum of compound **4**.

Figure S111. FTIR spectrum of an equimolar physical mixture of HP-β-CD and compound **4**.
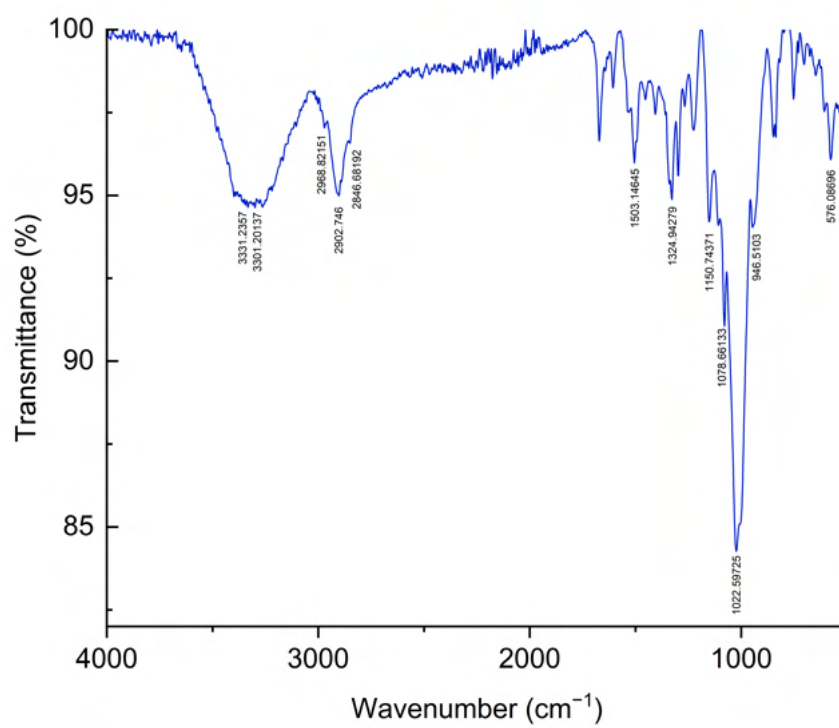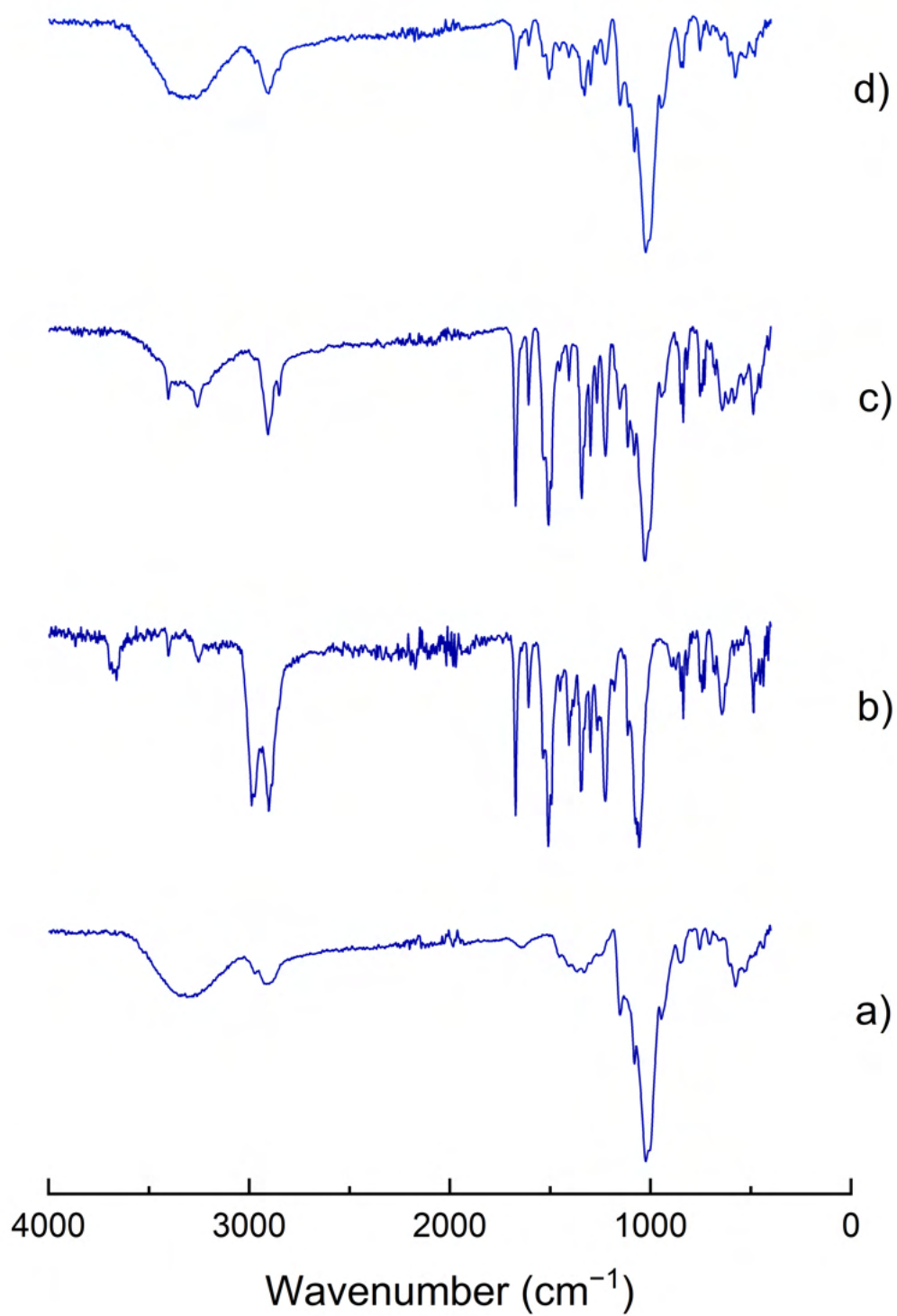
Figure S112. FTIR spectrum of HP-β-CD·**4**.

Figure S113. ATR-FTIR spectrum of (a) HP-β-CD, (b) **4**, (c) physical mixture of HP-β-CD and **4**, (d) inclusion complex HP-β-CD·**4**.

Figure S114. FTIR spectrum of compound **6**.

Figure S115. FTIR spectrum of an equimolar physical mixture of HP-β-CD and compound **6**.

Figure S116. FTIR spectrum of HP-β-CD·**6**.

Figure S117. ATR-FTIR spectrum of a) HP-β-CD, b) **6**, c) physical mixture of HP-β-CD and **6**, d) inclusion complex HP-β-CD·**6**.

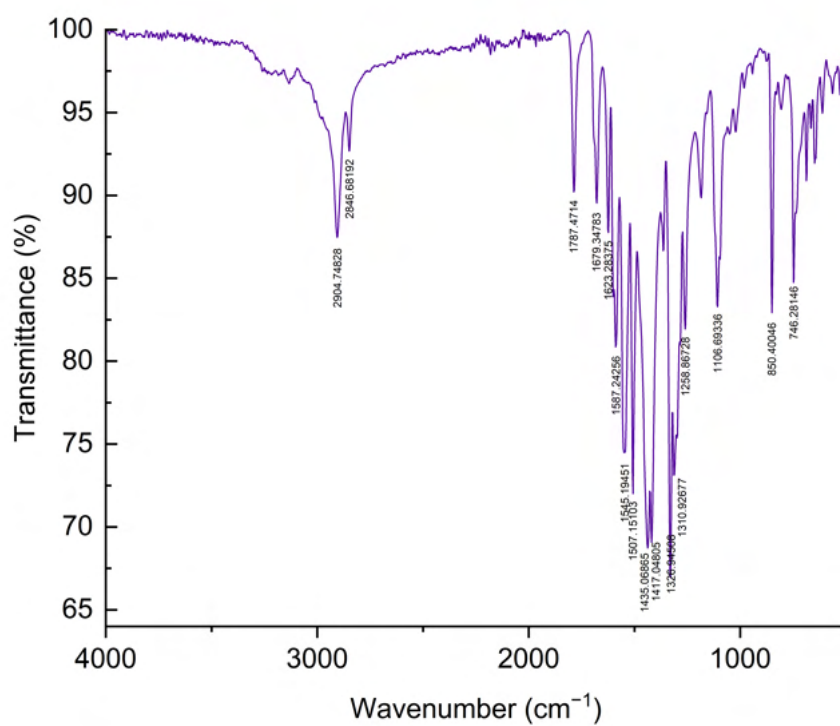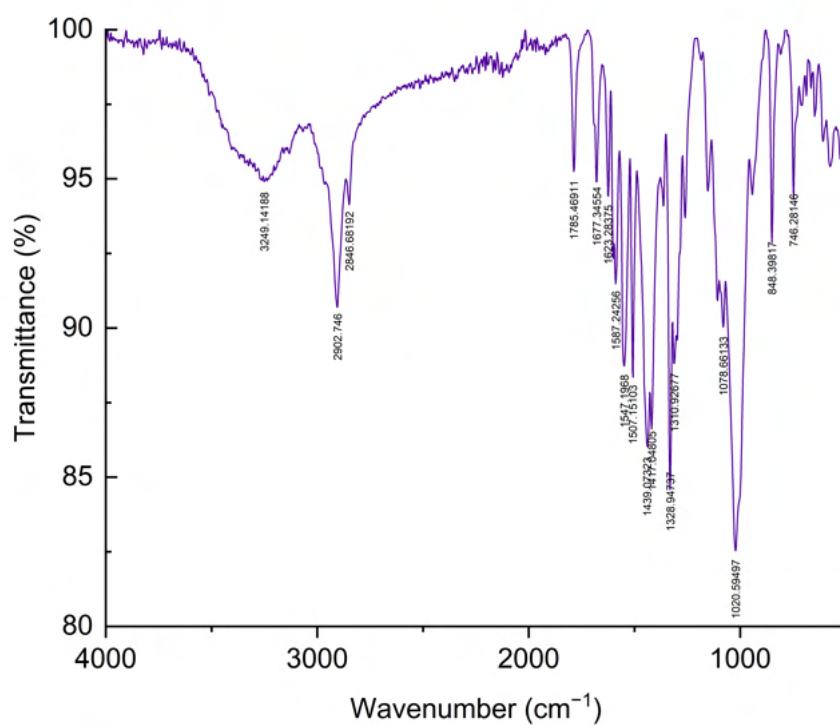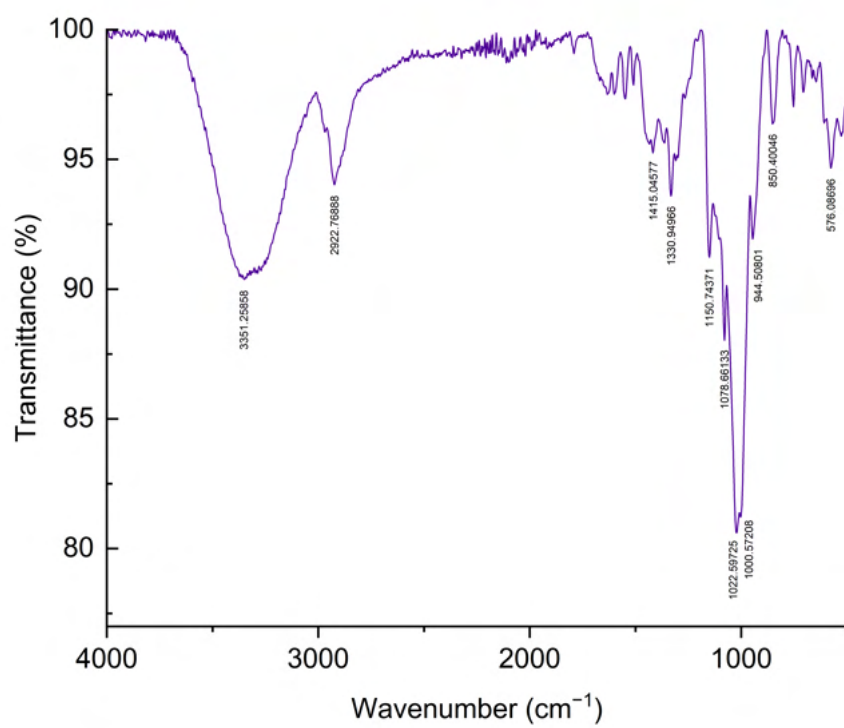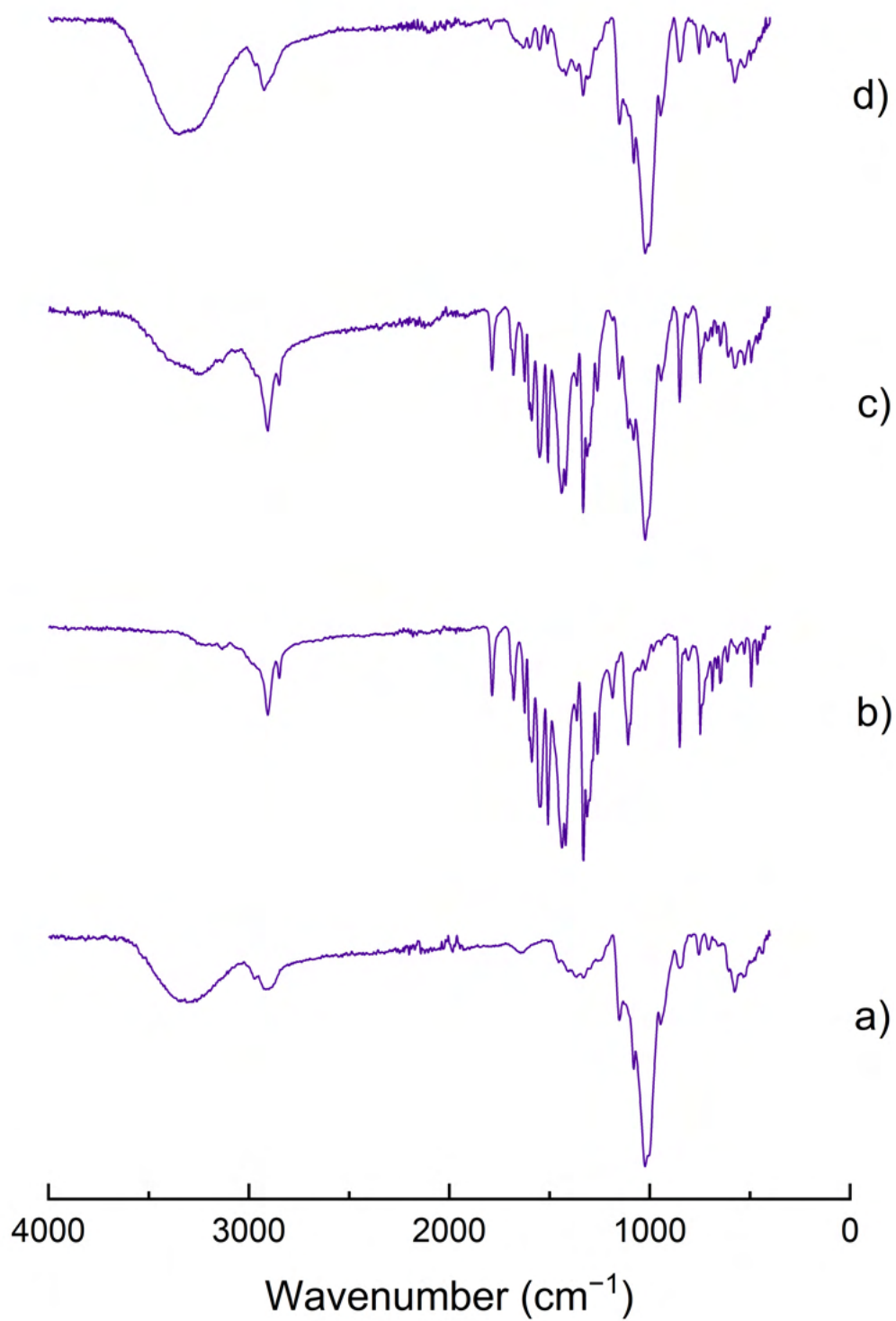## 11. 2D-NOESY ^{1}H NMR Spectroscopic Analysis

Two-dimensional NOESY ^{1}H NMR experiments were performed on the four inclusion complexes to investigate the spatial proximity of the HP-β-CD and transporter molecule hydrogens. The Nuclear Overhauser Effect (NOE) is the perturbation in intensity of an NMR resonance when a nearby proton is irradiated and occurs as a result of dipole–dipole cross-relaxation between the nuclei.[25] The effect is not governed by the through-bond relationship of the two nuclei and, instead, is a purely though-space interaction. The strength of the NOE is dependent on proximity and is typically observed between protons that are up to 4 Å apart. The appearance in the 2D-NOESY spectra of the inclusion complexes of NOE cross-peaks between resonances attributed with HP-β-CD and resonances attributed to the guest molecule would indicate that nuclei of the two species are close in space. The most likely reason for this occurrence is the presence of an inclusion complex.

The partial contour plot for the 2D NOESY spectrum of HP-β-CD·**1** can be seen in **Figure S118**. An appreciable correlation is seen between the signals attributed to the adamantyl protons of **1** and two of the signals relating to the protons of HP-β-CD, which are highlighted in **Figure S119**. On closer inspection (**Figure S120**), the cross-peaks can be attributed to the H^3 and H^5 protons of the macrocycle, which are located inside the HP-β-CD cavity (**Figure S44**). The proximity in space of the adamantyl protons and the protons of the interior surface of HP-β-CD strongly suggest that an inclusion complex has formed between the two components. This is complemented by the absence of cross-peak correlations associated with other HP-β-CD protons located on the outer surface of the structure (H^1, H^2 and H^4). The 2D NOESY spectra of HP-β-CD·**2** and HP-β-CD·**6** include similar cross-peak interactions between the adamantyl proton signals and the H^3/H^5 protons of HP-β-CD.

The cross-peak interactions present in the 2D NOESY spectrum of HP-β-CD·**4** are less clear (**Figure A.360**), but seem to suggest an NOE interaction occurs between the adamantyl protons and the H^5/H^6 protons of HP-β-CD. Cross-peak interactions with the H^3 protons are not visible. Compound **22** lacks a methyl spacer group, meaning the proximity of the urea moiety to the adamantyl group may limit the penetration of the transporter into the cavity if it enters from the narrower primary rim. The adamantyl is a better size match for the opening on the primary rim, so partial inclusion from this side would be more favourable. This would

explain the through-space interaction between the adamantyl protons and the H^6 protons of HP-β-CD, which are also located on the primary side of the structure.

Interestingly, cross-peak interactions were also visible between the H^3/H^5 protons, and the signals related to the aryl protons of the guest molecules. This was unexpected, as the compounds were designed with the intention that the adamantyl moiety would enter the cyclodextrin cavity. Several possibilities could explain the existence of NOE interactions between the aryl transporter protons and the interior cavity protons of HP-β-CD. Firstly, it could be that the adamantane sits in the primary rim of HP-β-CD whilst the remainder of the molecule penetrates the cavity. This would agree with the perfect size match that exists between adamantyl groups and β-CD derivatives, which other researchers have exploited. A second possibility is that the 1:1 host:guest complex is unselective, and either the *p*-nitrophenol group or the adamantyl moiety penetrates the cavity to form the inclusion complex. Finally, it may suggest that both ends of the transporter molecule are partially included inside a cyclodextrin molecule, forming a 2:1 host:guest complex. This theory would offer an explanation for the apparent HP-β-CD:transporter stoichiometries, which included more HP-β-CD than expected because the two components were combined during inclusion complex formation in equimolar amounts.
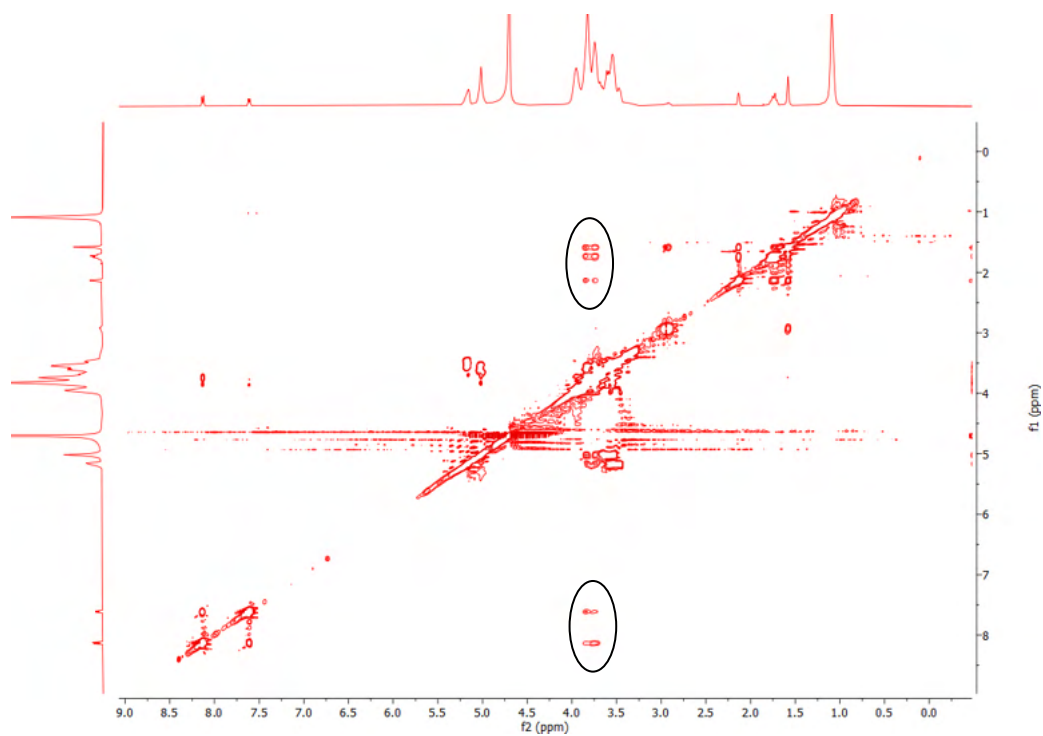
Figure S118. The 2D NOESY ^{1}H-NMR spectrum of HP-β-CD·**1** complex, in D$_2$O. Intermolecular cross-peak interactions between HP-β-CD and **1** have been circled.
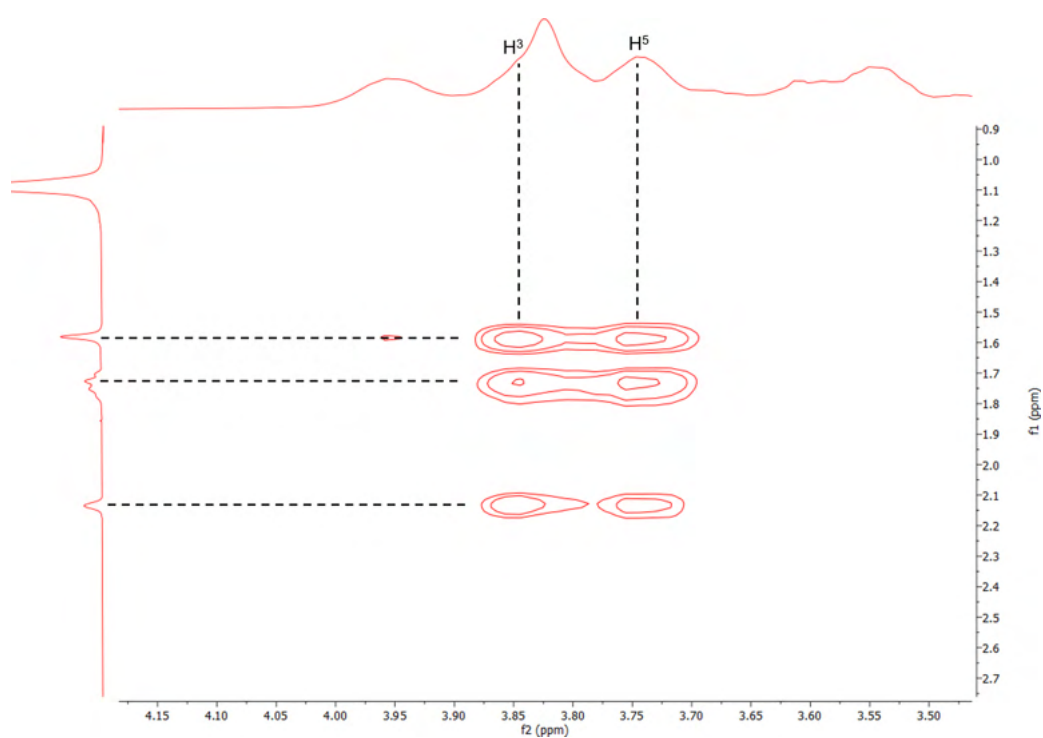

Figure S119. A magnified segment of the 2D NOESY ^{1}H-NMR spectrum of the HP-β-CD·**1** complex, showing the cross-peak interactions between the signals of the adamantyl protons

of **1** (δ = 1.58, 1.73, and 2.13 ppm) and the H^3 and H^5 protons of HP-β-CD (δ = 3.85 ppm and δ = 3.75 ppm, respectively).
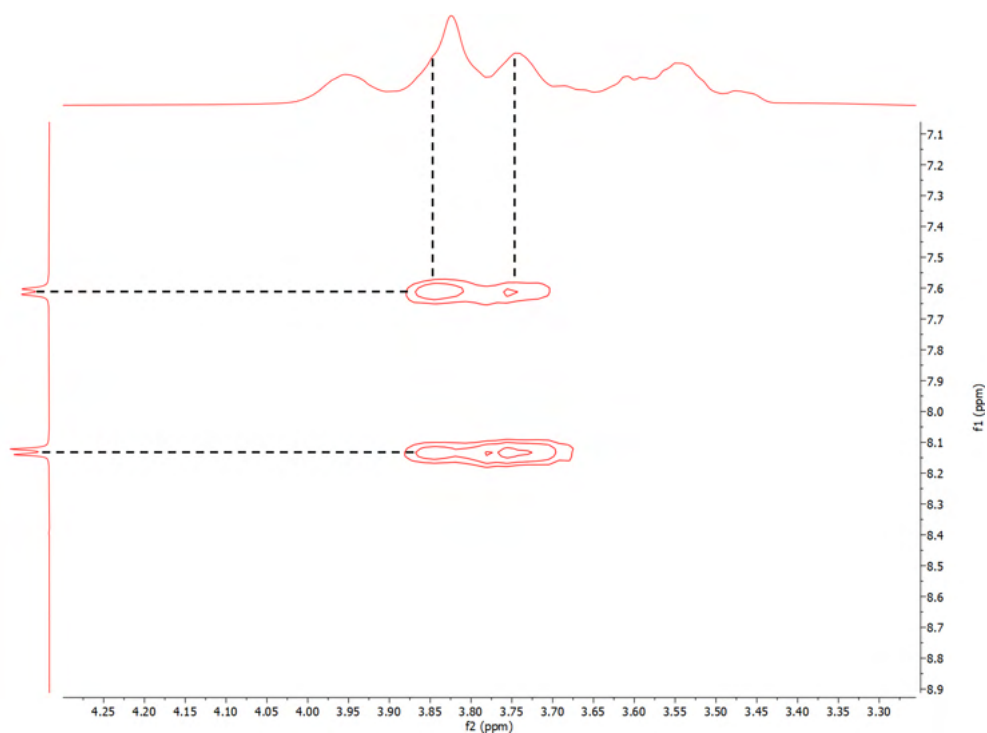

Figure S120. A magnified segment of the 2D NOESY ^{1}H-NMR spectrum of the HP-β-CD·**1** complex, showing the cross-peak interactions between the signals of the aromatic protons of **1** (δ = 7.61 and 8.13 ppm) and the H^3 and H^5 protons of HP-β-CD (δ = 3.85 ppm and δ = 3.75 ppm, respectively).
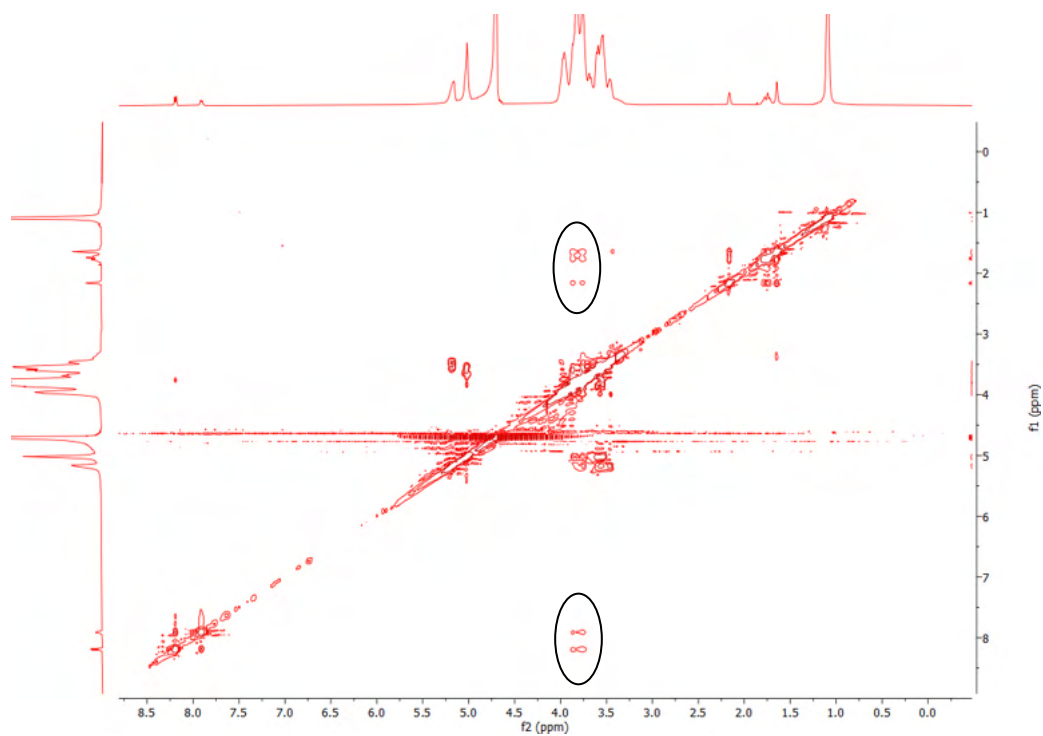
Figure S121. The 2D NOESY ^{1}H-NMR spectrum of HP-β-CD·**2** complex, in D$_2$O. Intermolecular cross-peak interactions between HP-β-CD and **2** have been circled.

Figure S122. A magnified segment of the 2D NOESY ^{1}H-NMR spectrum of the HP-β-CD·**2** complex, showing the cross-peak interactions between the signals of the adamantyl protons

of **2** (δ = 1.64, 1.76, and 2.16 ppm) and the H^3 and H^5 protons of HP-β-CD (δ = 3.85 ppm and δ = 3.75 ppm, respectively).
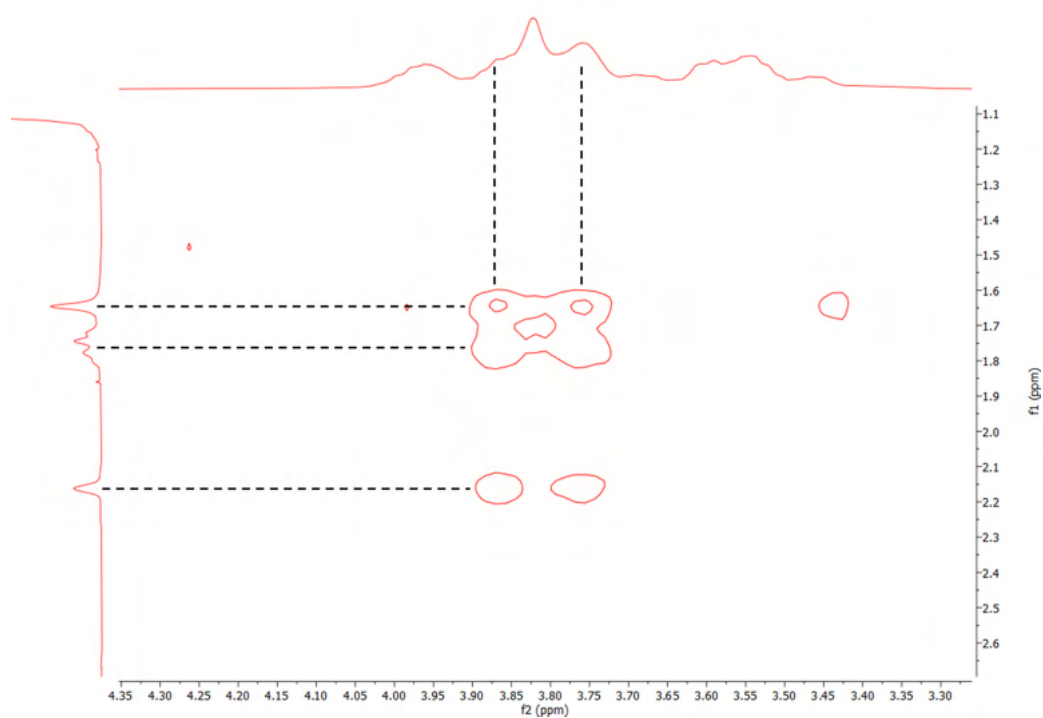

Figure S123. A magnified segment of the 2D NOESY ^{1}H-NMR spectrum of the HP-β-CD·**2** complex, showing the cross-peak interactions between the signals of the aromatic protons of **2** (δ = 7.91 and 8.19 ppm) and the H^3, H^5 and H^6 protons of HP-β-CD (δ = 3.85 ppm, δ = 3.75 ppm, and δ = 3.82 ppm, respectively).

Figure S124. The 2D NOESY ^{1}H-NMR spectrum of HP-β-CD·**4** complex, in D$_2$O. Intermolecular cross-peak interactions between HP-β-CD and **4** have been circled.
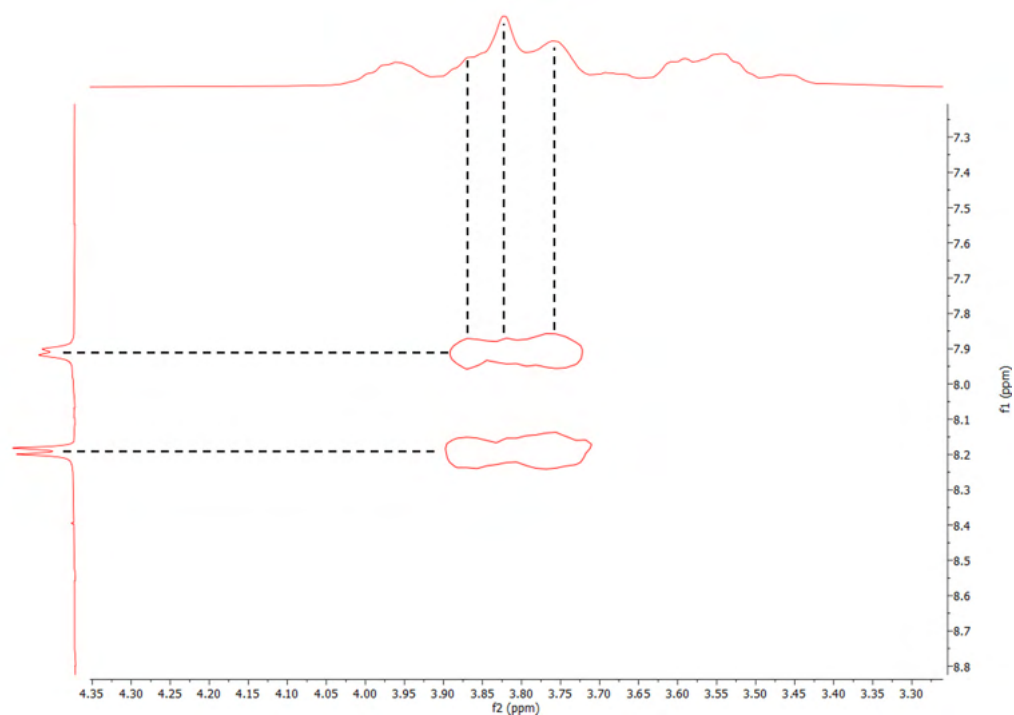

Figure S125. A magnified segment of the 2D NOESY ^{1}H-NMR spectrum of the HP-β-CD·**4** complex, showing the cross-peak interactions between the signals of the adamantyl protons

of **4** (δ = 1.74, 2.08, and 2.22 ppm) and the H^5 and H^6 protons of HP-β-CD (δ = 3.79 ppm and δ = 3.83 ppm, respectively).

Figure S126. A magnified segment of the 2D NOESY ^{1}H-NMR spectrum of the HP-β-CD·**4** complex, showing the cross-peak interactions between the signals of the aromatic protons of **4** (δ = 7.52 and 8.12 ppm) and the H^5 and H^6 protons of HP-β-CD (δ = 3.79 ppm and δ = 3.83 ppm, respectively).
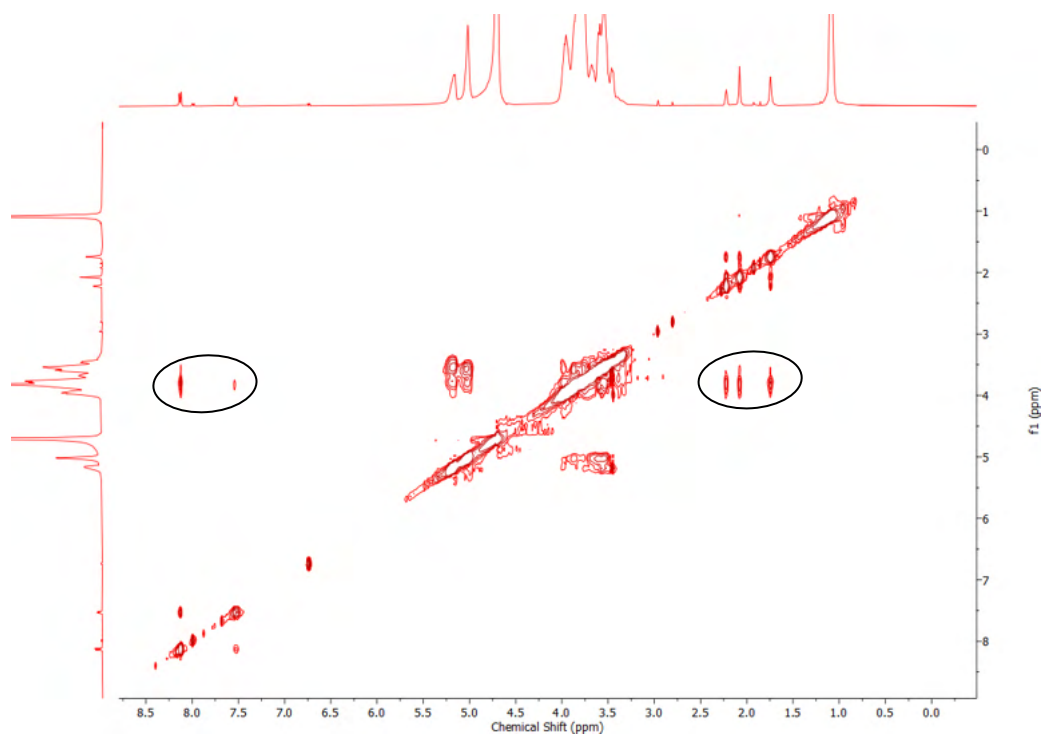
Figure S127. The 2D NOESY ^{1}H-NMR spectrum of HP-β-CD·**6** complex, in D$_2$O. Intermolecular cross-peak interactions between HP-β-CD and **6** have been circled.
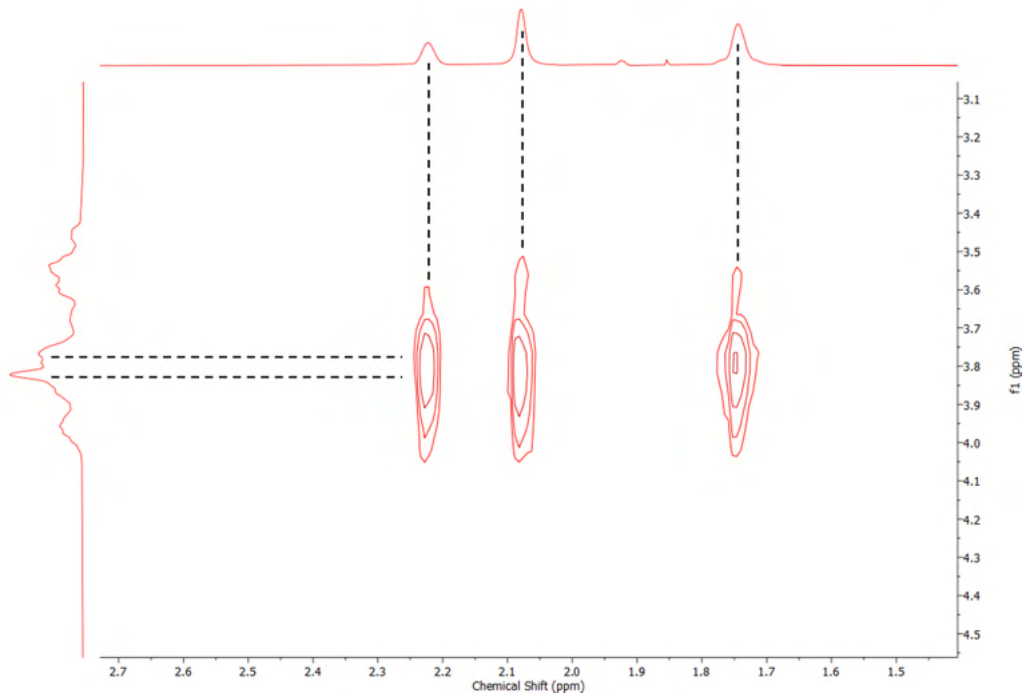

Figure S128. A magnified segment of the 2D NOESY ^{1}H-NMR spectrum of the HP-β-CD·**6** complex, showing the cross-peak interactions between the signals of the adamantyl protons

of **6** (δ = 1.76, 2.16, and 2.29 ppm) and the H^3, H^5, and H^8 protons of HP-β-CD (δ = 3.85 ppm, δ = 3.75 ppm, and δ = 3.95 ppm, respectively).
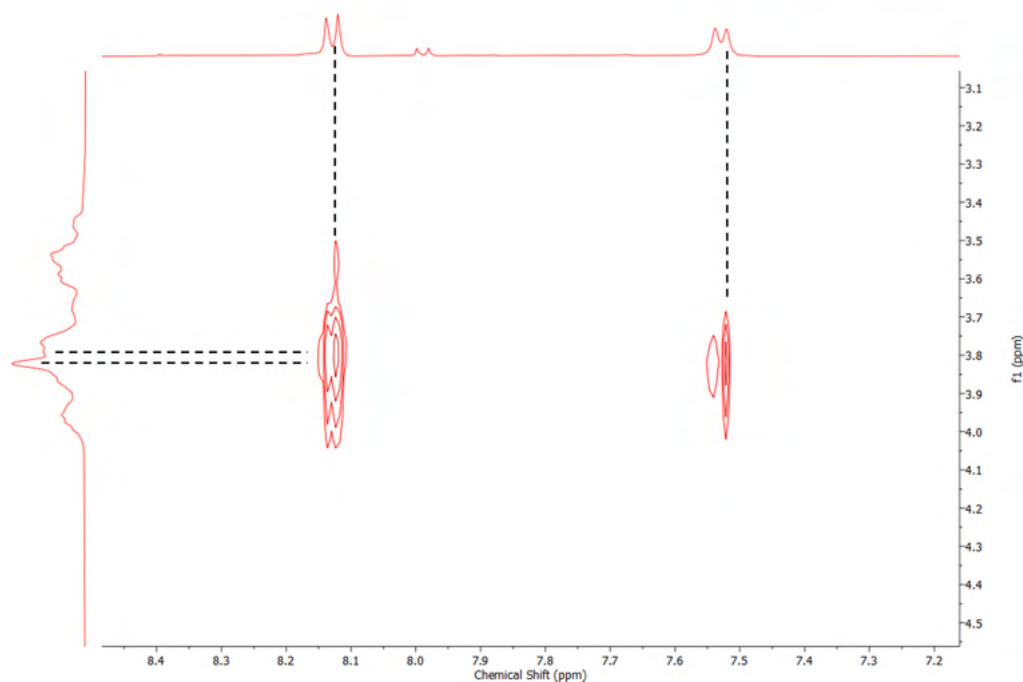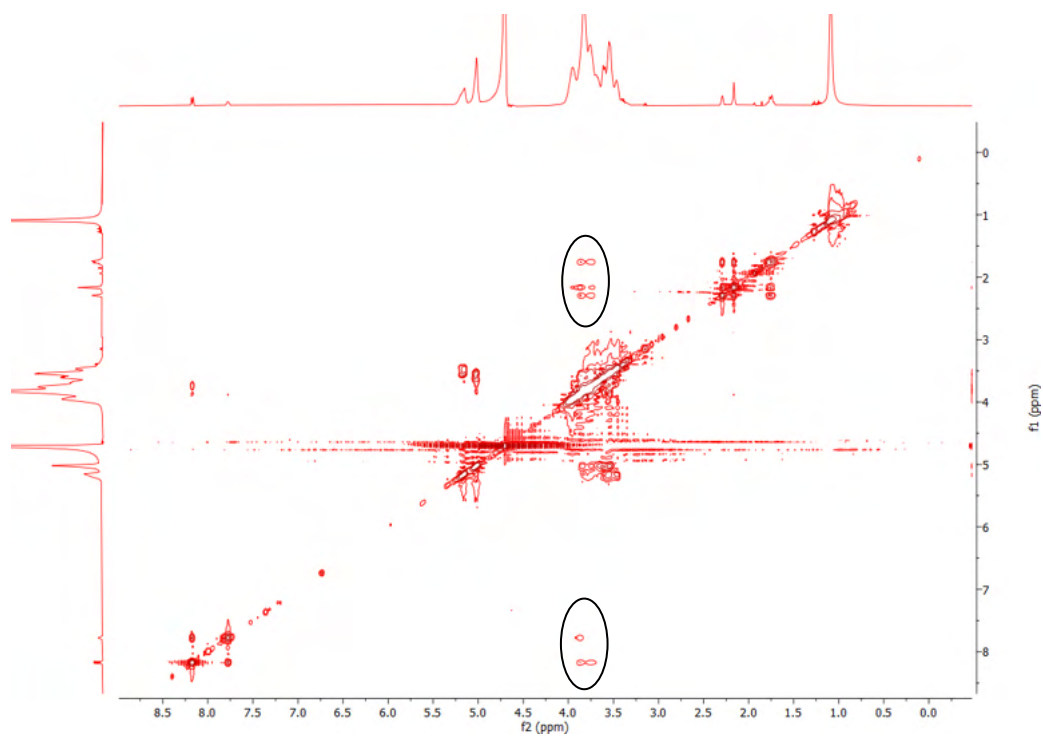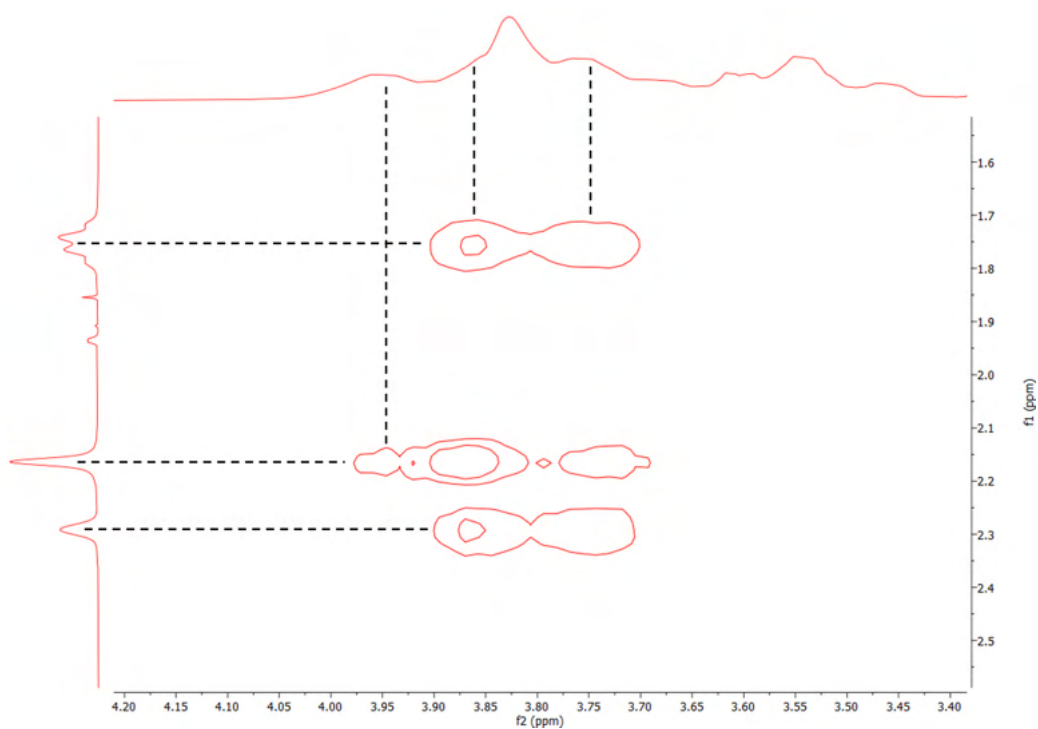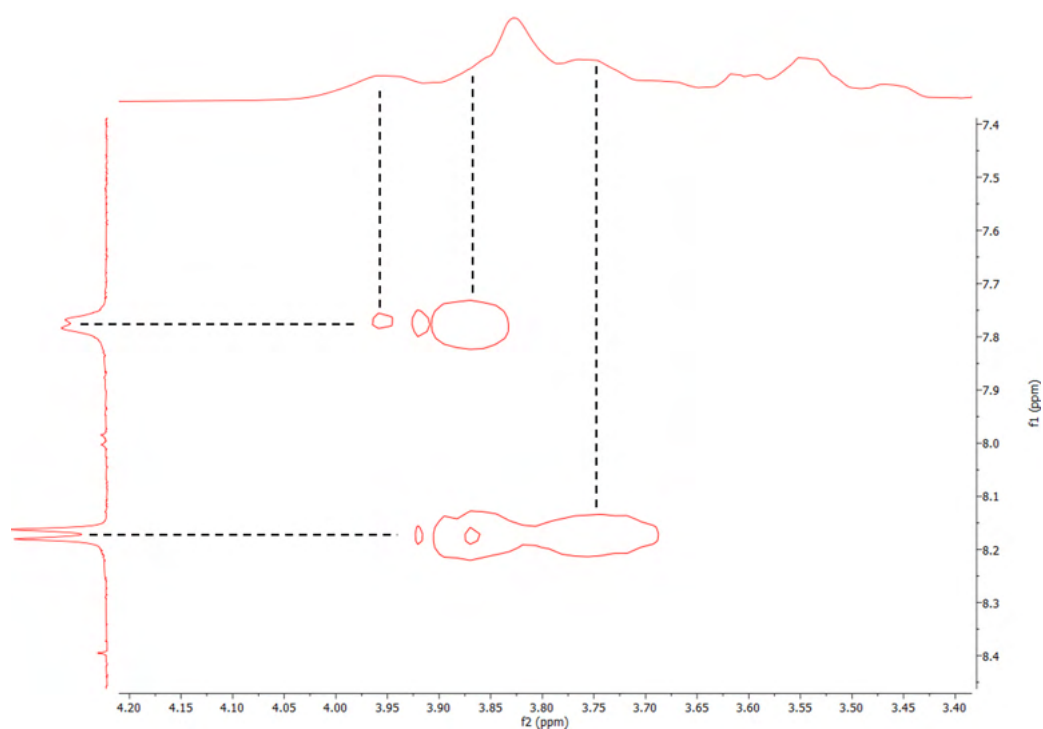

Figure S129. A magnified segment of the 2D NOESY ^{1}H-NMR spectrum of the HP-β-CD·**6** complex, showing the cross-peak interactions between the signals of the aromatic protons of **6** (δ = 7.78 and 8.17 ppm) and the H^3, H^5, and H^8 protons of HP-β-CD (δ = 3.85 ppm, δ = 3.75 ppm, and δ = 3.95 ppm, respectively).

12. Cl⁻/NO₃⁻ Exchange Assay – Hill Analysis

12.1. General Vesicle Preparation

Unilamellar vesicles were prepared following a procedure outlined previously by the Gale group.[26] A chloroform solution of POPC (37.5 mM, 4 mL) was transferred to a pre-weighed round-bottom flask, and the solvent was removed using a rotary evaporator. The pressure was lowered slowly to ensure the formation of a smooth lipid film. Subsequently, the film was dried in vacuo for 4–24 h, and the mass of lipid was recorded. The lipids were rehydrated with 4 mL of the respective internal solution (this number should correspond to the volume of POPC solution used initially) and vortexed until all lipids were removed from the sides of the flask and were suspended in solution. The lipids were subjected to 9 cycles of freeze-thaw by freezing using a dry ice/acetone bath and thawing in lukewarm water. Following this, the vesicles were left to rest at room temperature for 30 min. The lipids were extruded through a 200 nm polycarbonate membrane 25 times to form monodisperse vesicles. Only 1 mL of solution was extruded at a time before being collected. Finally, any residual unencapsulated salt from the internal solution was either removed via dialysis for 12 h in the desired external solution or through size-exclusion using a B19 column packed with hydrated G-25 Sephadex®, which had been pre-saturated with the respective external solution. The lipid suspensions were diluted with the external solution to afford a stock solution (10 mL) of a known concentration.

12.2. Electrode Calibration and Conversion of Raw Data

An Accumet chloride ion-selective electrode (ISE) was used for both the Cl⁻/NO₃⁻ exchange assay and the cationophore coupled assay. Before the beginning of each set of experiments, calibration of the electrode was required to correct any drift between recorded datasets. The electrode was submerged in a sequence of NaCl solutions of increasing concentration (M), and the reading from the electrode was recorded after stabilising after 5–15 min. The electrode potential reading, y, was plotted against NaCl concentration (M), x, and fitted to a simplified Nernst equation using *Origin 2021b (Academic)*. The equation is given as followed:

$$y = (P_1 log_{10} x) + P_2$$

Equation S7. Calibration of electrode potential data using a simplified Nernst equation.

where P_1 and P_2 are the calibration parameters. The chloride ion concentration at any given time during the experiments can be calculated by substituting P_1, P_2 and y, the electrode potential reading, into the equation and solving for x, the chloride ion concentration. By subtracting the chloride concentration at $t = 0$ from the concentration at a given time during the experiment, the total chloride concentration released from the vesicles at that given time can be calculated. Conversion to percentage chloride efflux was achieved by normalising the chloride concentration at time (t) using the 100% chloride efflux value recorded at the end of the experiment ($t = 420$ s) when the vesicles were lysed with a water dispersion of Triton X-100 (10% v/v).

12.3. Dose-Response Hill Analysis Assay Conditions

Vesicles were prepared using an internal solution of NaCl (487 mM) and buffered to pH 7.2 using a sodium phosphate salt buffer of NaH_2PO_4 (1.2 mM) and Na_2HPO_4 (4mM). An external solution containing $NaNO_3$ (487 mM) was prepared separately with the same sodium phosphate salt buffer and adjusted to pH 7.2 using an aqueous solution of dilute NaOH. Following the freeze-thaw cycles and extrusion, the NaCl lipids were dialysed in the $NaNO_3$ external solution (~ 1600 mL) for 12h. The lipid stock solution (10 mL) was diluted with the external solution to give both a concentration and volume suitable for ISE experiments (1 mM, 5 mL).

Each receptor was added as a DMSO solution (10 μL) at $t = 0$ s, and the change in chloride concentration was recorded using an Accumet chloride ISE. At $t = 300$ s, a detergent solution (Triton X-100 (10% v/v in H_2O), 50 μL) was injected to lyse the vesicles, and a final chloride concentration reading was recorded at $t = 420$ s to provide a 100% chloride efflux reading for use in calibration.

Dose-response experiments were performed at six transporter concentrations and a blank DMSO run, and percentage efflux at $t = 270$ s was recorded for each concentration tested. The chloride efflux (%) at $t = 270$ s was plotted against receptor concentration (mol%, with respect to lipid concentration). The recorded data was fit to the Hill Equation, using *Origin 2021b (Academic)*, given as:

$$y = V_{max} \frac{x^n}{k^n + x^n}$$

Equation S8. The Hill equation.

where y represents the percentage of chloride efflux at $t = 270$ s, x is the transporter concentration (mol%, with respect to lipids concentration), and V_{max}, k and n are the parameters to be fitted. V_{max} represents the maximum chloride efflux (typically fixed to 100%), n can be interpreted as the Hill coefficient. A derived equation was used to calculate the EC_{50} value, the transporter concentration required to facilitate 50% chloride efflux, given as:

$$EC_{50} = k \left(\frac{50}{y_1 - y_0 - 50} \right)^{\frac{1}{n}}$$

Equation S9. The adapted EC_{50} equation.

where k and n are the derived parameters from the Hill equation, y_0 is the percentage chloride efflux at $t = 0$ s, and y_1 is the percentage chloride efflux at $t = 300$ s.

12.4. Maximum Rate Calculations

The maximum rate of chloride efflux was calculated for receptors **1**, **2**, **4–6**, and inclusion complexes HP-β-CD·(**1**, **2**, **4**, **6**) at 2 mol%, by fitting the efflux plot at the given concentration to **Equation S10**, in *Origin 2021b (Academic)*, given as:

$$y = A_1 e^{\left(\frac{-x}{t_1} \right)} + A_2 e^{\left(\frac{-x}{t_2} \right)} + y_0$$

Equation S10. A non-linear exponential decay function.

where y represents the percentage of chloride efflux (%), x is the receptor concentration (mol%), y_0 is the percentage chloride efflux at $t = 0$ s, and A_1, A_2, t_1, and t_2 are the derived parameters. The maximum rate was obtained by calculating the first derivative at $x = 0$, which is given as:

$$K_{initial} = \frac{-A_1}{t_1} - \frac{A_2}{t_2}$$

Equation S11. Derivative of the decay function used to determine the maximum rate given in % s^{-1}.

The maximum rate of chloride efflux was calculated for receptor **3** at 2 mol%, by fitting the efflux plot at the given concentration to a non-linear Boltzmann curve function, in *Origin 2021b (Academic)*, given as:

$$y = A_2 + \frac{(A_1 - A_2)}{(1 + e^{(\frac{x - x_0}{dx})})}$$

Equation S12. The Boltzmann function was used for the fitting of the efflux plots for compound **3**.

where y represents the percentage of chloride efflux (%), x is the receptor concentration (mol%), and A_1, A_2, x_0, and dx are the derived parameters. The maximum rate was obtained by calculating the first derivative at $x = 0$, which is given as:

$$K_{max} = \frac{A_2 - A_1}{4dx}$$

Equation S13. Derivative of the Boltzmann function used to determine the maximum rate given in %s^{-1}.

12.5. Cl$^-$/NO$_3^-$ Exchange Assay – Efflux and Hill Plots

Figure S130. Hill analysis of Cl$^-$/NO$_3^-$ exchange facilitated by **1**. Each data point is the average of two repeats with error bars to show standard deviation. A run of pure DMSO was used as a control.
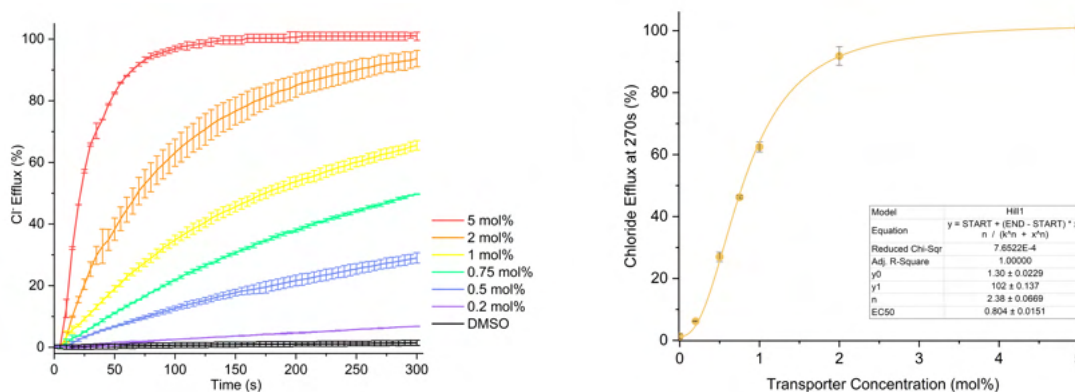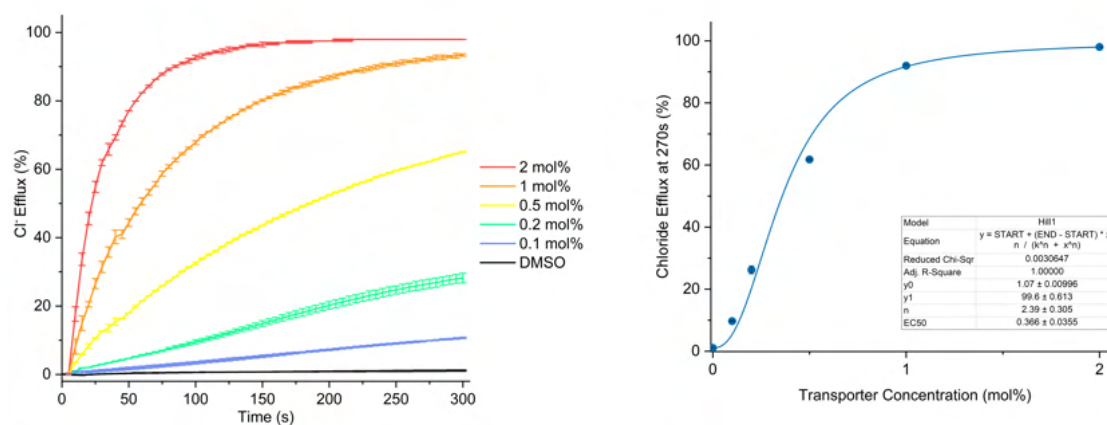
Figure S131. Hill analysis of Cl⁻/NO₃⁻ exchange facilitated by **2**. Each data point is the average of two repeats with error bars to show standard deviation. A run of pure DMSO was used as a control.
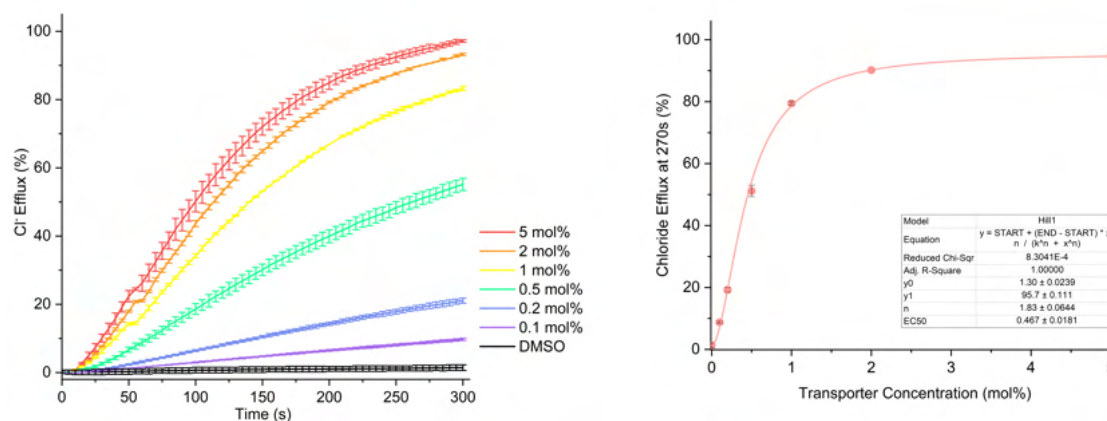

Figure S132. Hill analysis of Cl⁻/NO₃⁻ exchange facilitated by **3**. Each data point is the average of two repeats with error bars to show standard deviation. A run of pure DMSO was used as a control.
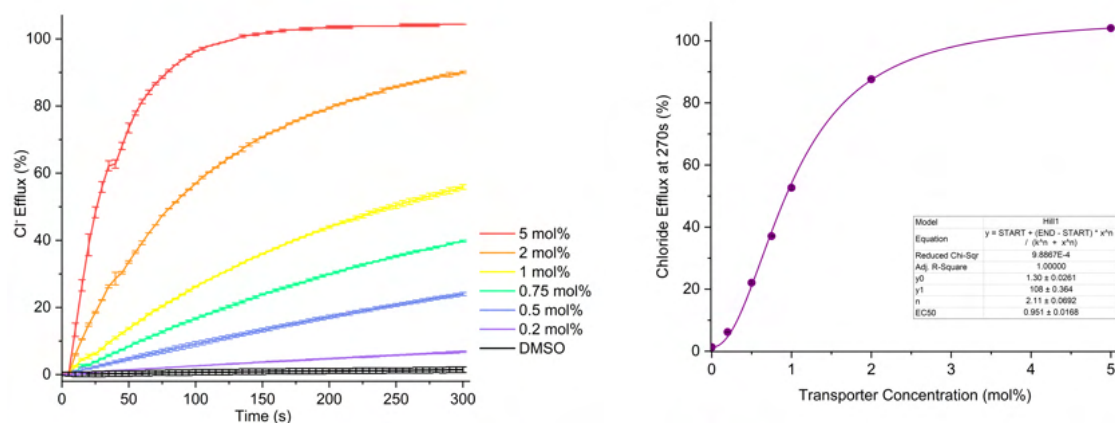
Figure S133. Hill analysis of Cl⁻/NO₃⁻ exchange facilitated by **4**. Each data point is the average of two repeats with error bars to show standard deviation. A run of pure DMSO was used as a control.

Figure S134. Hill analysis of Cl⁻/NO₃⁻ exchange facilitated by **5**. Each data point is the average of two repeats with error bars to show standard deviation. A run of pure DMSO was used as a control.
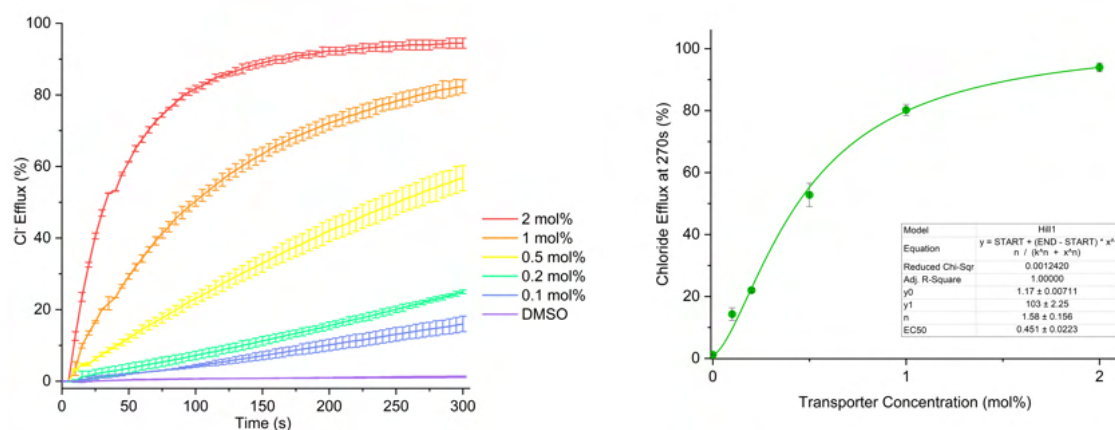
Figure S135. Hill analysis of Cl⁻/NO₃⁻ exchange facilitated by **6**. Each data point is the average of two repeats with error bars to show standard deviation. A run of pure DMSO was used as a control.
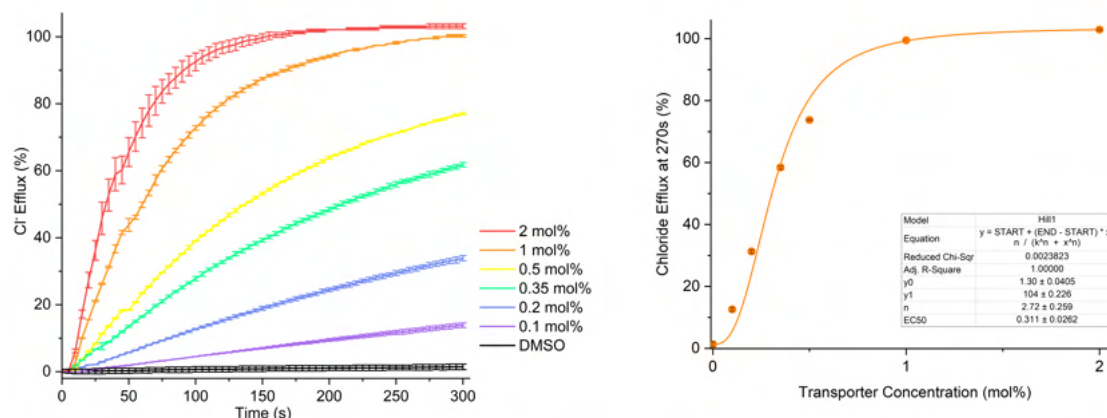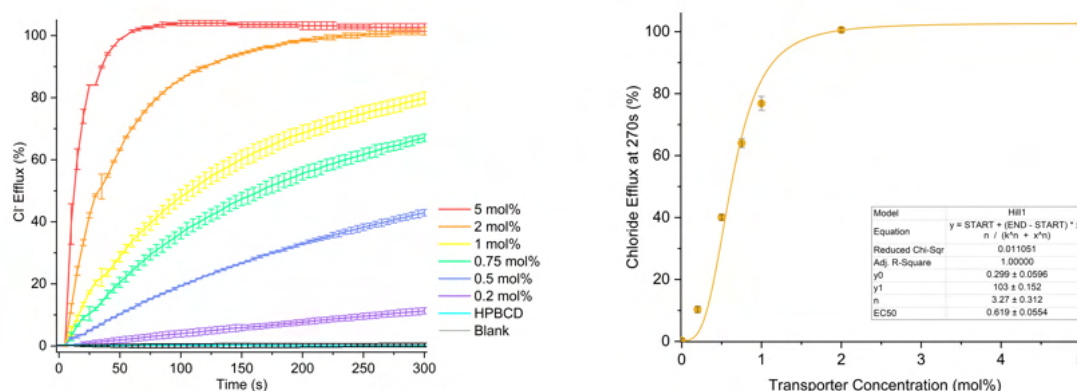

Figure S136. Hill analysis of Cl⁻/NO₃⁻ exchange facilitated by the HP-β-CD·**1** inclusion complex. Each data point is the average of two repeats with error bars to show standard deviation. A run of pure deionized H₂O and a run of solely HP-β-CD were used as controls.

Figure S137. Hill analysis of Cl^-/NO_3^- exchange facilitated by the HP-β-CD·**2** inclusion complex. Each data point is the average of two repeats with error bars to show standard deviation. A run of pure deionized H_2O and a run of solely HP-β-CD were used as controls.
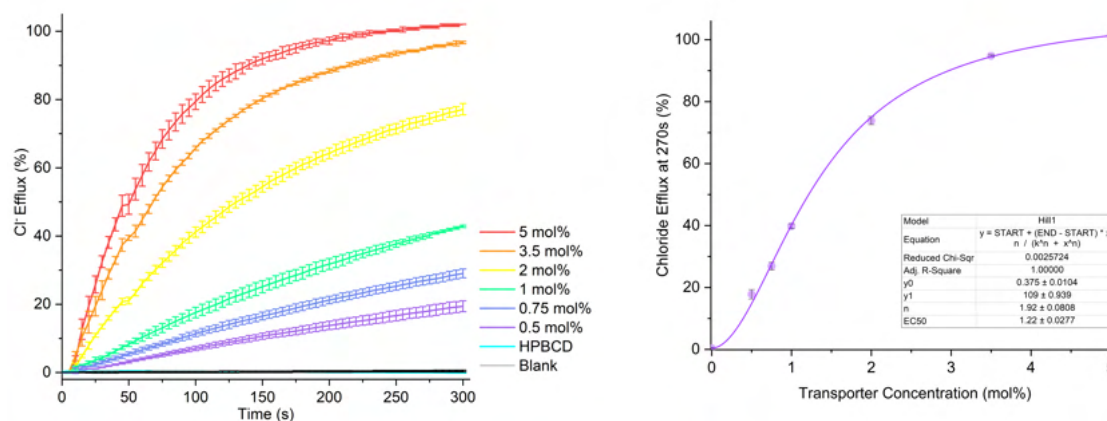
Figure S138. Hill analysis of Cl^-/NO_3^- exchange facilitated by the HP-β-CD·**4** inclusion complex. Each data point is the average of two repeats with error bars to show standard deviation. A run of pure deionized H_2O and a run of solely HP-β-CD were used as controls.
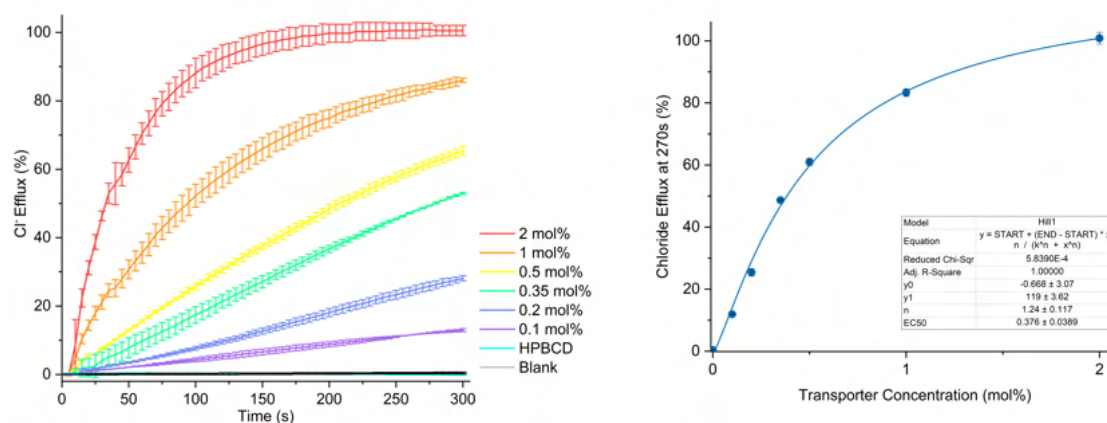
Figure S139. Hill analysis of Cl⁻/NO₃⁻ exchange facilitated by the HP-β-CD·**6** inclusion complex. Each data point is the average of two repeats with error bars to show standard deviation. A run of pure deionized H_2O and a run of solely HP-β-CD were used as controls.
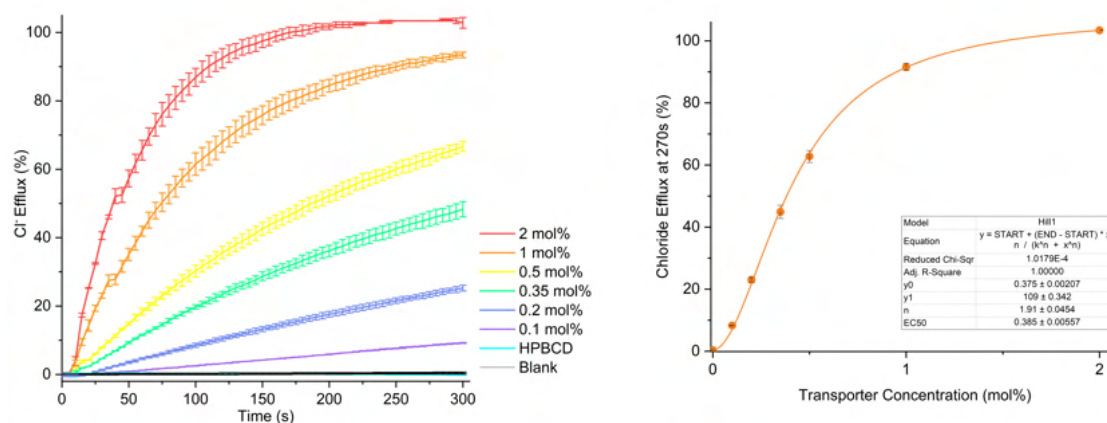
13. References

1. D. Brynn Hibbert and P. Thordarson, *Chem. Commun.*, 2016, **52**, 12792-12805.

2. J. Szejtli, *Chem. Rev.*, 1998, **98**, 1743-1754.

3. J. C. Harrison and M. R. Eftink, *Biopolymers*, 1982, **21**, 1153-1166.

4. G. Tiwari, R. Tiwari and A. K. Rai, *J. Pharm. Bioallied Sci.*, 2010, **2**, 72-79.

5. S. Gould and R. C. Scott, *Food Chem. Toxicol.*, 2005, **43**, 1451-1459.

6. M. E. Bellringer, T. G. Smith, R. Read, C. Gopinath and P. Olivier, *Food Chem. Toxicol.*, 1995, **33**, 367-376.

7. M. E. Brewster, K. S. Estes and N. Bodor, *Int. J. Pharm.*, 1990, **59**, 231-243.

8. F. J. O. Espinar, S. A. Igea, J. B. Méndez and J. L. V. Jato, *Int. J. Pharm.*, 1991, **70**, 35-41.

9. C.-W. Lee, S.-J. Kim, Y.-S. Youn, E. Widjojokusumo, Y.-H. Lee, J. Kim, Y.-W. Lee and R. R. Tjandrawinata, *J. Supercrit. Fluids*, 2010, **55**, 348-357.

10. M. Stojanov, R. Wimmer and K. L. Larsen, *J. Pharm. Sci.*, 2011, **100**, 3177-3185.

11. T. C. Chen, S.-C. Yu, C.-M. Hsu, F.-J. Tsai and Y. Tsai, *J. Incl. Phenom. Macrocycl. Chem.*, 2017, **88**, 27-34.

12. K. P. Sambasevam, S. Mohamad, N. M. Sarih and N. A. Ismail, *Int. J. Mol. Sci.*, 2013, **14**.

13. S. Riela, G. Lazzara, P. Lo Meo, S. Guernelli, F. D'Anna, S. Milioto and R. Noto, *Supramol. Chem.*, 2011, **23**, 819-828.

14. J. Pitha, J. Milecki, H. Fales, L. Pannell and K. Uekama, *Int. J. Pharm.*, 1986, **29**, 73-82.

15. W. M. Haynes, *CRC handbook of chemistry and physics*, CRC press, 2014.

16. A. Rostami, A. Colin, X. Y. Li, M. G. Chudzinski, A. J. Lough and M. S. Taylor, *JOC*, 2010, **75**, 3983-3992.

17. Á. Nacsa, R. Ambrus, O. Berkesi, P. Szabó-Révész and Z. Aigner, *J. Pharm. Biomed. Anal.*, 2008, **48**, 1020-1023.

18. Y.-l. Shen, S.-h. Yang, L.-m. Wu and X.-y. Ma, *Spectrochim. Acta. A Mol. Biomol. Spectrosc.*, 2005, **61**, 1025-1028.

19. A. Figueiras, L. Ribeiro, M. T. Vieira and F. Veiga, *J. Incl. Phenom. Macrocycl. Chem.*, 2007, **57**, 173-177.

20. S. Prabu, M. Swaminathan, K. Sivakumar and R. Rajamohan, *J. Mol. Struct.*, 2015, **1099**, 616-624.

21. M. Shanmugam, D. Ramesh, V. Nagalakshmi, R. Kavitha, R. Rajamohan and T. Stalin, *Spectrochim. Acta. A Mol. Biomol. Spectrosc.*, 2008, **71**, 125-132.

22. P. Mura, *J. Pharm. Biomed. Anal.*, 2015, **113**, 226-238.

23. O. Adeoye, C. Costa, T. Casimiro, A. Aguiar-Ricardo and H. Cabral-Marques, *J. Supercrit. Fluids*, 2018, **133**, 479-485.

24. P. P. Menezes, M. R. Serafini, B. V. Santana, R. S. Nunes, L. J. Quintans, G. F. Silva, I. A. Medeiros, M. Marchioro, B. P. Fraga, M. R. V. Santos and A. A. S. Araújo, *Thermochim. Acta*, 2012, **548**, 45-50.

25. D. Neuhaus, *eMagRes*, 2007.

26. L. A. Jowett and P. A. Gale, *Supramol. Chem.*, 2019, **31**, 297-312.